Quantum state reconstruction of classical and nonclassical light and a cryogenic opto-mechanical sensor for high-precision interferometry

Dissertation

zur Erlangung des akademischen Grades des
Doktors der Naturwissenschaften
(Dr. rer. nat.)
and der Universität Konstanz
Fakultät für Physik

vorgelegt von

Gerd Breitenbach

Konstanz, Juni 1998

Dedicated to my dear friend and coworker Klaus Schneider
(04.10.1969 – 30.03.1998)

Overview

Central topic of this thesis is the investigation of the quantum nature of light. This investigation is carried out in two separate experiments which are described in part I and part II respectively.

In part I, classical and non-classical laser radiation is characterized at the quantum mechanical level with respect to its amplitude and phase fluctuations, its photon number distribution and other observable quantities. This is done by employing recently developed methods of quantum state reconstruction. Such a complete characterization is of fundamental interest, since it can provide a much more detailed experimental description of light than previously known. Furthermore, since many experimental systems are analyzed by optical means, these methods may in future find important applications in the characterization of such systems in full quantum mechanical detail, by determining the state of the light field used as a probe before and after the interaction with the system.

In part II, high precision position measurements via laser interferometry are investigated. Such measurements play an important role in the microscopic domain (optomechanical sensors, modern microscopy techniques) as well as in the macroscopic domain (development of large scale interferometers for the detection of gravitational waves). The goal of the second experiment is to explore the quantum mechanical limits in the precision with which the position of a macroscopic body can be determined.

One common conceptual aspect of both experiments, besides the similar optical techniques employed, is that both attempt a high precision characterization of a harmonic oscillator system disturbed by stochastic noise. In part I, this oscillator is the light field, subject to quantum noise, in part II, it is a mechanical harmonic oscillator excited by thermal noise. Further considerations about the connection and possible unification of the two experiments can be found in the outlook to part II.

The main results of the first part of the thesis are
(i) the complete mapping of the whole family of squeezed states of the light field, that is light with reduced quantum noise. The values for noise suppression are among the highest achieved so far,
(ii) the first direct evidence of photon number oscillations in parametrically downconverted light, and
(iii) the measurement of the first-order time correlation function of the light field of squeezed vacuum.

The main result of the second part is the detection of the Brownian motion of a cryogenically cooled high-Q mechanical oscillator, using a high-finesse Fabry-Perot interferometer. Displacements in the order of 10^{-14} m of a macroscopic object were detected.

Kurzfassung

Das zentrale Thema der vorliegenden Arbeit ist die Untersuchung der Quantennatur des Lichtes. Diese Untersuchung wurde in zwei separaten Experimenten durchgeführt, welche in Teil I und Teil II beschrieben werden.

In Teil I wird klassische und nichtklassische Laserstrahlung auf quantenmechanischer Ebene charakterisiert, im Hinblick auf seine Amplituden- und Phasenfluktuationen, seine Photonenzahlverteilung und andere observable Größen. Dies geschieht mit Hilfe von jüngst entwickelten Methoden der Quantenzustandsrekonstruktion. Solch eine vollständige Charakterisierung ist zum einen von fundamentalem Interesse, da sie eine bei weitem detailliertere experimentelle Beschreibung von Licht ermöglicht, als bisher bekannt war. Zum anderen werden viele experimentelle Systeme mit Hilfe optischer Verfahren analysiert, wodurch diese Methoden der Quantenzustandsrekonstruktion zukünftig eine wichtige Anwendung im Rahmen der Charakterisierung solcher Systeme finden können, indem der Zustand des sondierenden Lichtfeldes vor und nach der Wechselwirkung mit dem System bestimmt wird.

In Teil II werden laserinterferometrische Präzisionsmessungen des Ortes untersucht. Solche Messungen spielen sowohl im mikroskopischen (optomechanische Sensoren, moderne Techniken der Mikroskopie), als auch im makrosopischen Bereich (Entwicklung von Gravitationswellendetektoren) eine wichtige Rolle. Das Ziel dieses zweiten Experimentes ist es, die quantenmechanische Grenze der Präzision zu erforschen, mit welcher der Ort eines makroskopischen Gegenstandes bestimmbar ist.

Ein gemeinsamer Aspekt beider Experimente, neben den jeweils verwendeten ähnlichen optischen Techniken, ist der, daß beide hochpräzise Charakterisierungen eines von stochastischem Rauschen gestörten harmonischen Oszillatorsystems vornehmen. In Teil I is dieser Oszillator das Lichtfeld selbst, welches dem Quantenrauschen ausgesetzt ist, in Teil II ist es ein mechanischer Oszillator, angeregt durch thermisches Rauschen.

Die Hauptresultate des ersten Teils der Dissertation sind
(i) die vollständige experimentelle Aufzeichnung der gesamten Familie der gequetschten Zustände des Lichtfeldes, d.h. Zustände mit verringertem Quantenrauschen. Der Betrag der Rauschunterdrückung liegt gleichauf mit den weltweit erzielten Bestwerten,
(ii) der erste direkte Nachweis von Photonenzahloszillationen bei parametrisch konvertiertem Licht und
(iii) die Messung der Zeitkorrelationsfunktion erster Ordnung des Lichtfeldes von gequetschtem Vakuum.

Das Hauptergebnis des zweiten Teils ist der Nachweis der Brownschen Bewegung eines kryogen gekühlten mechanischen Oszillators hoher mechanischer Güte mit Hilfe eines Hochfinesse-Fabry-Perot-Interferometers. Ortsverschiebungen in der Größenordnung von 10^{-14} m wurden detektiert.

Contents

1 Introduction to part I

A central issue in many fields of quantum physics is the development and application of theoretical and experimental tools for obtaining information about the states of quantum fields of matter and radiation. Although the state of an individual particle or system is unobservable, it is possible to determine the state of an ensemble of identically prepared systems by performing a large number of measurements [204]. This procedure of state determination is called quantum state reconstruction. Experimentally the first quantum state reconstruction was performed by Havener et al. [85], who determined the density matrix of a H(n=3) atom. But it was not until a more general theoretical background was laid out [13, 259][1] and the first measurement of the Wigner function, a quantum mechanical analogue of the classical phase space distribution, was implemented [229, 230] that the field started flourishing.

Notable experimental success has since then been achieved in generating and determining states of various quantum mechanical systems such as a single mode of light [229, 230, 163, 28, 30, 31], vibrational modes of a diatomic molecule [60, 5] and of an ion in a Paul trap [132], and the motional state of freely propagating atoms [126] (for reviews see [70, 110]).

The first part of this thesis presents the investigation of the light field by methods of quantum state reconstruction. Special emphasis is placed on the characterization of so-called *squeezed states* of light: The electric field of a freely evolving monochromatic laser wave propagating sinusoidally in space is best described in quantum optics by a coherent state [74]. Due to the fact that the operators for phase and amplitude quadrature of the light field do not commute, any light wave carries intrinsic quantum noise, having its origin in Heisenberg's uncertainty relation. For coherent states this quantum noise is evenly distributed between both quadratures. For squeezed states the quantum noise is less in one quadrature than in its conjugate, thus the noise variance is changing periodically during the wave's propagation.

Squeezed states were first defined and theoretically analyzed in [109, 240, 161, 235, 280, 94] (see also the overviews in [196, 232, 266]). Squeezing is a general phenomenon of harmonic oscillations accompanied by noise. Not only the light field, but also the motional state of a trapped atom (few phonons) [156], ensembles of phonons in crystals [72] and thermomechanical noise [206] have been squeezed in the past. For the light field the first observations of squeezed states are by now more than 10 years old [227, 224, 276, 146]. Still, as the most easily accessible class of non-classical states and as a potential means of noise reduction in precision measurements, for example resolution enhancement of interferometers [40, 278, 76], high resolution spectroscopy [184], weak absorption measurements [79], and quantum nondemolition measurements [34], they remain an important subject

[1] citations are given in chronological rather than alphabetical (numerical) order

of present-day research efforts.

Part I of this thesis is structured as follows: First a brief theoretical outline of quantum state reconstruction and the generation of squeezed states is given. In the following experimental chapter the setup (Sec. 3.1) and the measurements of squeezed and coherent states (Sec. 3.2) are presented. Various reconstruction methods are applied (3.3–3.5). The investigation of the quantum states emitted by the OPO directly at threshold and of classical superpositions of coherent states is described in sections 3.6 and 3.7. The last experiment presented in this first part is the simultaneous detection of a whole spectrum of quantum states and the measurement of the first order time correlation function. Section 3.10 gives an overview over all experimentally investigated states of the light field, concluded by a short outlook.

2 Theory I: Reconstruction of quantum states of the light field

2.1 The state of a quantum system

The state of a one-dimensional quantum system with Hamiltonian H is described by its state vector $|\,\psi\,\rangle$ which obeys the evolution equation

$$i\hbar\frac{\partial}{\partial t}|\,\psi,t\,\rangle = H\,|\,\psi\,\rangle\,. \tag{2.1}$$

In the coordinate representation of the Schrödinger picture, the state vector is given by a complex wave function

$$\psi(x,t) = \langle\, x\,|\,\psi,t\,\rangle\,. \tag{2.2}$$

In the case of an ensemble of identically prepared systems each with probability p_i in a particular state $|\,\psi_i\,\rangle$, the whole system is described by its density operator $\hat\rho = \sum_i p_i|\,\psi_i\,\rangle\langle\,\psi_i\,|$ [64, 16] obeying the evolution equation

$$i\hbar\frac{\partial\hat\rho(t)}{\partial t} = -\,[\,H,\hat\rho(t)\,] \tag{2.3}$$

(neglecting the coupling to an outer environment). If the density operator is known, the expectation value for any arbitrary physical variable represented by an operator A can be calculated via [1]

$$\langle\, A\,\rangle = \mathrm{Tr}(\hat\rho A)\,, \tag{2.4}$$

this is the reason for saying, the state of the system is completely determined by its density matrix.

An important representation of the density matrix is given by its expansion in the Fock state basis

$$\hat\rho = \sum_{m,n}\rho_{mn}\,|\,m\,\rangle\langle\,n\,| \tag{2.5}$$

with $\rho_{mn} = \langle\, m\,|\,\hat\rho\,|\,n\,\rangle$. The diagonal elements of $\hat\rho$ determine the state's distribution of energy quanta, i.e. for the light field the photon statistics $p_n = \rho_{nn}$. (For a discussion of the usefulness of the notion of a photon see [127]).

An equivalent description of the state of a system offers the Wigner function, a quantum mechanical analogue of the classical phase space distribution [272, 89]. It is defined by

$$W(x,p) = \frac{1}{2\pi}\int_{-\infty}^{\infty} e^{ipx'}\langle\, x-\frac{x'}{2}\,|\,\hat\rho\,|\,x+\frac{x'}{2}\,\rangle\,\mathrm{d}x'\,. \tag{2.6}$$

[1] Throughout this thesis operators are denoted by capital letters *or* by small letters with a hat.

As a joint distribution function of position x and momentum p it cannot be a probability distribution, since it may take on negative values. Nevertheless it retains many properties of a classical two-dimensional probability distribution: It is real, its marginal distributions are the position and momentum distributions

$$\begin{aligned} \int_{-\infty}^{\infty} W(x,p)\mathrm{d}p &= \langle\, x \,|\, \hat{\rho} \,|\, x \,\rangle = P(x)\,, \\ \int_{-\infty}^{\infty} W(x,p)\mathrm{d}x &= \langle\, p \,|\, \hat{\rho} \,|\, p \,\rangle = P(p)\,, \end{aligned} \tag{2.7}$$

$$\tag{2.8}$$

and similar to the density operator it can be used to calculate expectation values of any arbitrary physical variable represented by an operator A:

$$\mathrm{Tr}(\hat{\rho}A) = 2\pi \int_{-\infty}^{\infty}\int_{-\infty}^{\infty} W(x,p)W_A(x,p)\,\mathrm{d}x\mathrm{d}p\,, \tag{2.9}$$

where the $W(x,p)$ is the Wigner function of the state and $W_A(x,p)$ is the Wigner function of the operator A defined by

$$W_A(x,p) = \frac{1}{2\pi}\int_{-\infty}^{\infty} e^{ipx'} \langle\, x - \frac{x'}{2} \,|\, A \,|\, x + \frac{x'}{2} \,\rangle\, \mathrm{d}x'\,. \tag{2.10}$$

Due to these properties $W(x,p)$ is called a quasiprobability distribution.[2]

2.2 The light field

In quantum optics the single mode light field of frequency ω is described by a quantum harmonic oscillator. Its Hamiltonian is given by

$$H = \hbar\omega(\hat{n} + \frac{1}{2})\,, \tag{2.11}$$

where $\hat{n} = \hat{a}^\dagger\hat{a}$ is the photon number operator, $\hat{a}$ and $\hat{a}^\dagger$ being the annihilation and creation operators.

In comparison with the description of a single particle in a harmonic potential, position x and momentum p are replaced by the operators of the amplitude and phase quadrature $X = (\hat{a} + \hat{a}^\dagger)/\sqrt{2}$ and $Y = (\hat{a} - \hat{a}^\dagger)/\sqrt{2}i$, of the electric field.[3] Since the two

[2] Hillery et al. [89] list altogether seven properties which define the function uniquely. This makes it possible to extend the concept of the Wigner function to other spaces [256]. For applications of the Wigner function to classical optics see [10].

[3] Note that the scaling factor $\sqrt{2}$ in the transformation $X, Y \to a, a^\dagger$ becomes noticeable, when phase space amplitudes are put in relation to photon numbers $n = aa^\dagger$. The factor $1/2$ for e_0 in Eq. 3.17 and Eq. 2.20 vanishes when using the asymmetric transformation $X = (\hat{a} + \hat{a}^\dagger)$ and $Y = (\hat{a} - \hat{a}^\dagger)/i$.

quadrature operators do not commute, $[X,Y] = i$, their standard deviations must obey the Heisenberg uncertainty relation

$$\Delta X \Delta Y \geq 1\,. \tag{2.12}$$

(Note that a strict derivation of this inequation from the uncertainty relation would lead to a factor 1/2 on the right side. Since the scaling of the uncertainties is to some extent arbitrary when comparing experimental values with theory, I use a normalization in which the vacuum field's variance is most simple, $\Delta X = \Delta Y = 1$.)

2.2.1 States of the light field

Fock states $|\,n\,\rangle$, coherent states $|\,\alpha\,\rangle$ and squeezed states $|\,\alpha,\zeta\,\rangle$ are the three basic types of states that we are interested in, since they will appear later on in calculations or the description of the measurements. Another class of states, incoherent superpositions of coherent states, will be presented in the experimental section.

Fock states

The energy eigenfunctions or Fock states $|\,n\,\rangle$ are given in the Schrödinger representation by

$$\psi_n(x) = \langle\, x|\,n\,\rangle = \frac{1}{\pi^{1/4}\sqrt{2^n n!}} H_n(x)\exp(-x^2/2)\,, \tag{2.13}$$

where H_n denotes the nth Hermite polynomial. Especially the wave function of the vacuum state $|\,0\,\rangle$ is given by the Gaussian distribution

$$\psi_0(x) = \frac{1}{\pi^{1/4}}\exp(-x^2/2)\,. \tag{2.14}$$

Since the energy eigenfunctions are stationary states, their time evolution consists simply of a phase shift: $|\,n,t\,\rangle = U(t)\,|\,n\,\rangle = e^{\mathrm{i}n\omega t}\,|\,n\,\rangle$, where $U(t) = \exp(-\mathrm{i}\omega t\,\hat{a}^\dagger\hat{a})$ is the time evolution operator.

Coherent states

Coherent states are defined by

$$|\,\alpha\,\rangle = \exp\left(-\frac{1}{2}\,|\,\alpha\,|^2\right)\sum_{n=0}^{\infty}\frac{\alpha^n}{\sqrt{n!}}\,|\,n\,\rangle\;. \tag{2.15}$$

They can be considered as being generated by letting the displacement operator $D(\alpha) \equiv \exp(\alpha\,\hat{a}^\dagger - \alpha^*\hat{a})$ act on the vacuum state $|\,\alpha\,\rangle = D(\alpha)\,|\,0\,\rangle$. The wave function of a coherent state with amplitude $\alpha = 2^{-1/2}\,(e_0\cos\phi + \mathrm{i}\,e_0\sin\phi)$ follows from Eq. 2.15 [222]

$$\psi_\alpha(x) = \frac{1}{\pi^{1/4}}\,\exp\left[-\frac{(x-e_0\cos\phi)^2}{2}\;+\;\mathrm{i}\,x\,e_0\sin\phi\;-\;\frac{\mathrm{i}\,e_0^2\,\sin 2\phi}{4}\right]\,. \tag{2.16}$$

Replacing $|\, n \,\rangle$ by $|\, n \,\rangle \, \mathrm{e}^{\mathrm{i}n\omega t}$ in Eq. 2.15 results in a time evolution of the wave packet of

$$|\psi_\alpha(x,t)|^2 = \frac{1}{\sqrt{\pi}} \exp\left[-(x \, - \, (e_0 \, \cos(\omega t \, - \, \phi))^2\right] . \tag{2.17}$$

Thus the wave packet oscillates back and forth. This behavior, similar to the one of a classical point mass, was the original motivation for Schrödinger to study coherent states as a first example of quantum dynamics in 1926 [222] (see also [26]). In quantum optics they were introduced 1963 by Glauber [74], as being the most adequate quantum mechanical description of an ideal laser beam.

The Wigner function for a coherent state is a displaced rotationally symmetric two-dimensional Gaussian:

$$W(x,y) = \exp\left(-(x - e_0 \cos\phi)^2 - (y - e_0 \sin\phi)^2\right) . \tag{2.18}$$

For the density matrix in the Fock representation we find using Eq. 2.15

$$\rho_{nm} = \frac{1}{\sqrt{2^n 2^m n! m!}} \, e_0^n \, e_0^m \, \mathrm{e}^{-\frac{e_0^2}{2}} . \tag{2.19}$$

The diagonal elements show the well known Poissonian statistics, with the characteristic property that its variance is equal to its mean value

$$\sigma_n^2 = \langle\, n^2 \,\rangle - \langle\, n \,\rangle^2 = \langle\, n \,\rangle = |\alpha|^2 = \frac{e_0^2}{2} . \tag{2.20}$$

Squeezed states

The class of all minimum-uncertainty squeezed states arises from letting the squeezing operator

$$S(r) \equiv \exp\left[\frac{r}{2}\hat{a}^2 - \frac{r}{2}\hat{a}^{\dagger 2}\right] \ , \tag{2.21}$$

with $r \geq 0$ act on a coherent state $|\, \beta \,\rangle$: [4]

$$|\, \alpha, r \,\rangle = S(r) \, D(\beta) \, |\, 0 \,\rangle , \tag{2.22}$$

The amplitude after the interaction is given by $\alpha = \cosh r \, \beta - \sinh r \, \beta^*$. Thus its absolute value changes in dependence on the phase ϕ of the input state $\beta = 2^{-1/2} \ (e_0 \cos\phi + \mathrm{i} \, e_0 \sin\phi)$ from e_0 to $e_0 \sqrt{\mathrm{e}^{-2r} \cos^2\phi \, + \, \mathrm{e}^{2r} \sin^2\phi}$.

Since the squeezing operator transforms the quadratures according to

$$S^\dagger(r) \, X \, S(r) = X \mathrm{e}^{-r} \qquad \text{and} \qquad S^\dagger(r) \, Y \, S(r) = Y \mathrm{e}^{r} , \tag{2.23}$$

the state's uncertainties become squeezed in the X quadrature and anti-squeezed in the Y-quadrature. Fig. 2.1 illustrates this hyperbolic action of the squeezing operator in phase space.

[4] This state was originally called two-photon coherent state [280]. It is equivalent to a squeezed state, where the latter is usually defined by first letting the squeezing operator act on a vacuum state with a subsequent displacement [266].

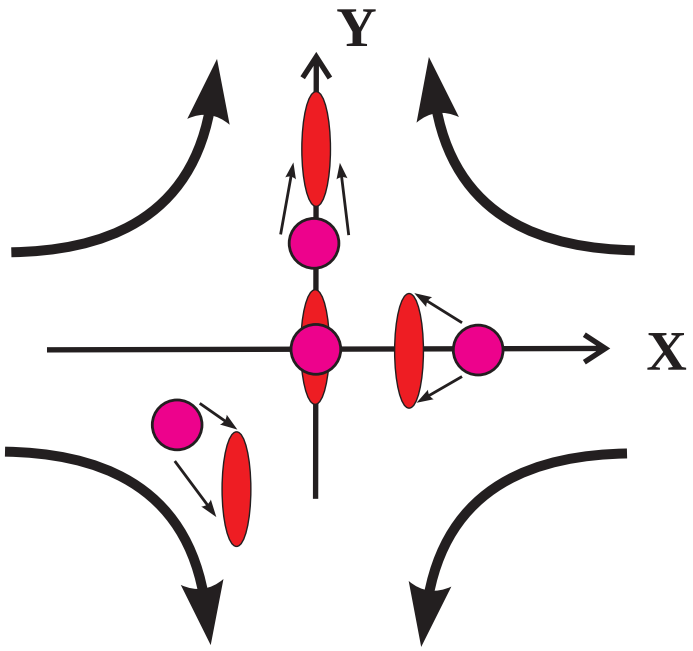

Figure 2.1: *Action of the squeezing operator in phase space. Shown are the uncertainty areas (contours of the Wigner functions) of the states before (coherent) and after (squeezed) the operator's action.*

The time evolution of the wave packet of a squeezed state is given by

$$|\psi(x,t)|^2 = \frac{1}{\sqrt{\pi}w(t)} \exp\left[-\frac{(x - (e_0 \cos(\omega t - \phi))^2}{w(t)}\right] , \tag{2.24}$$

with $w(t) = \sqrt{\mathrm{e}^{-2r}\cos^2(\omega t) + \mathrm{e}^{2r}\sin^2(\omega t)}$. The wave packet oscillates back and forth and in addition changes its width ("breathes") periodically.

The photon statistics of pure squeezed states has been analyzed in [235, 280, 214]. For the squeezed vacuum state the odd photon number probabilities vanish resulting in odd/even oscillations. For bright squeezed states, the photon statistics shows large scale oscillations, termed Schleich-Wheeler oscillations. Both features can be explained as arising from interference in phase space (see Sec. 3.4.5).

One complication for exact theoretical calculations is due to the fact that the squeezed states generated in the experiment are not pure states, as defined above, but mixed states due to the interaction of the light field with the environment (losses). This is equivalent to the fact that they are not minimum uncertainty states, i.e. $\Delta X \neq 1/\Delta Y$ (see Sec. 3.4.3). To abbreviate the notation in all following sections a^2 denotes the minimum and b^2 the maximum variance of the squeezed state (replacing e^{-2r} and e^{2r} resp.). The Wigner function for bright, non-minimum-uncertainty squeezed states is then given by

$$W(x,y) = \frac{1}{\pi ab} \exp\left(-\frac{(x - e_0\cos\phi)^2}{a^2} - \frac{(y - e_0\sin\phi)^2}{b^2}\right) . \tag{2.25}$$

A characteristic feature is the elliptical shape of its contours. With this expression the

density operator in the position basis is found to be

$$\rho(x+x', x-x') = \int_{-\infty}^{\infty} \mathrm{e}^{i2x'y}\, W(x,y)\,\mathrm{d}y \tag{2.26}$$

$$= \frac{1}{\sqrt{\pi}a} \exp\left[-\left(\frac{x - e_0\cos\phi}{a}\right)^2 - (bx')^2 + i2x'e_0\sin\phi \right] . \tag{2.27}$$

To calculate the matrix elements in the number state representation we use

$$\rho_{n,n+j} = \int\int \rho(x,y)\,\psi_n(x)\,\psi_{n+j}(y)\,\mathrm{d}x\mathrm{d}y\,, \tag{2.28}$$

with $\psi_n(x)$ defined by Eq. 2.13. In the general case of bright squeezed light ρ_{nm} is fairly complicated to calculate ([151]). In the following I will restrict myself to the squeezed vacuum state. In the case of a non-minimum-uncertainty state with $1/ab \neq 1$, this state is also called squeezed thermal state, since it can be thought of as being generated by squeezing a thermal state (see Ref. [151, 133]). This can be seen as follows: A thermal state of a harmonic oscillator of frequency ω with the temperature T and the mean occupancy $n_{_T} \equiv [\exp(\hbar\omega/k_{_B}T) - 1]^{-1}$ is described by the density operator (see section 3.7.2)

$$\hat{\rho}_{_T} \equiv \frac{1}{1+n_{_T}} \sum_{m=0}^{\infty} \left(\frac{n_{_T}}{1+n_{_T}}\right)^m |\, m\,\rangle\langle\, m\,|. \tag{2.29}$$

By applying the squeezing operator $S(r)$ we obtain in the position representation

$$\rho(x_1, x_2) = \langle\, x_1\,|\, S(r)\,\hat{\rho}_{_T}\, S^\dagger(r)\,|\, x_2\,\rangle \tag{2.30}$$

which yields exactly equation 2.27 with

$$a = \mathrm{e}^{-r}\sqrt{1+2n_{_T}}\,, \quad b = \mathrm{e}^{r}\sqrt{1+2n_{_T}} \qquad \text{and} \qquad e_0 = 0\,. \tag{2.31}$$

Using Eq. 2.28, the matrix elements of the squeezed thermal state are given by

$$\rho_{n,n+j} = \frac{1}{\pi a\sqrt{2^{2n+j}\,n!(n+j)!}} \int_{-\infty}^{\infty}\mathrm{d}x \int_{-\infty}^{\infty}\mathrm{d}y\, H_n(x)H_{n+j}(y) \exp\left(-A\,x^2 - A\,y^2 + 2C\,xy\right), \tag{2.32}$$

$$\text{with} \qquad A \equiv \frac{1}{2} + \frac{1}{4a^2} + \frac{b^2}{4} \qquad \text{and} \qquad C \equiv \frac{b^2}{4} - \frac{1}{4a^2}. \tag{2.33}$$

An alternative ansatz is the calculation of ρ via the Wigner function

$$\rho_{nm} = 2\pi \int_{-\infty}^{\infty}\mathrm{d}x \int_{-\infty}^{\infty}\mathrm{d}y\; W(x,y)\,W_{nm}(x,y)\,, \tag{2.34}$$

where

$$W_{nm}(x,y) = \frac{1}{2\pi}\int_{-\infty}^{\infty}\mathrm{d}x'\,\psi_m(x - \frac{x'}{2})\,\psi_n(x + \frac{x'}{2})\,\exp\left(ix'y\right) \tag{2.35}$$

$$= \frac{(-1)^m}{\pi}\sqrt{\frac{2^n m!}{2^m n!}}(x-iy)^{n-m}\exp[-(x^2+y^2)]L_m^{n-m}(2x^2+2y^2)$$

is the Wigner function of the projection operator $|n+j\rangle\langle n|$, L_m^{n-m} are the generalized Laguerre polynomials, and $\psi_n(x)$ are the energy eigenfunctions defined in Eq. 2.13.

Both integrals are solved by the associate Legendre function P_n^m of degree n and order m. Hence the Fock representation of the density operator of the squeezed thermal state reads

$$\rho_{n,n+2k+1} = 0 \qquad \text{and} \tag{2.36}$$

$$\rho_{n,n+2k} = \frac{(-1)^{-k/2}2}{\sqrt{(a^2+1)(b^2+1)}}\sqrt{\frac{n!}{(n+2k)!}}\,\xi^{n+k}P_{n+k}^k(\zeta) \tag{2.37}$$

with

$$\xi \equiv \left[\frac{(a^2-1)(b^2-1)}{(a^2+1)(b^2+1)}\right]^{1/2} \qquad \text{and} \qquad \zeta \equiv \frac{a^2b^2-1}{\sqrt{(a^4-1)(b^4-1)}}. \tag{2.38}$$

For the photon number distribution we get

$$p_n = \rho_{nn} = \frac{2}{\sqrt{(a^2+1)(b^2+1)}}\xi^n P_n(\zeta), \tag{2.39}$$

where $P_n \equiv P_n^0$ is the Legendre polynomial of degree n. Note that both ξ and ζ are purely imaginary, since $a^2 < 1$. Altogether the i's cancel out, due to the structure of the Legendre polynomials, so that ρ_{nm} is a real number. As a result of this cancellation the signs of the coefficients of the Legendre polynomials, which are usually strictly positive, are alternating in Eq. 2.37.

The non-classicality of the squeezed thermal state has its manifestation in the odd-even oscillation of the diagonal and even off-diagonal elements $\rho_{n,n+2k}$ (see Fig. 3.19). This oscillation has its origin in the two-photon generation process since the Hamiltonian is quadratic in the creation and annihilation operators. Note that for mixed states with $1/a \neq b$ the odd diagonal elements do not vanish completely (see Fig. 3.16 in the experimental part). Thus the two-photon correlation is reduced by the coupling to the outer environment. That the odd off-diagonal elements $\rho_{n,n+2k+1}$ are equal to zero is not a sign of non-classicality, but simply reflects the symmetry of the state in phase space $W(x,y) = W(-x,-y)$ (see Fig. 3.19). A further discussion of this matrix is given in Sec. 3.4.

2.3 The measurement method

How is the quantum state of an optical wave determined? The measurements to be performed on the state are measurements of the electric field operator

$$E(\theta) \propto X_\theta = X\cos\theta + Y\sin\theta \tag{2.40}$$

at all phase angles θ.

To experimentally access the electric field, which oscillates with a frequency $\omega/2\pi$ of hundreds of THz, a balanced homodyne detector [281, 1, 223, 283, 191] is employed.

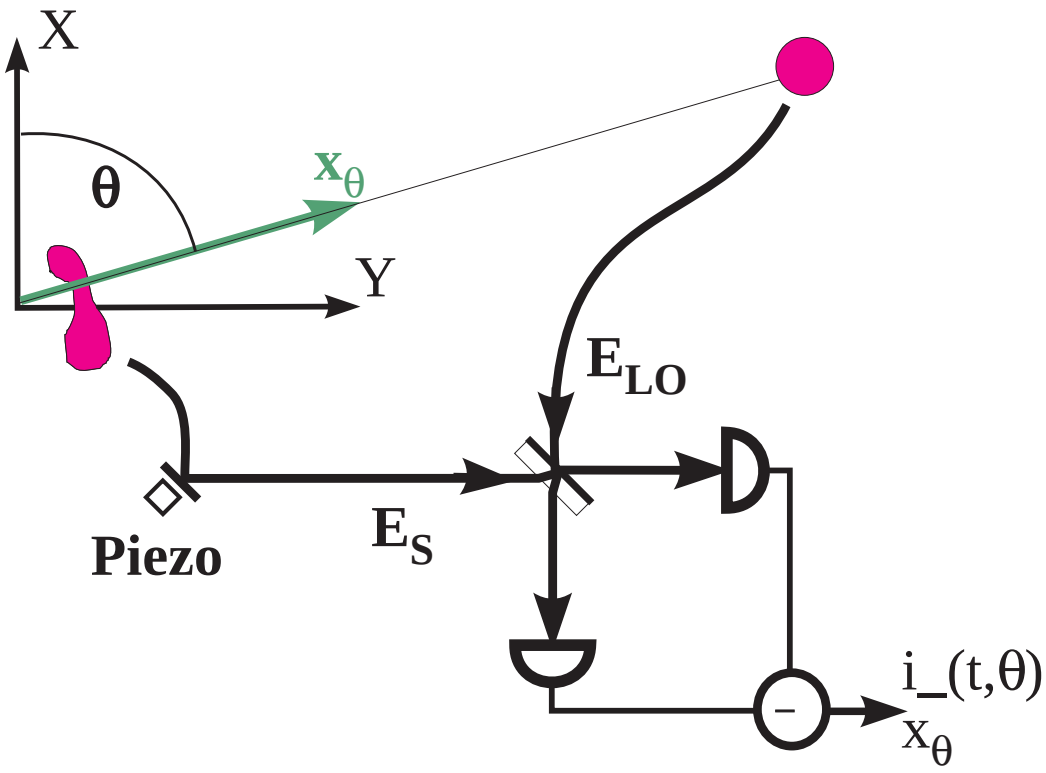

Figure 2.2: *Scheme of balanced homodyne detection. To the left, the phase space representations of the unknown signal state and the strong coherent local oscillator are shown. The phase angle θ between the two is the angle of measurement. The two corresponding waves E_S and E_{LO} are overlapped at a beam splitter. The subtracted photocurrents of two detectors at the two beam splitter output ports yield a current proportional to the signal's electric field quadrature X_θ. By varying the angle θ via a piezoelectric shift of a mirror in the beampath of either one of the two waves, the signal state can be observed from all possible directions in phase space.*

Herein the signal wave is spatially overlapped at a 50/50 beam splitter with a strong coherent local oscillator wave of nearly the same frequency. The two fields emerging from the beam splitter are the sum and the difference of the signal and local oscillator fields. By subtracting the photocurrents of two detectors at the two beam splitter output ports, the natural oscillation of the signal state under investigation is converted to a low frequency electrical signal i_-, directly proportional to X_θ (calculations see Sec. 3.1.7). The angle θ is the relative phase between signal and local oscillator. It is varied linearly in time by a movable mirror in the beampath of one of the two waves.

A large number of measurements of the observable X_θ yields the probability distribution $P_\theta(x_\theta)$ of its eigenvalues x_θ. The relation between the measured distributions and the density operator ρ is

$$P_\theta(x_\theta) = \langle\, x \,|\, U^\dagger(\theta)\, \hat{\rho}\, U(\theta) \,|\, x \,\rangle, \tag{2.41}$$

where $U(\theta) = \exp(-i\theta \hat{a}^\dagger \hat{a})$ performs a rotation in phase space. Since the optical state evolves freely with frequency ω, U is equivalent to the time evolution operator with

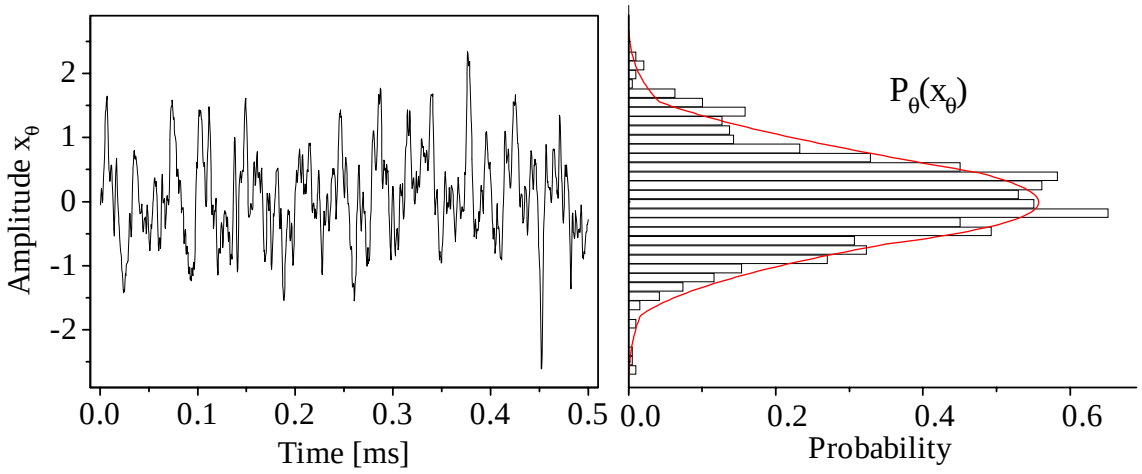

Figure 2.3: *Measurement of the vacuum noise by balanced homodyne detection. The figure right shows the wave packet sampled from the noise measurement left. A Gaussian fit (solid line) is shown for comparison. The variance of the Gaussian determines the noise level of the vacuum.*

$\theta = \omega t + const.$, and the θ-dependence of P_θ is equivalent to the time dependence of the position probability density of the state (i.e. of $|\,\psi(x,t)\,|^2$, if $\hat{\rho} = |\,\psi\,\rangle\langle\,\psi\,|$ is a pure state). In this way the rapid oscillation of the free time evolution of the electric field operator $E(t) \propto X\cos\omega t + Y\sin\omega t$ is converted to a controlled phase dependence $E(\theta) \propto X_\theta$. Thus, assuming that the signal state (i.e. its wave vector or density matrix) emitted by the source does not change during the measurement time, the noise current $i\_(t)$ and correspondingly the distributions $P_\theta(x_\theta)$ furnish an image of the time evolution of the signal wave.

2.3.1 Quantum tomography

As shown in Fig. 2.4 the measured distributions $P_\theta(x_\theta)$ are the marginal distributions of the Wigner function, integrated along a rotated coordinate axis $y_\theta = -x\sin\theta + y\cos\theta$:

$$P_\theta(x_\theta) = \int_{-\infty}^{\infty} W(x_\theta\cos\theta - y_\theta\sin\theta, x_\theta\sin\theta + y_\theta\cos\theta)dy_\theta\,, \tag{2.42}$$

This is a generalization of the condition given in Eq. 2.8. Thus, the measured distribution functions are the density projections of the Wigner function. The integral 2.42 is also called Radon transform. It can be readily inverted by use of the inverse Radon transformation [188]. This way the Wigner function can be reconstructed from the measured data [13, 259, 229]. In more detail this is described in section 3.3.

An alternative reconstruction method for $W(x,y)$ with a special integral kernel is given in [53]. A third method to gain $W(x,y)$ via summation over the density matrix elements ρ_{nm} is outlined below.

To obtain the density matrix elements in the Fock representation ρ_{nm} we have to invert Eq. 2.41. This is done by integrating the measured distributions over a set of pattern functions f_{nm}, which is carried out in section 3.4. The pattern functions were first found by D'Ariano [51]. Subsequent analytical improvements lead to the very useful

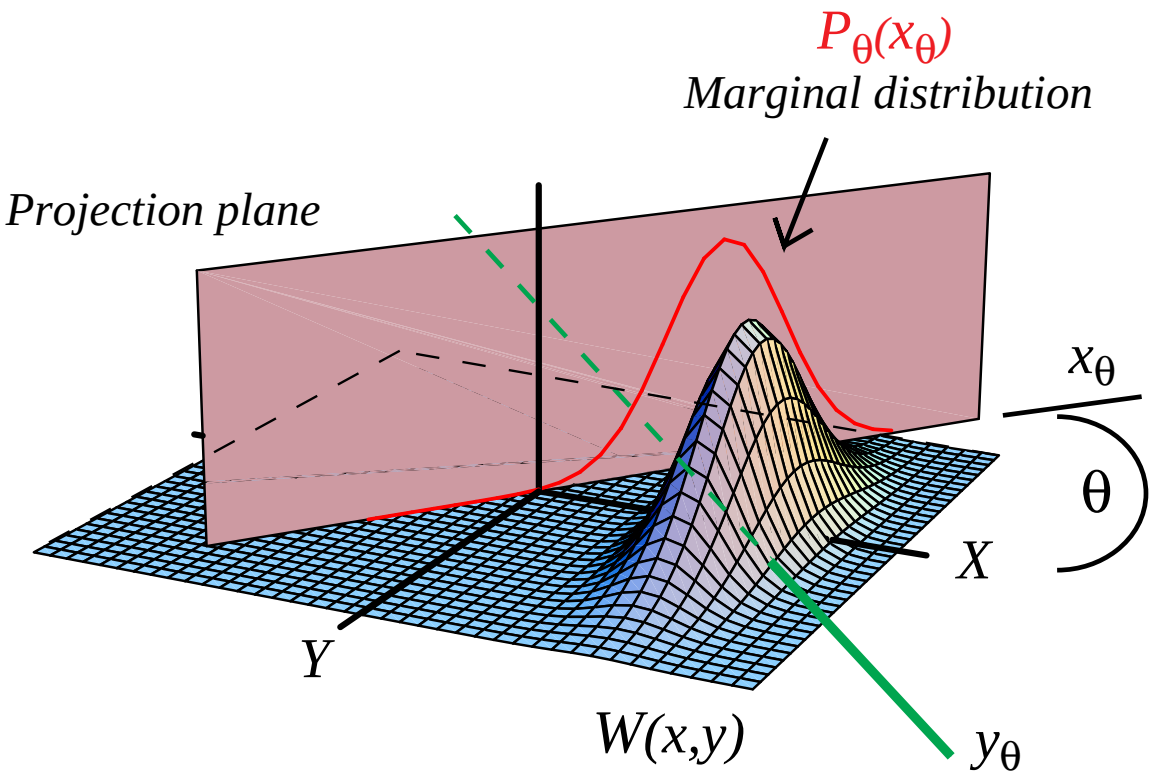

Figure 2.4: *The Wigner function and its density projection. Tomography is a general method to infer the shape of an inaccessible object (in this case the Wigner function) from its projections (the quadrature distributions $P_\theta(x_\theta)$) under various angles.*

description in [135]. The most detailed analysis can be found in the book of U. Leonhardt [137] (see also the review article [123]).

Once the density matrix elements are known, the distribution of any other quantum mechanical observable may be derived. This is described for the phase distributions in Sec. 3.4.6 and the joint number-phase distribution in Sec. 3.4.7. Other relevant evaluations employing ρ_{nm} are the determination of the mean and variance of the photon number distribution and the state's purity (Sec. 3.4.3).

As mentioned above, it is also possible to obtain the Wigner distribution $W(x,y)$ by a summation over the density matrix elements ρ_{nm}. Using the definition Eq. 2.6, and inserting ρ in the Fock basis given by Eq. 3.15 results in

$$W(x,y) = \sum_{m,n} \rho_{mn} W_{nm}(x,y) \tag{2.43}$$

where $W_{nm}(x,y)$ is defined by Eq. 2.36. Since the dominant errors in the experimental part (see Sec. 3.4.3) are systematical or statistical ones and not due to the reconstruction method, I have so far only employed the inverse Radon transform for the evaluation of $W(x,y)$.

2.3.2 Alternative measurement methods

By now there exists a variety of other reconstruction algorithms that transform the probability distributions $P_\theta(x_\theta)$ measured via homodyning into the density matrix [290, 53,

241, 172, 96, 9, 173]. The application of some of them to the data measured in this thesis is presented in section 3.5. In contrast to this, only few principally different measurement schemes have been proposed that may provide a complete description of the light field's quantum state as well. These are eight port homodyning for Q-function measurements [263, 137], also used for the determination of the quantum optical phase [169], unbalanced homodyning [264], and direct photon counting [7] (see also Sec. 3.5.3), which can be combined with photon chopping [178] to possibly provide an experimentally feasible measurement method.

2.4 Cavity equations for the parametric amplifier

One way of realizing a quadratic interaction Hamiltonian such as the squeezing operator of Eq. 2.21 is the two-photon generation process of parametric down-conversion [161, 266]. A strong pump wave of frequency 2ω interacts with a weak signal field (in the limit with zero amplitude, vacuum) of frequency ω. The pairwise creation of photons in the signal field occurs by splitting a 2ω photon into 2 photons of frequency ω. The interaction between pump wave and signal wave takes place in a medium with a polarizability $\mathbf{P}$ which exhibits a nonlinear dependency from the electric field $\mathbf{E}$

$$P_i = \epsilon_0 \chi^{(1)}_{ij} E_j + \epsilon_0 \chi^{(2)}_{ijk} E_j E_k + \epsilon_0 \chi^{(3)}_{ijkl} E_j E_k E_l + ... \tag{2.44}$$

Since the relevant nonlinear term $\chi^{(2)}_{ijk}$ is usually very weak, in the order of $10^{-12}\, m/V$, the interaction is enhanced by employing an optical cavity.

In the following considerations the cavity is assumed to be a standing wave cavity, singly resonant for the subharmonic wave, with one output port of transmission T, internal losses A, and length L, resulting in a roundtrip time $\tau = 2L/c$. The injected subharmonic and harmonic waves are denoted by $\alpha_{\rm in}$ and $\beta_{\rm in}$ and the outcoming waves by $\alpha_{\rm out}$ and $\beta_{\rm out}$ respectively. Assuming zero detuning, the equation of motion for the subharmonic intracavity field α can be derived, using the standard field equations in nonlinear media (see [279] and [212]):

$$\frac{{\rm d}\alpha}{{\rm d}t} = -(\gamma_l + \gamma_c)\,\alpha + \sqrt{2\gamma_c}\,\alpha_{\rm in} - \mu\alpha^*\alpha^2 + 2\sqrt{\mu}\,\alpha^*\,\beta_{\rm in} \tag{2.45}$$

Here $\gamma_c = (1-\sqrt{1-T})/\tau$ is the damping rate due to the input coupler transmission and $\gamma_l = (1-\sqrt{1-A})/\tau$ that due to other cavity losses. The strength of the interaction is given by the nonlinear coupling parameter $\mu = \hbar\omega E_{\rm NL}/2\tau^2$, where $E_{\rm NL}$ is the effective nonlinearity, described in more detail in Sec. 3.1.3. The coupling term $2\sqrt{\mu}\,\alpha^*\beta_{\rm in}$ is responsible for the phase-sensitive parametric generation, the third order term higher power effects such as cascaded nonlinear interactions [271] and finite limiting values for parametric amplification. The input-output relations

$$\beta_{\rm out} = \beta_{\rm in} - \sqrt{\mu}\alpha^2 \qquad \alpha_{\rm out} = -\alpha_{\rm in} + \sqrt{2\gamma_c}\alpha^2 \tag{2.46}$$

complete the description of the system. The measured input/output powers are related to the normalized field amplitudes by

$$P_{1,\rm in} = \hbar\omega\,|\,\alpha_{\rm in}\,|^2\,, \qquad P_{1,\rm out} = \hbar\omega\,|\,\alpha_{\rm out}\,|^2\,, \tag{2.47}$$

$$P_{2,\rm in} = 2\hbar\omega\,|\,\beta_{\rm in}\,|^2\,, \qquad P_{2,\rm out} = 2\hbar\omega\,|\,\beta_{\rm out}\,|^2\,, \tag{2.48}$$

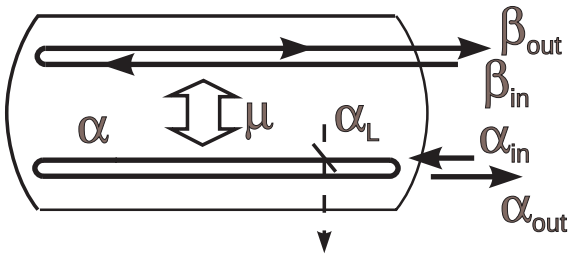

Figure 2.5: *Schematic of the nonlinear interaction inside a resonator between the resonant subharmonic wave α and the harmonic wave β.*

whereas the circulating power is given by $P_1 = \hbar\omega\,|\,\alpha\,|^2/\tau$. Thus $|\,\alpha_{\rm in/out}\,|^2$ and $|\,\beta_{\rm in/out}\,|^2$ are normalized to a photon rate and $|\,\alpha\,|^2$ to the number of intracavity photons.

Stationary solutions for the classical analysis of the OPO threshold and the gain of parametric amplification and deamplification are found by setting $\mathrm{d}\alpha/\mathrm{d}t$ equal to zero. A semiclassical analysis of the quantum noise can be carried out by linearizing Eq. 2.45 for small fluctuations [49]

$$\alpha = \bar{\alpha} + \Delta\alpha\,. \tag{2.49}$$

Neglecting the third order term for small circulating field strengths and noting that an additional incoupling term $\Delta\alpha_{\rm L,in}$ arises from the vacuum fluctuations entering the cavity due to the internal losses, we arrive at

$$\Delta\dot{\alpha} = -(\gamma_l + \gamma_c)\,\Delta\alpha + \sqrt{2\gamma_c}\,\Delta\alpha_{\rm in} + \sqrt{2\gamma_l}\,\Delta\alpha_{\rm L,in} + 2\sqrt{\mu}\,\beta_{\rm in}\,\Delta\alpha^* \tag{2.50}$$

The relation of quadrature fluctuations to the fluctuations of the field amplitudes is given by

$$\Delta X = \frac{1}{\sqrt{2}}\,(\Delta\alpha + \Delta\alpha^*) \qquad \text{and} \qquad \Delta Y = \frac{1}{\sqrt{2i}}\,(\Delta\alpha - \Delta\alpha^*)\,. \tag{2.51}$$

Taking the Fourier transform of Eq. 2.50 and using the input/output relations, we find

$$\begin{aligned}
\Delta X_{\rm out} &= \frac{\gamma_c - \gamma_l - \epsilon - \mathrm{i}\Omega}{\gamma_c + \gamma_l + \epsilon + \mathrm{i}\Omega}\Delta X_{\rm in} + \frac{2\sqrt{\gamma_c\gamma_l}}{\gamma_c + \gamma_l + \epsilon + \mathrm{i}\Omega}\Delta X_{\rm L,in} \\
\Delta Y_{\rm out} &= \frac{\gamma_c - \gamma_l + \epsilon - \mathrm{i}\Omega}{\gamma_c + \gamma_l - \epsilon + \mathrm{i}\Omega}\Delta Y_{\rm in} + \frac{2\sqrt{\gamma_c\gamma_l}}{\gamma_c + \gamma_l - \epsilon + \mathrm{i}\Omega}\Delta Y_{\rm L,in}\,,
\end{aligned} \tag{2.52}$$

where $\epsilon = 2\sqrt{\mu}\beta_{\rm in}$ With input variances of 1 and no correlations between different quadratures we obtain for the spectra of squeezing $\Psi_- = |\Delta X_{\rm out}|^2$ and anti-squeezing $\Psi_+ = |\Delta Y_{\rm out}|^2$

$$\Psi_\pm(\Omega, P) = \Psi_0\left(1 \pm \xi\,\frac{4\,d}{(1 \mp d)^2 + (\Omega/,\,)^2}\right)\,. \tag{2.53}$$

Here $, = \gamma_c + \gamma_l$ is the linewidth (HWHM) of the cavity without nonlinear losses, $d = \sqrt{P/P_{th}}$ is the pump parameter with a pump power $P = P_{2,in}$ and a threshold power $P_{th} = 2\hbar\omega|\beta_{th}|^2 = \hbar\omega,\,^2/2\mu$ of the OPA, $\Psi_0 = 1$ is the spectral density of the vacuum state, and $\xi = \gamma_c/,$ is the escape efficiency of the resonator. The detection efficiency η can be modelled equivalently to the internal losses by a beam splitter with vacuum input

placed between the detector and the cavity output. Including η in the calculations leads to a replacement of the factor ξ by $\xi \cdot \eta$ in Eq. 2.53. Finally note that, regarding the linewidth, the nonlinear coupling results in a line broadening (parametric deamplification) or line narrowing (parametric amplification) dependent on the relative phase between injected signal wave and pump wave, so that the effective linewidth changes to , $_e = (\gamma_c + \gamma_l)(1 \pm d)$ [219].

3 Experiment I: States of the light field

3.1 The setup

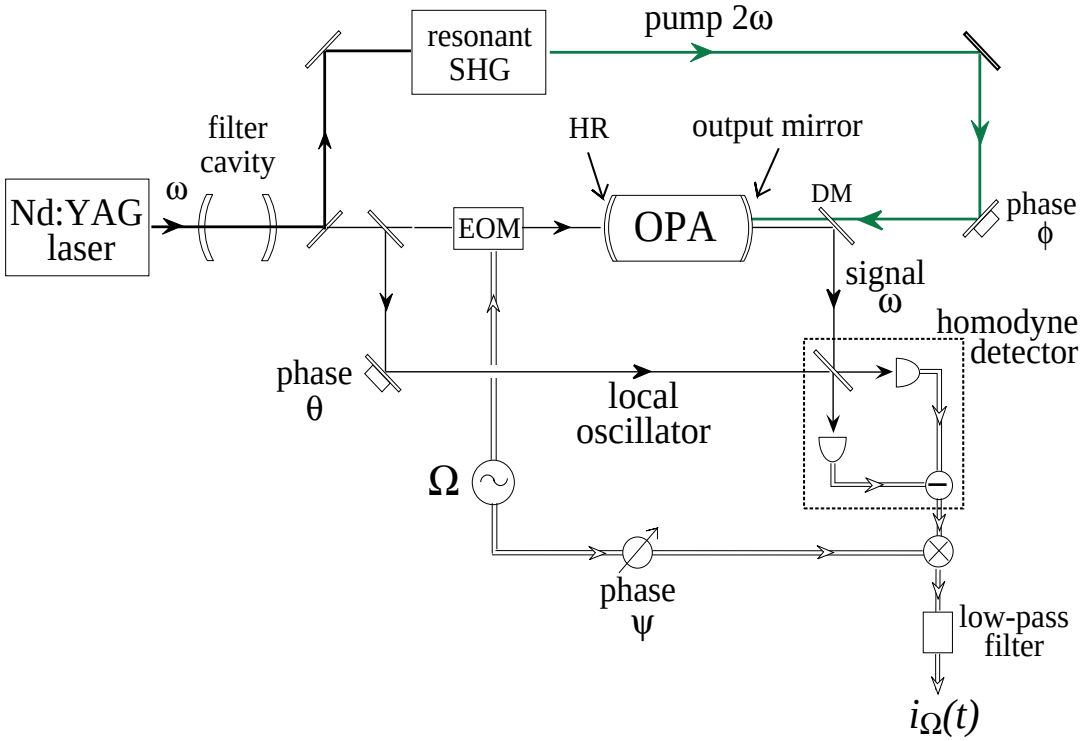

Figure 3.1: *Experimental scheme for generating bright squeezed light and squeezed vacuum with an OPA. The electric field quadratures are measured in the homodyne detector while scanning the phase θ. A computer performs the statistical analysis of the photocurrent i_Ω and calculates the quantum states. EOM: electro-optic modulator, DM: dichroic mirror.*

A schematic of the experiment is shown in Fig. 3.1. A miniature monolithic Nd:YAG laser (1064 nm, 500 mW, Lightwave 122) was employed as the laser source. To reduce the excess noise of the laser resulting from the relaxation oscillations, the laser beam first traverses a high finesse mode cleaning cavity. It is then split into three parts and directed to the homodyne detector as the local oscillator, to the frequency doubler to generate the pump wave for the OPA, and to the OPA for injection-seeding. The ouput wave of the OPA is subsequently recorded by the homodyne detector.

3.1.1 The mode cleaner

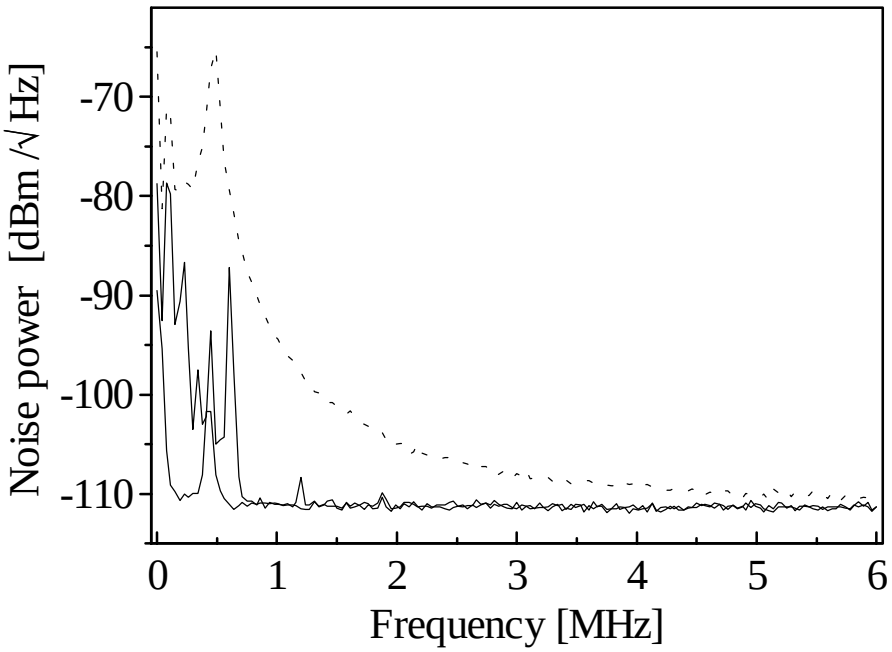

Figure 3.2: *Spectral density of the amplitude noise of the diode-pumped Nd:YAG laser as a function of frequency, recorded with a homodyne detector without local oscillator. Shown are the spectral noise densities before (dotted) and after (solid) the filter cavity. The third trace at the bottom refers to the vacuum noise for both cases. The peak at 500 kHz is due to the relaxation oscillation of the laser. The second peak at 600 kHz of the trace after the filter cavity is the frequency modulation used for locking the cavity. The resolution bandwidth was 10 kHz.*

The mode-cleaning cavity consists of two high finesse mirrors (radius of curvature 1000 mm) coated by Research Electro Optics, Boulder and an 8 cm spacer made of Invar (Goodfellow, Cambridge), to avoid longtime cavity drifts due to changes in the room temperature. One of the mirrors was mounted on a piezoelectric actuator, to be able to stabilize the cavity length to the laser frequency via the Pound-Drever locking technique [59, 91]. To obtain the error signal, the laser itself was phase-modulated at frequencies $<$900 kHz. The linewidth of the cavity was measured to be 170 kHz, which is equivalent to a finesse of 10 400.

The effect of the mode cleaner can be seen in Fig. 3.2. The amplitude excess noise of the laser around 1 MHz was reduced by more than 15 dB. Although the cavity was not kept in vacuum and circulating light powers were in the order of some kW, no reduction of the finesse within 2 years of operation was observed.

A new proposal for the usage of the mode cleaning cavity, not carried out in this thesis, would be the spatial analysis of the light field [142]: In the first preliminary experimental setup [28] the mode cleaner was not placed directly after the laser, but in the beam path of the local oscillator right before the homodyne system. This way by using higher TEM-modes of the resonator the spatial structure of the signal beam could be investigated.

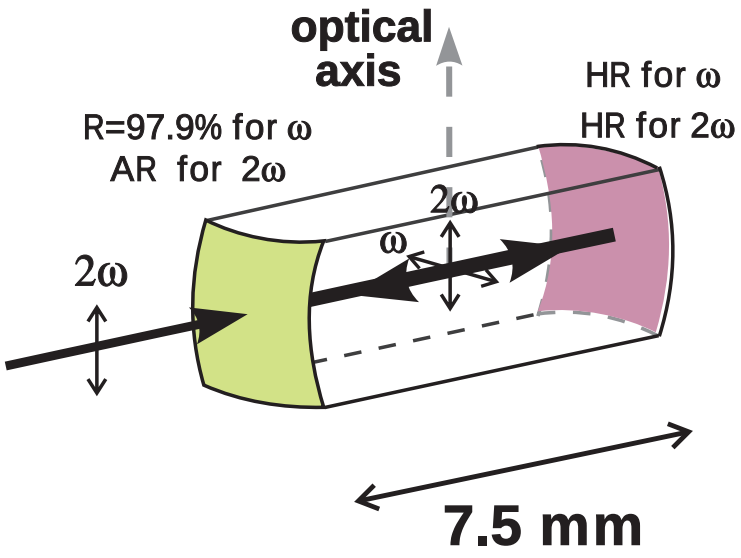

Figure 3.3: *Sketch of the monolithic OPA, the center piece of the experiment.*

3.1.2 The frequency doubler

The semi-monolithic doubler cavity consists of a 7.5 mm long crystal made of magnesium-oxide-doped lithium niobate (MgO:$LiNbO_3$) with one flat and one $R_1 = 10$ mm spherical endface and an $R_2 = 25$ mm input coupler mirror (AR(532nm), $T(1064\text{ nm}) = 3.5\,\%$) mounted on a piezoelectric actuator. The back coating of the crystal is HR for both 1064 nm and 532 nm. A frequency-locking circuit is used to lock the cavity to the laser frequency. A modified Pound-Drever technique is employed, with electro-optic modulation of the crystal itself. When optimized, the frequency doubler generates a 532 nm pump wave with up to 200 mW power at 70 % conversion efficiency. Typically, the doubler is operated with non-optimal mode-match of the input wave, emitting 150 mW at 532 nm with 300 mW input power at 1064 nm. By varying the laser frequency, the harmonic frequency is continuously and rapidly tunable over 20 GHz.

3.1.3 The OPA

The OPA consists of a monolithic standing wave cavity, made of magnesium-oxide-doped lithium niobate. Besides the experiments described here, the same crystal served as a highly efficient frequency converter [177, 29, 213]. The endfaces of the crystal of length $L = 7.5$ mm are polished spherically with 10 mm radii of curvature. One end of the crystal is coated with a high reflector at both 1064 ($T_{HR} < 0.05\%$) and 532 nm, the other side is the output coupler with transmittivity $T_o = 2.1\%$ at 1064 nm and high transmission at 532 nm. With this configuration, the nonresonant pump double passes the resonator to enhance the nonlinear coupling, so that the threshold is reduced [14]. The measured linewidth of the OPA is 2, = 35 MHz (FWHM), which, considering the free

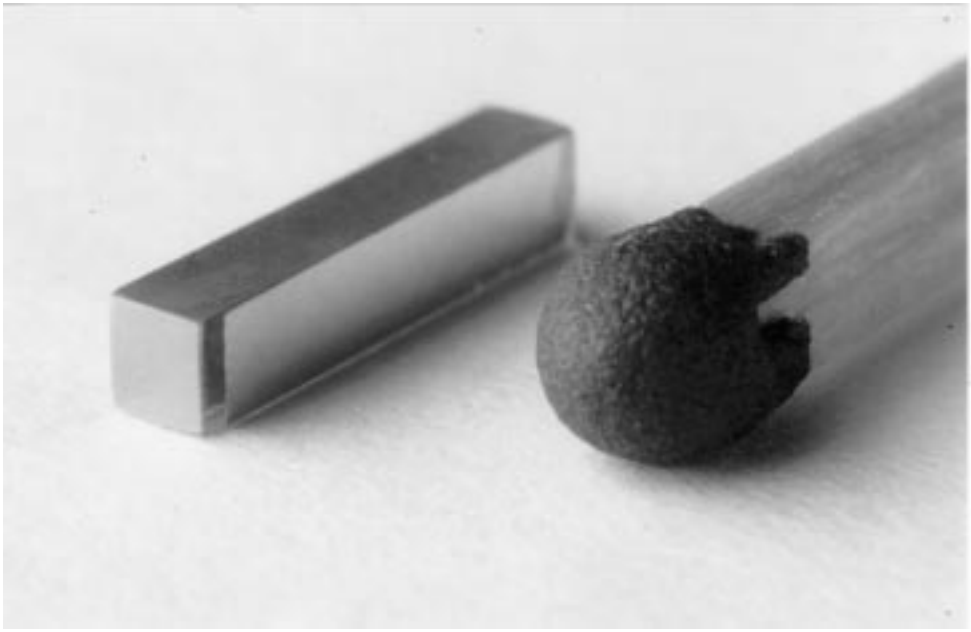

Figure 3.4: *Photograph of the monolithic OPA. A match is shown for comparison.*

spectral range of 9 GHz, gives a finesse of 260 and roundtrip losses A of $\approx 0.3\%$ The faces perpendicular to the crystal c-axis are coated with gold for electrooptic modulation. The resonator is embedded in an aluminum oven whose temperature of $\approx 120°\mathrm{C}$ is actively controlled to 10 millikelvin. The OPA is operated in degenerate mode, i.e. the resonance frequency of the cavity mode is half the frequency of the pump wave, and the parametric gain of the nonlinear crystal is maximized via its temperature.

The threshold power for the onset of degenerate parametric oscillation is derived from Eq. 2.45 to be

$$P_{\mathrm{th}} = \frac{\pi^2}{\mathcal{F}^2 E_{\mathrm{NL}}}, \tag{3.1}$$

with an effective nonlinearity

$$E_{\mathrm{NL}} = \frac{2\omega^3 d_{\mathrm{eff}}^2}{\pi n^2 c^4 \epsilon_0} L\, h(\Delta k, \xi), \tag{3.2}$$

where $h(\Delta k, \xi)$ is the Boyd-Kleinman factor [21], Δk is the phase mismatch, $\xi = L/2z_R$ is the focussing parameter, and z_R is the Raleigh range. With waists of $27\,\mu$m for the ω and $19\,\mu$m for the 2ω wave, h equals 0.655 under phase matching conditions. E_{NL} is determined by measurements of frequency doubling at low input powers, where the relation $P_{2\omega} = E_{\mathrm{NL}} P_\omega^2$ holds. With a nonlinear coefficient of $d_{\mathrm{eff}} \approx 5$ pm/V, a threshold power of $P_{\mathrm{th}} = 28$ mW is calculated, which agrees with the lowest measured values.

The escape efficiency of the OPA cavity, determining roughly speaking the fraction of quantum noise that is emitted, is calculated to be $\xi = T_o/(T_o + T_{HR} + A) = 0.88$. Since the very same factor is found to be the upper limit for the maximum achievable conversion efficiency, the previous experiments involving the OPA as a highly efficient frequency doubler [177] and as a highly efficient OPO [29] confirm this value for ξ.

Although in the beginning of the experiment the laser frequency was stabilized to the OPA cavity resonance by a frequency shifted reference beam exciting a higher order transversal mode of the OPA, the excellent free running frequency stability of the laser, the dimensional stability of the OPA cavity and its broad linewidth allow frequency stable operation of the experiment without active stabilization, relative drifts being less than 10 MHz/min (at constant room temperature even less than 10 MHz/hour).

Three optical isolators (not shown in Fig. 3.1) prevent backreflection of the laser light from the filter cavity into the laser, from the standing-wave frequency doubler into the filter cavity and from the OPA into the frequency doubler.

3.1.4 Parametric amplification and deamplification

A central aspect of the experiment is the generation of bright squeezed light, i.e. squeezed light with a coherent excitation. An efficient method to achieve this consists of using the OPA in a dual-port configuration [221]: A weak seed wave is injected into the HR mirror and the bright squeezed light is extracted from the output port.

To characterize the OPA we first investigated the classical effects. If the seed wave of power P_{in} at ω is on resonance with the cavity, then $P_s = 4P_{in}T_oT_{HR}/(T_o + T_{HR} + A)^2$ is the output power transmitted by the OPA cavity through the T_o mirror in absence of the pump. Once the pump is turned on, the output power gP_s has a gain g which depends on the power and the phase of the pump. Using Eq. 2.45, the strongest deamplification factor is found as

$$g_{min} = \frac{1}{(1 + \sqrt{P_p/P_{th}})^2}. \tag{3.3}$$

Note that it is independent of the seed power and does not explicitly depend on the mirror transmissivities. Fig. 3.5a shows the agreement of this expression with the experimentally measured g_{min}. The deamplification limit at threshold is 1/4 independent of the employed resonator. The maximum amplification g_{max}, on the other hand, depends on seed power since it is limited by the depletion of the pump. At a fixed seed power the measured maximum gain as a function of pump power is shown in Fig. 3.5b. By reducing the seed power the amplification factor can be increased. The inset of Fig. 3b shows this dependence with $P_p = 0.985 \cdot P_{th}$. Amplification factors up to 3200 were obtained. With a pump power exactly at threshold, the maximum gain is given by $g_{max} = (4\xi P_{th}/P_s)^{2/3}$. Note, however, that this gain factor cannot be directly used for signal amplification, since the injection of the seed wave through the HR port leads to high losses.

3.1.5 The homodyne system

From a technical perspective the homodyne system can be regarded as a lock-in detector for the signal field: The quantum noise at the optical frequency ω is mixed down to the electronically accessible RF range. This is achieved by overlapping the signal beam with a local oscillator beam at a 50/50 beam splitter and subsequently detecting the beams of the two output ports (Fig. 3.1).

The basic property of the homodyne detection system is a narrowband detection of the electric field fluctuations at frequencies offset from the local oscillator frequency ω by

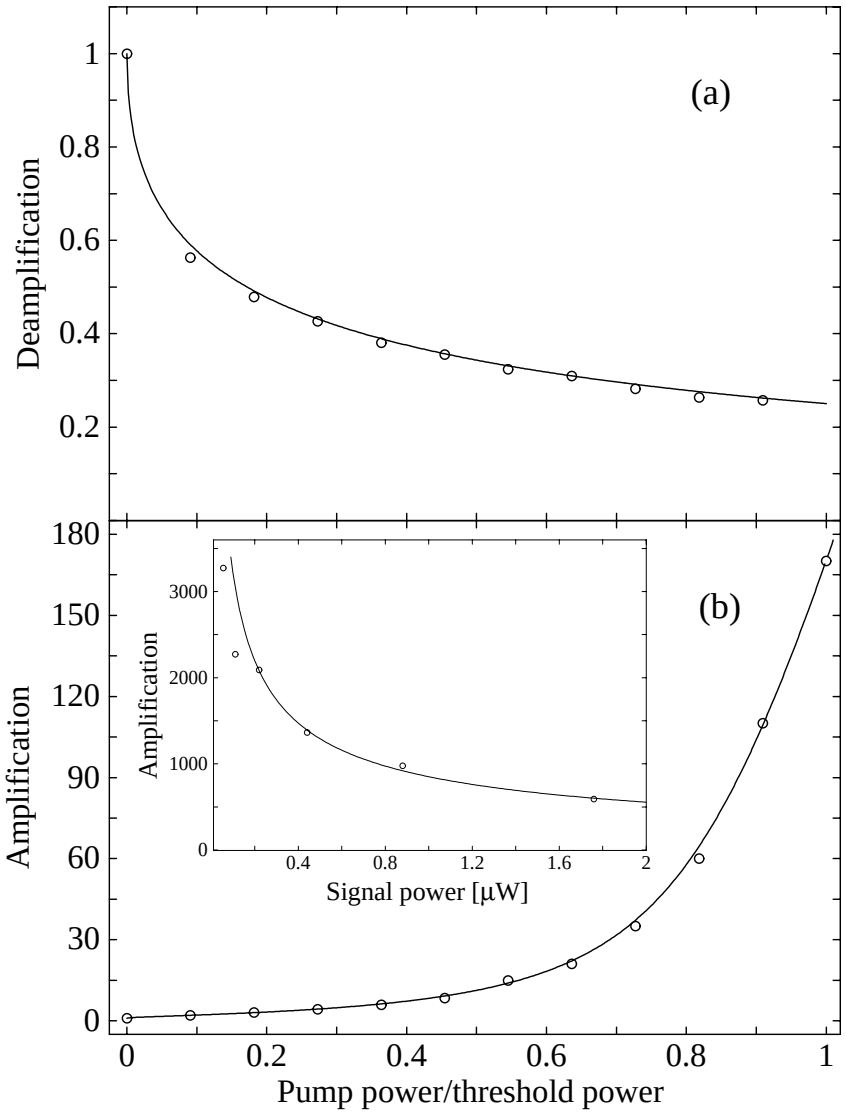

Figure 3.5: *Parametric deamplification (a) and amplification (b) of a weak signal injected into the OPA. The signal input power in (b) amounted to $P_{in} = 40\,\mu W$. Inset: Maximum amplification vs. signal input power at constant pump power $P_p \approx P_{th}$. Lines: Theory, Points: measured values.*

Ω=1.5 to 2.5 MHz, rather than at DC, to avoid technical noise at low frequencies. This means, that we detect the correlated signal and idler waves $\omega_{1,2} = \omega \pm \Omega$ of the OPA output wave, which are generated by the process of non-degenerate parametric down-conversion $2\omega \rightarrow \omega_1 + \omega_2$ (cf. Sec. 3.8). For measurements covering the whole spectral output of the OPA, leading to multiple mode reconstructions of the light field see section 3.9. The photodetectors contain passivated InGaAs photodiodes (ETX500, Epitaxx). The photocurrents are amplified by transimpedance amplifiers (NE5212, Valvo) with a bandwidth exceeding 30 MHz. The two output photocurrents are subtracted (added) to i_- (i_+) by a hybridjunction (Varil) with measured 40 dB common mode rejection. One part of the difference photocurrent is directed to a spectrum analyzer for variance

measurements, the other part is further amplified by a low-noise 40 dB gain amplifier and then mixed with an electrical oscillator of frequency Ω. The intermediate frequency output of the mixer is further amplified and low-pass filtered by a SRS 560 low-noise amplifier. The bandwidth is set to 100 kHz, defining the bandwidth within which the fluctuations of i_- are detected. The suppression of a strong modulation applied to the local oscillator is better than 20 dB. The shot noise level, determined by comparing i_+ and i_- when the open port of the beam splitter has vacuum input, is accurate to 0.3 dB for a wide range of frequencies. When the balancing of power in the two detectors is optimized for a particular frequency, the accuracy is on the order of 0.2 dB. At a local oscillator power of 2 mW the shot noise level is 14 dB above the electronic noise level of the detectors at lower frequencies and 5 dB for frequencies above 24 MHz.

The detection efficiency

Not only to detect high degrees of quantum noise supression but also to ensure the faithfulness of the quantum state reconstructions, detection efficiency is a crucial issue in our experiment. A thorough discussion of detection efficiency of an experimental homodyne system is found in the excellent article by Wu and Kimble [276].

The overall losses suffered by a quantum state emitted by the OPA until it is recorded can be summarized by $\xi \cdot \eta$, where ξ, defined in section 3.1.3, is the cavity escape efficiency resulting from the losses occurring inside the optical cavity and η is the detection efficiency, consisting of the following three factors: modematching efficiency, propagation efficiency and photodetection efficiency.

The modematching efficiency is defined to be the square of the integral over the spacial extension of the product of local oscillator and signal wave at the beam splitter of the homodyne system. To maximize the mode overlap, the homodyne system was mounted in such a way that besides the beam's direction, the size as well as the position and magnitude of the two beam waists could be controlled independently via micrometer translation stages. Focused beams were found to be easier to adjust than parallel propagating ones. A modematching efficiency of more than 99% was obtained by measurement of the fringe visibility produced from the interference of local oscillator and OPA cavity transmission of an injected signal beam.

For the photodiodes the producer Epitaxx specifies a typical value for the spectral response $R = \textit{generated photocurrent}\ [A]\,/\,\textit{light power}\ [W]$ of 0.90 at 1300 nm. Since each individual diode is tested by the manufacturer, it is possible to choose for the quantum noise measurements those with higher responsivity (0.95-0.99) than the average. According to the manufacturers data sheet the spectral response is almost flat in the wavelength range 1000 – 1300 nm, so the best expected quantum efficiencies at 1064 nm amount to $\eta_q = R\hbar\omega/e = 96\,\%$.

The quantum efficiency was measured by directly monitoring the produced current of the diode, as well as by measuring the amplified current of the photodetector output, rescaling the result by the known (measured) amplification factor of the detectors electronic circuit. By both methods we obtained values between 95% and 97%, using a Laser Instrumentation thermopile for calibration of the light power. The published 97±2% are overestimated, and should be replaced by 96±2%. After three months operation at po-

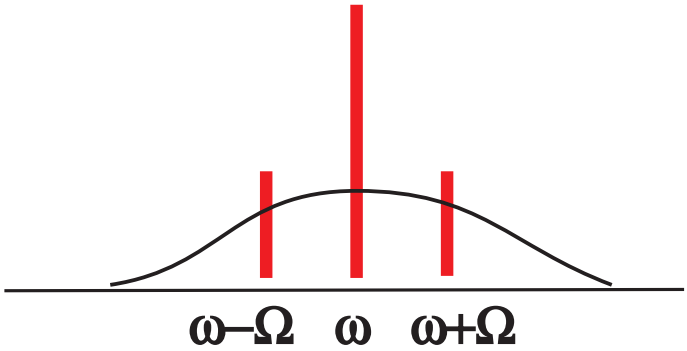

Figure 3.6: *Sketch in frequency space for the measurement of squeezed states with a coherent displacement: The envelope, given by the cavity resonance with width 17.5 MHz, describes the frequency range in which the quantum noise is altered due to the parametric interaction. The vertical center line (linewidth 10 kHz, thus negligible compared to the cavity or detection band width) represents the injected signal. Via homodyne detection the two side bands, well within the cavity linewidth, are measured simultaneously.*

wers below 5 mW no degradation of the efficiency was found. After more than one year of operation, the efficiency dropped by some percent (to as much as 80% for two diodes being exposed to light powers >10 mW over a prolonged period of time).[1]

Together with propagation losses of 2% , the detection efficiency can be estimated to be $\eta = 93\% \pm 3\%$. By measurements of the variance of the squeezed and anti-squeezed quadrature described in section 3.2.1 an overall detection efficiency of 80% including the escape efficiency can be inferred, which agrees within 3% with the value $\rho \cdot \eta = 82\%$ derived above.

3.1.6 Scheme for the generation of bright squeezed states

We confirmed experimentally, that the quantum noise of the OPA output measured by the homodyne system around the measurement frequency Ω is not changed by the injection of the 100 pW seed beam into the OPA. To realize a coherent excitation at the measurement frequency Ω, a part of the optical power of the seeding input has to be transferred to the sidebands at Ω. This is accomplished by a phase-modulator placed before the OPA cavity driven at frequency Ω with a modulation index $\beta \ll 1$ (electro-optic modulation of the nonlinear crystal is also possible). The amplitude of the sidebands βE_0 is determined by the strength of the cavity output field E_0 which depends on the relative phase ϕ between pump and signal wave and by the modulation index β. The carrier frequency ω is kept on-resonance with the cavity and the two "bright" sidebands $\omega \pm \Omega$ are well within the cavity bandwidth , $/2\pi = 17.5$ MHz (HWHM) (see Fig. 3.6).

[1] Apart from uncertainties regarding the absolute power calibration of the reference power meter, the thermopile, specified by ± 2%, a possible inaccuracy in these measurements which may lead to a lower detection efficiency in the actual measurements than the one expected by the individually measured efficiencies is the following: The diodes response is slower at the edge regions of the photodiode than in the center part. This may lead to a lower AC-response than the measured DC-efficiency if the beam's waist (80μm in our setup) is comparable to the detector's area (500μm) [276, 268].

In the semiclassical picture we may write the Fourier components at the frequency Ω' of the field's quadratures emitted from the output coupler as

$$\begin{aligned} X(\Omega') &= E_0\,\delta(\Omega') + \beta E_0(\delta(\Omega'-\Omega) - \delta(\Omega'+\Omega)) + X_n(\Omega'), \\ Y(\Omega') &= Y_n(\Omega'), \end{aligned} \tag{3.4}$$

where δ is the Dirac delta-function and X_n, Y_n are the broad-band quantum fluctuations. The electric field of the signal wave can now be written as

$$E_S(t) \sim \int X(\Omega')\cos(\omega+\Omega')t\,d\Omega' + \int Y(\Omega')\sin(\omega+\Omega')t\,d\Omega'. \tag{3.5}$$

Due to the very small ratio of HR transmission ($< 0.1\%$) to output coupler transmission (2.1%), the transmitted sidebands and their quantum fluctuations are strongly attenuated. The quantum fluctuations of the signal wave inside the resonator originate essentially from the vacuum fluctuations entering through the output coupler. The injected seed wave amplitude as well as the fluctuations are modified inside the resonator by the interaction with the 2ω pump wave: The quadrature fluctuations out-of-phase with the pump are deamplified (squeezed), the in-phase quadrature fluctuations are amplified. Similarly, the seed wave is deamplified if it is out of phase and amplified if it is in phase with the pump wave. Since the relative phase ϕ between seed wave and pump wave is controlled manually by a mirror attached to a piezoelectric actuator, deamplified amplitude-squeezed light, amplified phase-squeezed light and light squeezed in an arbitrary quadrature are easily generated. The coherent excitation of the sidebands is controlled coarsely by changing the power of the seed wave, fine control is achieved by varying the EOM modulation strength. By turning the modulation off, we obtain squeezed vacuum, by blocking the OPA pump wave, we are left with coherent states.[2]

3.1.7 Relation of the measured photo current to the quantum noise

At the beam splitter, the signal wave is mixed with the local oscillator wave $E_{LO}(t) \sim \cos(\omega t+\theta)$. The mixed waves at the two output ports of the beam splitter are given by

$$E_1 = \frac{1}{\sqrt{2}}(E_S + E_{LO}) \qquad \text{and} \qquad E_2 = \frac{1}{\sqrt{2}}(E_S - E_{LO}). \tag{3.6}$$

Discarding the second order noise terms, DC contributions as well as terms oscillating with twice the optical frequency ω, the difference current of the two photodetectors at

[2]Note, that there are different interpretations of the notion "bright squeezed light". Many authors refer to it as light with coherent excitation in the carrier, with squeezed sidebands without coherent amplitude. This is sensible for experiments, where exactly such a light source is of use, for example the spectroscopy experiments described in [184]. Since the method of quantum state reconstruction renders possible detailed comparisons between quantum optical theory and experiment the notion "bright squeezed light" is employed in this thesis in the same way standard texbooks of theoretical quantum optics [266, 137, 218] use it for the description of single mode states.

the detection frequency Ω is given by

$$\begin{aligned} i_-(\Omega,\theta) &\sim |E_1|^2 - |E_2|^2 \\ &\sim E_{LO}\cdot E_S \\ &\sim |E_{LO}|\cos(\omega t+\theta)[\\ &\quad (\beta E_0 + X_n(\Omega))\cos(\omega t+\Omega t) + (-\beta E_0 + X_n(-\Omega))\cos(\omega t-\Omega t)] \\ &\quad + Y_n(\Omega)\sin(\omega t+\Omega t) + Y_n(-\Omega)\sin(\omega t-\Omega t)] \\ &\sim (\beta E_0 + X_n(\Omega))\cos(\Omega t-\theta) + (-\beta E_0 + X_n(-\Omega))\cos(-\Omega t+\theta) \\ &\quad + Y_n(\Omega)\sin(\Omega t-\theta) - Y_n(-\Omega)\sin(-\Omega t-\theta). \end{aligned} \tag{3.7}$$

The crucial step of this equation array is the third transformation, in which the mode pair at $\pm\Omega$ is selected and the condition $E_{LO} \gg E_0$ is used. The homodyne detector output current i_- is mixed with an electrical local oscillator $\sim \sin(\Omega t+\psi)$, phase-locked to the modulation source, and then low-pass filtered with 100 kHz bandwidth. The resulting current is

$$\begin{aligned} i_\Omega(\theta,t) &\sim [(X_n(\Omega,t)+X_n(-\Omega,t))\cos\theta - (Y_n(\Omega,t)+Y_n(-\Omega,t))\sin\theta]\ \sin\psi \\ &\quad + [(2\beta E_0 + X_n(\Omega,t) - X_n(-\Omega,t))\sin\theta + (Y_n(\Omega,t)-Y_n(-\Omega,t))\cos\theta]\ \cos\psi\,, \end{aligned} \tag{3.8}$$

where $X_n(\Omega,t), Y_n(\Omega,t)$ are the quantum fluctuations in a 100 kHz wide band centered at Ω, transferred to DC. The time dependence of the fluctuations is due to the finite (non-delta) detection bandwidth. Setting the phase of the electric local oscillator such that $\cos\psi = 1$ and varying the local oscillator phase θ linearly in time, the mean homodyne current $\langle i_\Omega(\theta,t)\rangle \propto 2\beta E_0\cos\theta$ oscillates harmonically and exhibits in addition the phase dependent fluctuations with the chosen bandwidth of 100 kHz.

3.2 Quantum state measurements

While the local oscillator phase was swept by 2π in approximately 200 ms, the i_Ω-data were recorded using an A/D board T3012 of the company IMTEC, Backnang, with an amplitude recording resolution of 12 bit. The maximum number of recorded samples is 524 288, the board's frequency range is 0-30 MHz.[3]

The first step of the state measurement consists in determining the standard deviation ΔE_{vac} of the electric field of the vacuum state, to use it for the calibration of the noise of all generated states. Its value is obtained by a measurement of the noise current i_Ω with the homodyne detector signal input blocked. It serves as the unit of measurement for the

[3] During the time of this thesis the data caption was improved in three steps: The first sets were taken by an HP digitizing oscilloscope 54504A. Due to the memory limitation of 2000 sampled points, several recorded traces had to be overlayed, to gain sufficient statistical information. This led to an artificial phase diffusion effect of the reconstructed states. As a second instrument a Nicolet 400 oscilloscope with a memory depth of 256 000 points was employed. Here the effect of unequal sampling of the 256 amplitude channels (8 bit resolution) was the most disturbing effect. This effect can be partially compensated, by recording the response probability of all 256 channels and calibrating the measured noise traces accordingly. The measurements in [28] were done this way (see also the Konstanz T-Shirt of A.G. White).

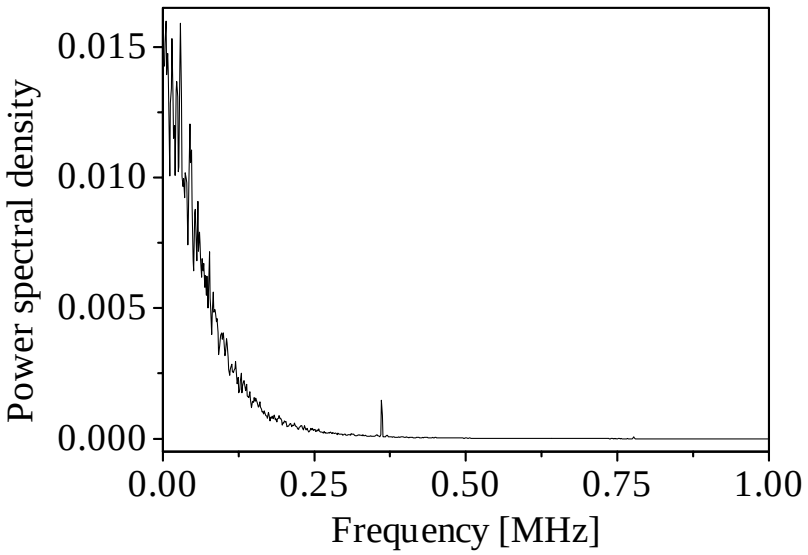

Figure 3.7: *Spectrum of one of the recorded noise traces, showing the bandwidth of 100 kHz within which the modes of the light field are detected.*

electric field E_0 of the signal wave (or more precisely of its sidebands $e_0 = 2\beta E_0$ at Ω). In order to verify that the system is not influenced by artefacts of electronic noise, it is necessary to check the data's frequency spectrum by taking the Fourier transform of the recorded homodyne noise. A typical measurement is shown in Fig. 3.7.

To test the measurement system, we verified the independence of the variance of the coherent state's electric field from the degree of coherent excitation. The traces shown in Fig. 3.8 demonstrate that the angle-independent variance is equal to $(\Delta E_{vac})^2$ for all three traces. The methods employed in our experiment enable us to detect coherent states of almost arbitrary field strength as long as the power of the signal beam is small in comparison with the local oscillator power. Accurate reconstructions are however limited to states with average photon numbers up to 40 ($e_0 < 9$), since the resolution of the A/D board is limited.

Immediately after the data are stored in the on-board memory of the A/D converter, the probability distributions are sampled. For this, the traces are subdivided into 128 equal length intervals within which the local oscillator phase is approximately constant. These individual time traces may be regarded as the quantum trajectories of a particular quadrature x_θ. Histograms of 256 amplitude bins for each quantum trajectory are formed, whose absolute bin width is normalized using as reference the distribution of a vacuum state. Note that the bin resolution of these probability distributions $P_\theta(x_\theta)$ (8 bit) is smaller than the one gained from the noise traces. Averaging over several amplitude bins serves to avoid errors due to uneven sampling of the A/D-board's channels. Fig. 3.9 shows selected measured quadrature probability distributions for one of the coherent states of Fig. 3.8. In the actual experiment these distributions are formed on-line, thus in time intervals of ≈ 8 s one can watch the wave packet moving back and forth in a 4π-oscillation of the light field. This motion of the wave packet in a harmonic potential was historically the first example of quantum dynamics, studied by Schrödinger in 1926 [222]. The on-line monitoring allows a constant check for electrical or optical disturbances and makes it possible to change experimental parameters directly to precisely control the state of the light field to be measured.

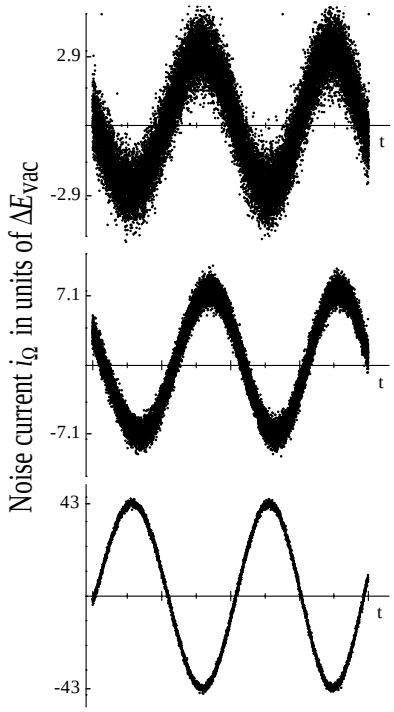

Figure 3.8: *Noise traces i_Ω for three coherent states with different amplitudes e_0. Average photon numbers $\langle n \rangle = e_0^2/2$ from top to bottom are equal to 4.2, 25.2, 924.5.*

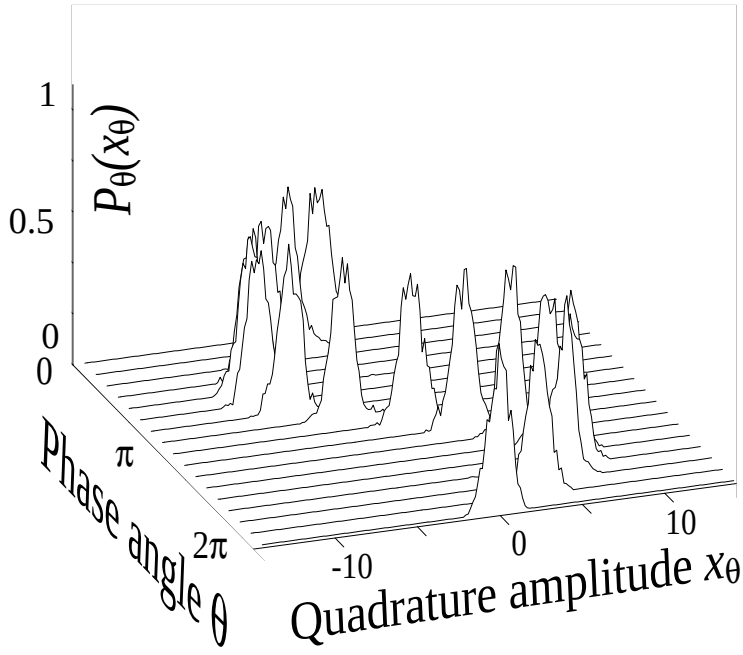

Figure 3.9: *Quadrature probability distributions for a coherent state, showing the harmonic motion of its wave packet.*

Figure 3.10: *Noise traces $i_\Omega(t)$ (left) and quadrature distributions $P_\theta(x_\theta)$ (right) of generated quantum states. From the top: Vacuum state, squeezed vacuum state. phase-squeezed state, state squeezed in the $\phi = 48°$-quadrature, amplitude-squeezed state. The noise traces as a function of time show the electric fields oscillation in a 4π-interval for the upper four states, whereas for the squeezed vacuum (belonging to a different set of measurements) a 3π-interval is shown. The quadrature distributions can be interpreted as the time evolution of wave packets (position probability densities) during one oscillation period. Oscillatory motion as well as "breathing" of the wave packet can be observed.*

The left column of Fig. 3.10 shows the whole set of recorded noise traces of different squeezed states generated by the OPA as well as the reference trace of the vacuum. They can be considered to be the experimental counterpart of the theoretical depictions of squeezed states introduced by Takahasi [240] and Caves [41]. The right column of Fig. 3.10 presents selected sampled corresponding quadrature probability distributions for the generated states. All distributions are found to be Gaussians. This is expected, since the states are generated from a coherent state with a Gaussian Wigner function via a second-order nonlinear interaction. Note that due to the fact that the generated squeezed states are mixed states (see Sec. 3.4.4) the description of the states by wave functions is not valid anymore. Nevertheless the behavior of the quadrature probability distributions is in principle the same as the one of the wave packet of a corresponding pure squeezed state. This can be seen when comparing the analytical formula for the distributions for the bright squeezed states

$$P_\theta(x) = \frac{1}{\sqrt{\pi} w_\theta} \exp\left[-\left(\frac{x - e_0 \cos(\theta - \phi)}{w_\theta} \right)^2 \right] \tag{3.9}$$

with the expression for the wave packet given in Sec. 2.2.1. As before e_0 denotes the amplitude and $w_\theta = \sqrt{a^2 \cos^2\theta + b^2 \sin^2\theta}$, with $a^2 = \mathrm{Var}(X_{sq}(\Omega))$ and $b^2 = \mathrm{Var}(X_{as}(\Omega))$ being the degree of squeezing and anti-squeezing and ϕ the squeezing angle

3.2.1 Squeezing measurements

Experimentally the amount of squeezing and anti-squeezing is obtained by determining the minimum and maximum variances of the measured quadrature distributions. A minimum of -6 dB ± 0.25 dB (= 0.25 linear scale) for the squeezed vacuum mode was detected, which is among the highest values of noise suppression of a quadrature of the light field achieved so far [184, 112, 30, 221]. For the bright squeezed light a minimum value of -5.2 dB (= 0.3) was obtained, due to phase instabilities of the seed wave and maybe noise introduced by the frequency modulation in the presence of the pump wave. The anti-squeezing amounted to 12-14 dB (= 15.8-26.9) for the states presented here. As shown in Fig. 3.11, these values agree well with the results of simultaneous measurements of i_Ω with a spectrum analyzer.

For the measurement shown, the pump power was approximately 3/4 the threshold power. (A little less for the bright squeezed states to avoid strong fluctuations of the mean amplitude e_0). Increasing the pump power further led to a higher gain, but additional noise degraded the squeezing. We believe this is mainly due to classical noise of the pump wave which is not completely removed by the filtering cavity. This is indicated by the presence of modulation signals of the frequency doubler in the OPA output spectrum. In this regime the measured values deviate from Eq. 2.53 (see also Ref. [275]).

From measurements at lower pump powers a total efficiency of detection of

$$\xi \cdot \eta = \frac{(b^2 - 1)(1 - a^2)}{b^2 + a^2 - 2} = 80\% \tag{3.10}$$

can be inferred, which agrees within 3% with the measured individual detection efficiencies. Correcting for η, the inferred squeezing amounted to 7.6 dB outside the resonator.

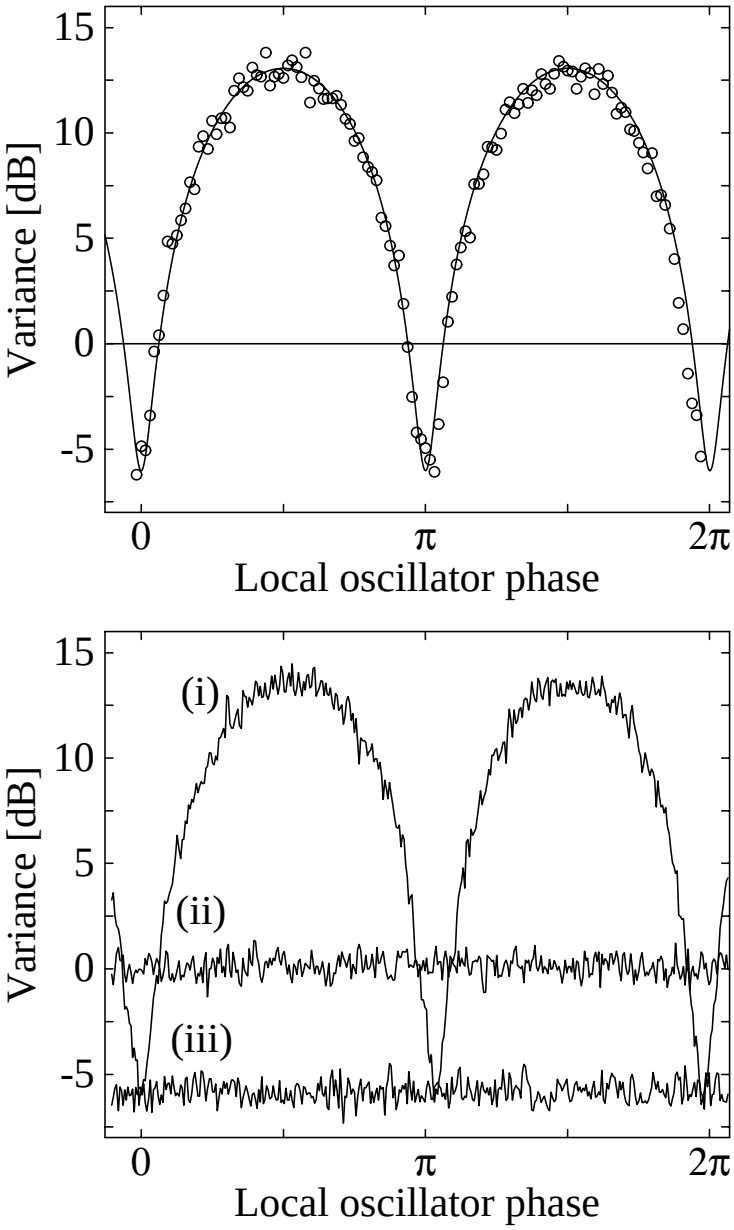

Figure 3.11: *Squeezed vacuum measurements. Upper picture: Variances of the measured quadrature distributions for 128 local oscillator phases (dots) in comparison with theory (line). Lower picture: Spectrum analyzer plot of the electric field variances. Trace (i): $Var(X_\theta)$ vs. the phase of the local oscillator θ. Trace (iii): $Var(X_\theta)$ with the phase $\theta = 0$ fixed manually for minimum noise, resulting in an averaged variance $Var(X_{sq}) = 6\ dB \pm 0.25\ dB$ below the vacuum level. The shot noise level is given by the average of trace (ii). The resolution bandwidth was 100 kHz, the video bandwidth 1 kHz.*

3.2.2 Higher order squeezing

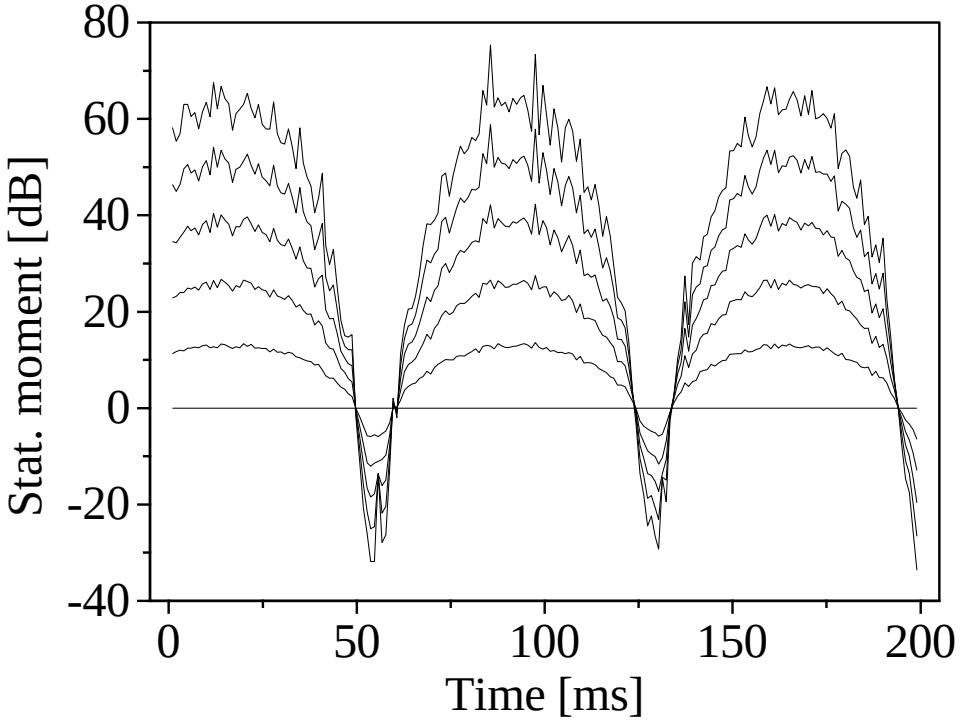

Figure 3.12: *Measured phase dependence of the 2nd (smallest), 4th, 6th, 8th and 10th (largest phase dependence) order statistical moment of a 6 dB squeezed-vacuum state. The local oscillator phase varies by $\approx 3\pi$. The odd statistical moments of the quadrature distributions are equal to 0.*

Not only the variance, the second order statistical moment can take values below that of the vacuum field, but also the higher even order statistical moments, as Hong and Mandel [95] predicted in 1985. Having sampled the complete distributions $\{P_\theta\}$, this higher-order squeezing of a quantum field is readily verified in our experiment up to the tenth's statistical moment. Fig. 3.12 shows a 3π-interval of the measured higher order moments of a 6 dB squeezed-vacuum state. Clearly, the higher the moment, the stronger is the phase dependence. This suggests that, by measuring the higher order moments, a more sensitive squeezing detection, i.e. detecting fields with a very weakly squeezed quadrature, should be possible.

This did not turn out to be true: At squeezing degrees of 0.1-0.3 dB both the spectrum analyzer signal as well as the 10th order moment phase dependence was lost in noise. Nevertheless, this method can be quite useful when trying to detect states of the light field that do not show a strong phase dependence in the variance, but in higher order moments, such as the star state presented in section 3.11. Here, a measurement of the 3rd order moment could give the first experimental proof of existence.

3.3 Reconstruction of the Wigner function

The Wigner functions of the measured states are obtained via the Inverse Radon Transform, the direct inversion of equation 2.42:

$$W(x,y) = \frac{1}{4\pi^2} \int_{-\infty}^{\infty} \mathrm{d}x' \int_{-\infty}^{\infty} \mathrm{d}r|r| \int_{0}^{\pi} \mathrm{d}\theta\, P_\theta(x')\, \exp[\mathrm{i}r(x' - x\cos\theta - y\sin\theta)] \tag{3.11}$$

A derivation can be found in [102] or [166]. It is important to note that, due to non-unity detection efficiency η, the equation above does not exactly yield the Wigner function but the s-parametrised phase space distribution function $W(x,y,s)$[38], the convolution of the original Wigner function with a Gaussian of width s. The parameter s is given by $s = 1 - 1/\eta = -0.064$ [134]. $W(x,y,-1)$ represents the Q-function, $W(x,y,0)$ Wigner's original distribution. Data taken with efficiencies $\eta < 0.5$ cannot be used for quantum state reconstruction, since they do not correspond to a meaningful phase space distribution [52].

A second issue to be aware of is that the numerical implementation of the inverse Radon transform contains a filtering process which reduces the faithfulness of the reconstruction.

To analyze the process of data filtering Eq. 3.11 can be rewritten as

$$W(x,y) = \frac{1}{4\pi^2} \int_{0}^{\pi} \mathrm{d}\theta \int_{-\infty}^{\infty} \mathrm{d}x'\, P_\theta(x')\, g(x' - \xi)\,, \tag{3.12}$$

where $\xi = x\cos\theta - y\sin\theta$ and

$$g(x) = \int_{-\infty}^{\infty} \mathrm{d}r|r| \exp(\mathrm{i}rx). \tag{3.13}$$

The process of filtering occurs in the evaluation of the angle and data independent function $g(x)$. The integral has to be approximated, since the data are given in discrete steps in x. Usually this is done by introducing a cut-off frequency r_{min}, r_{max} for the integration over r, chosen with respect to the spatial x-extension of the smallest features the measured distributions contain. To be able to determine the influence of data filtering quantitatively, we approximated $g(x)$ by means of quadratic regularization as presented in [102]:

$$g_\epsilon(x) = \int_{-\infty}^{\infty} \mathrm{d}r|r| \exp[-\epsilon r^2 + \mathrm{i}rx]. \tag{3.14}$$

As ϵ goes to zero the function reduces more or less to a δ-peak at zero. Numerically $g_\epsilon(x)$ is evaluated using the Dawson integral [185]. Figure 3.14 shows examples of $g(x)$ approximated by the two different methods.

In the reconstruction algorithm, filtering with a factor ϵ is equivalent to a convolution of the Wigner function with a Gaussian of width $\sqrt{2\epsilon}$. Thus detection losses and filtering

Figure 3.13: *Reconstructed Wigner functions for the states of Fig. 3.10. From the top: Vacuum state, squeezed vacuum state, phase-squeezed state, state squeezed in the $\phi = 48°$-quadrature, amplitude-squeezed state. The ripples at the base of all reconstructions are due to the finite number of angular divisions of the noise trace.*

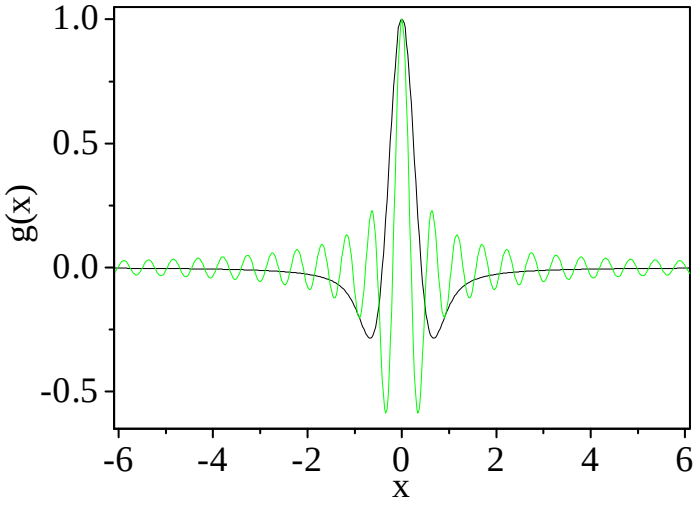

Figure 3.14: *Filter function $g(x)$ for the Inverse Radon Transform. The grey oscillating curve shows an approximation via cut-off frequency, the black one an approximation via quadratic regularization (the method employed in this thesis).*

are directly comparable and can be quantitatively described by the s-parameter of the reconstructed quasi-probability distribution. For the experimentally given discrete x-steps of $\approx 30/256$ (in units of the variance of the vacuum fluctuations), ϵ values of 0.002 to 0.01 gave satisfying results. Applying the distributive law for convolutions $(f * g_\sigma) * g_\kappa = f * g_{\sqrt{\sigma^2+\kappa^2}}$, where g_σ and g_κ are Gaussians of width $\sigma = \sqrt{(1-1/\eta)/2}$ and $\kappa = \sqrt{2\epsilon}$, yields for $\epsilon = 0.002$ a total value of $s = 0.072$. Thus, distortions due to the filtering process are small in our experiment and our reconstructed distributions are in fact very close to the states' Wigner function.

The results of the numerical inversion are presented in Fig. 3.13. The shown Wigner functions are in good agreement with the theoretical expression for bright, non-minimum-uncertainty squeezed states, given in Sec. 2.2.1. Note that for the theoretical calculations a coordinate system was used in which the state is squeezed along the x-axis and anti-squeezed along the y-axis combined with a displacement in an arbitrary direction in phase space. In contrast to this in the experiment the squeezing angle is changed by a constant angle of displacement. This corresponds to a coordinate rotation $x = x_0 \cos\phi + x_{\pi/2} \sin\phi$, $y = -x_0 \sin\phi + x_{\pi/2} \cos\phi$, when comparing Eq. 2.25 with Fig. 3.13. For the bright squeezed light it can be clearly seen how a change of the angle ϕ between pump and OPA-input signal corresponds to a rotation of the squeezed Wigner function in phase space.

3.4 Reconstruction of the density matrix

A different view of the generated states is provided by their density matrices ρ in the Fock basis. Here the state is described in terms of energy eigenstates, in contrast to the description by field components discussed in the previous paragraph. The density matrix is obtained from the measured distributions via integration over a set of pattern functions

$$\rho_{nm} = \int_0^{\pi} \mathrm{d}\theta \int_{-\infty}^{\infty} \mathrm{d}x_\theta \, P_\theta(x_\theta) \, \mathrm{e}^{i(n-m)\theta} \, f_{nm}(x_\theta) \, . \tag{3.15}$$

According to [199] the pattern functions are just the first derivatives of the product of *regular and irregular wave functions*

$$f_{nm}(x) = \frac{\partial}{\partial x} \Big[\psi_n(x) \, \varphi_m(x) \Big] \, . \tag{3.16}$$

Both wave functions represent energy eigenstates of the harmonic oscillator. The irregular wave function $\varphi_m(x)$ is the non-normalizable solution to the same energy eigenvalue as normalizable one $\psi_m(x)$ defined in Eq. 2.13. Using Eq. 3.16 a very efficient algorithm can be implemented for the computation of the pattern functions via the recursion relations of $\psi_m(x)$ and $\varphi_n(x)$. The exact procedure can be found in [135]. It was tested up to $n = m = 100$ to work well with both experimental and synthetic data. Fig. 3.15 shows two of the pattern functions demonstrating the structural similarity to the corresponding energy eigenfunctions.

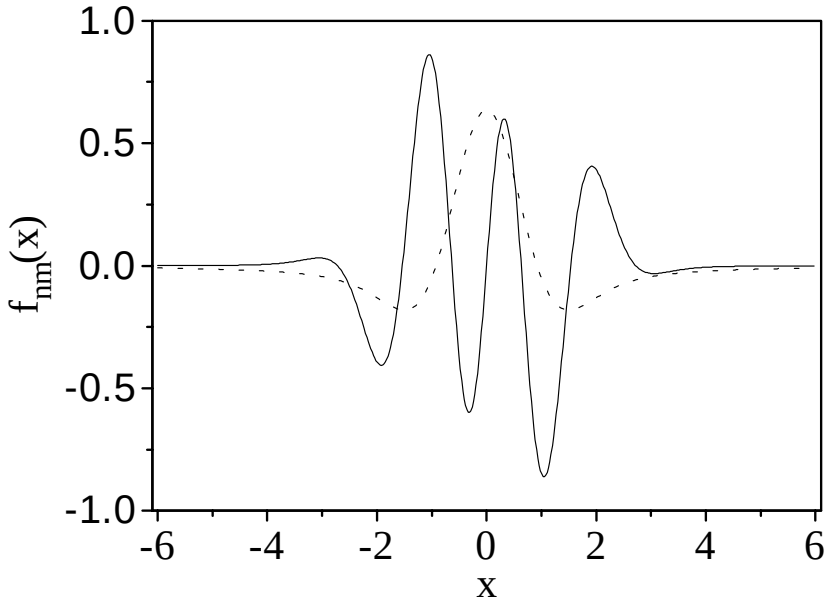

Figure 3.15: *Pattern functions f_{00} (dotted) and f_{14} (solid). The corresponding products of energy eigenstate wave functions $\psi_0(x)\psi_0(x)$ and $\psi_1(x)\psi_4(x)$ exhibit the same structure regarding the number of oscillations, minima, and maxima.*

3.4.1 Photon number distributions

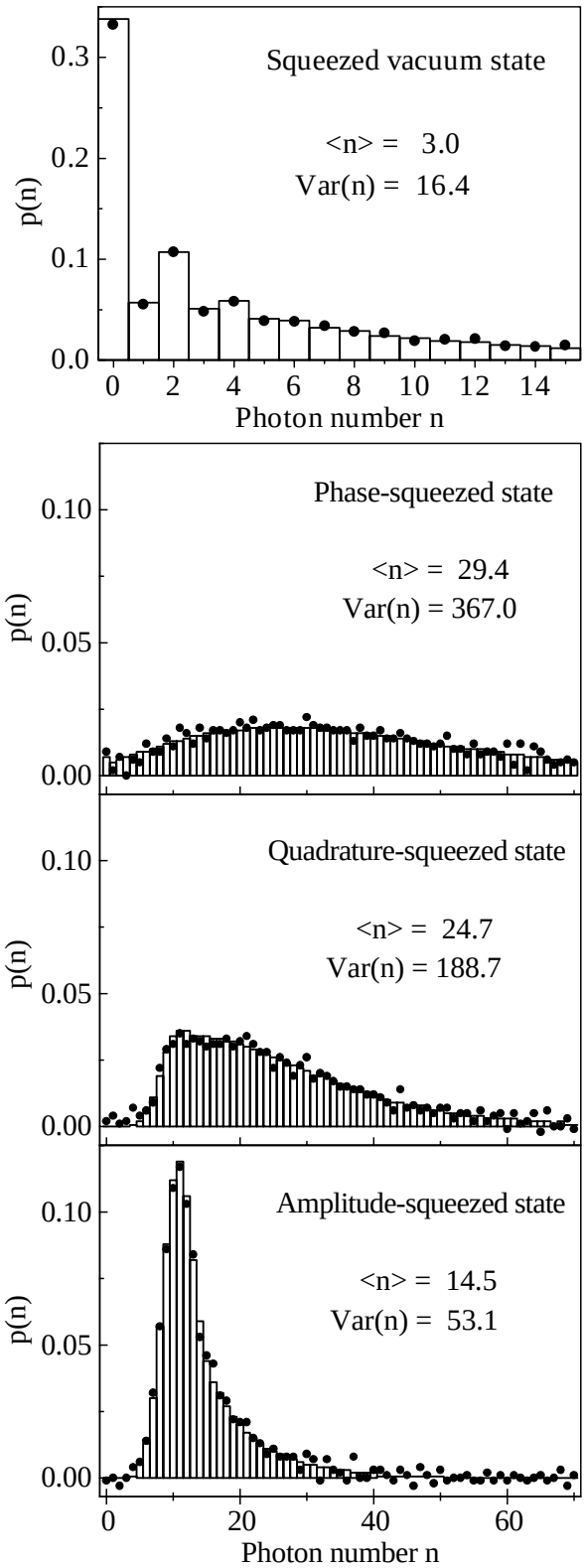

Figure 3.16: *Photon number distributions for the squeezed states of Fig. 3.10. Solid points refer to experimental data, histograms to theoretical expectations.*

The density matrix' diagonal elements $\rho_{nn} = p(n)$ are the occupation probabilities of the number states $|n\rangle$. Note that for the diagonal elements Eq. 3.15 becomes independent of the phase angle θ. Thus for photon number measurements it suffices to detect only the phase averaged state. This is important for experimental setups, where local oscillator and signal wave do not have a fixed phase relation to one another [163]. Historically, the characterization of optical quantum states was first pursued using photon counting and was applied to study the statistics of thermal and coherent light [4, 69] as well as sub- and super-Poissonian statistics [225, 242, 189]. In comparison with these earlier results the method of quantum state reconstruction offers the possibility to obtain very precise data of the photon statistics with near unity quantum detection efficiency, single photon resolution, for arbitrary low photon numbers. This enabled us to resolve distinctly quantum features of non-classical light that have been unobservable previously. Fig. 3.16 shows the photon number distributions for the squeezed states from Figs. 3.10, 3.13. (Since the vacuum state contains no photons, it is not depicted here). For the bright squeezed states one can see how a simple rotation of the squeezing ellipse with respect to the coherent excitation in phase space changes the photon distribution function substantially. The odd/even oscillations in the photon number distribution of the squeezed vacuum state are a consequence of the pair-wise generation of photons. They can be explained equivalently by quantum interference effects in phase space (see Sec. 3.4.5). Note that due to the coupling to the outer environment (losses) the odd photon numbers do not vanish completely.

All distributions shown are strongly super-Poissonian, $\mathrm{Var}(n) > \langle n \rangle$. For amplitude-squeezed light this seems counter-intuitive, since reduced amplitude noise should imply reduced intensity (photon number) noise. An explanation is given by the expressions for photon number average and variance for general (non minimum uncertainty) squeezed states[57]:

$$\begin{aligned} \langle n \rangle &= \tfrac{1}{4}(a^2 + b^2 - 2) + \tfrac{1}{2}{e_0}^2 \\ \mathrm{Var}(n) &= \tfrac{1}{8}(a^4 + b^4 - 2) + \tfrac{1}{2}{e_0}^2(a^2 \cos^2\phi + b^2 \sin^2\phi) \end{aligned} \tag{3.17}$$

For states with a large amplitude e_0, the variance of the amplitude quadrature $a^2 \cos^2 \phi + b^2 \sin^2 \phi$ indeed determines the characteristics of the photon number distribution. However, in the regime of low amplitudes, when coherent excitation and quantum noise are comparable in size, the first terms in Eq. 3.17, figuratively the photon content of the quadrature fluctuations, play a significant role. (For the relation between squeezing and sub-Poissonian photon statistics see also [149, 111, 289]).

We adjusted the experimental parameters to $a^2 = 0.43$, $b^2 = 3.3$ (reduced squeezing and anti-squeezing) and $e_0 = 4.12$ to obtain amplitude-squeezed sub-Poissonian light. Its Mandel-Q-parameter $\left(\mathrm{Var}(n) - \langle n \rangle\right) / \langle n \rangle = -0.45$ is to my knowledge the lowest value achieved so far using optical nonlinear frequency conversion techniques [54].

Fig. 3.17 shows the photon number distribution for the sub-Poissonian amplitude-squeezed state in comparison with those of a Poissonian coherent and a super-Poissonian phase-squeezed state with aproximately equal average photon numbers. Comparing with Fig. 3.16, obviously reconstructions of states with lower mean photon number are more precise, lead to better agreement with theory (see Sec. 3.4.3).

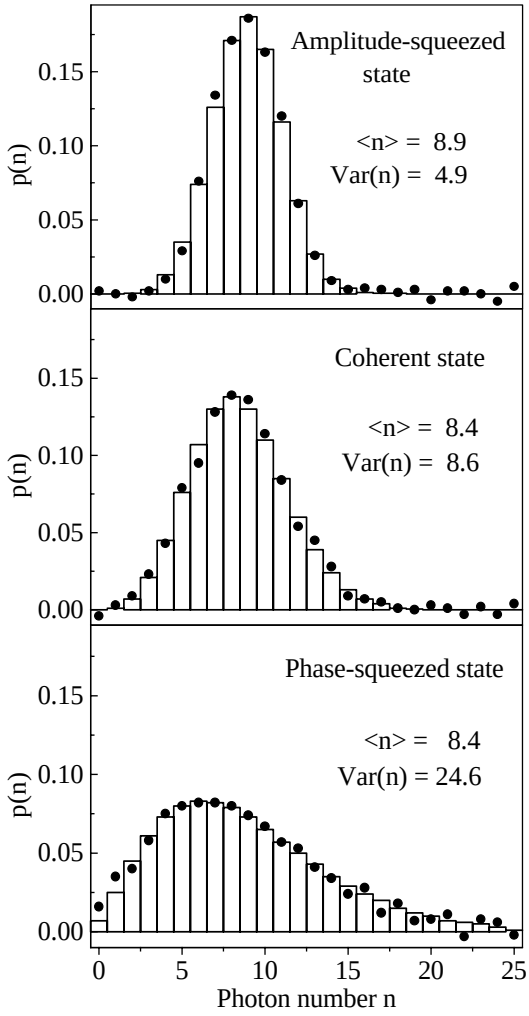

Figure 3.17: *Photon number distribution of an amplitude- and a phase-squeezed state in comparison with a coherent state of the same amplitude. Solid points refer to experimental data, histograms to theory. The amplitude-squeezed state shows a strong sub-Poissonian statistics. The deviation of photon number average and variance from their theoretical expectations is less than 2%.*

To relate the values found for the average occupation number $\langle n \rangle$ to the actually measured powers, we notice that $\langle n \rangle$ is the average photon flux per unit bandwidth. $p(n)$ is the probability that an ideal photon counter would register n photons per Hz bandwidth within 1 s. Given our detection bandwidth of 100 kHz set by the lowpass filter, a state with $\langle n \rangle$ photons implies a total photon flux of $\langle n \rangle \cdot 10^5$ photons/s $\approx 0.02 \cdot \langle n \rangle$ pW power distributed over the 100 kHz wide sidebands at $\pm\Omega$. For a coherent state this light power is concentrated in the coherent excitation e_0. For a bright squeezed state the flux in the sidebands arises partly from the monochromatic coherent excitation, and partly from the wide-band (and, on the scale of 100 kHz, white) noise power of the quantum fluctuations.

The total output power of the OPA consists of the transmitted seed wave power, $P_s \approx 100$ pW, plus the wide-band contribution of the quantum fluctuations. Integration over the squeezing spectrum of Eq. 2.53 results in a contribution $2\eta_{es}$, $\pi P_p/(P_{th} - P_p) = 6.5 \cdot 10^8$photons/s ≈ 100 pW if $P_p = 0.9 \cdot P_{th}$. Thus the total output power is ≈ 200 pW.

3.4.2 Density matrices

The density matrices up to n=25 for the three states of Fig. 3.17 are shown in Fig. 3.18. Due to the states' reflection symmetry in phase space, it is always possible to choose a basis in which their density matrices in the Fock representation are real. For the coherent state and the phase-squeezed state all elements ρ_{nm} are positive. For the amplitude-squeezed state an oscillatory pattern in the off-diagonal elements is observed (see below).

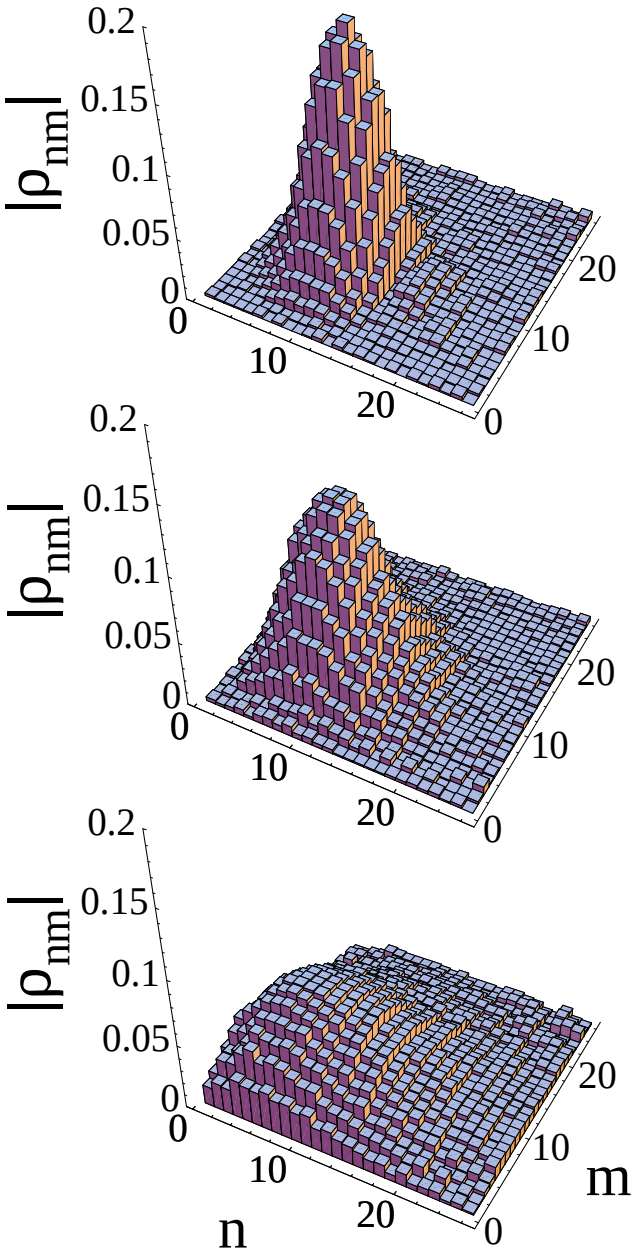

Figure 3.18: *Reconstructed density matrices (absolute values) of the three states of Fig. 3.17: (a) sub-Poissonian amplitude-squeezed state, (b) coherent state, (c) phase-squeezed state. The bump around $n \approx 18$, $m \approx 12$ for the amplitude-squeezed state is a characteristic feature explained in the text.*

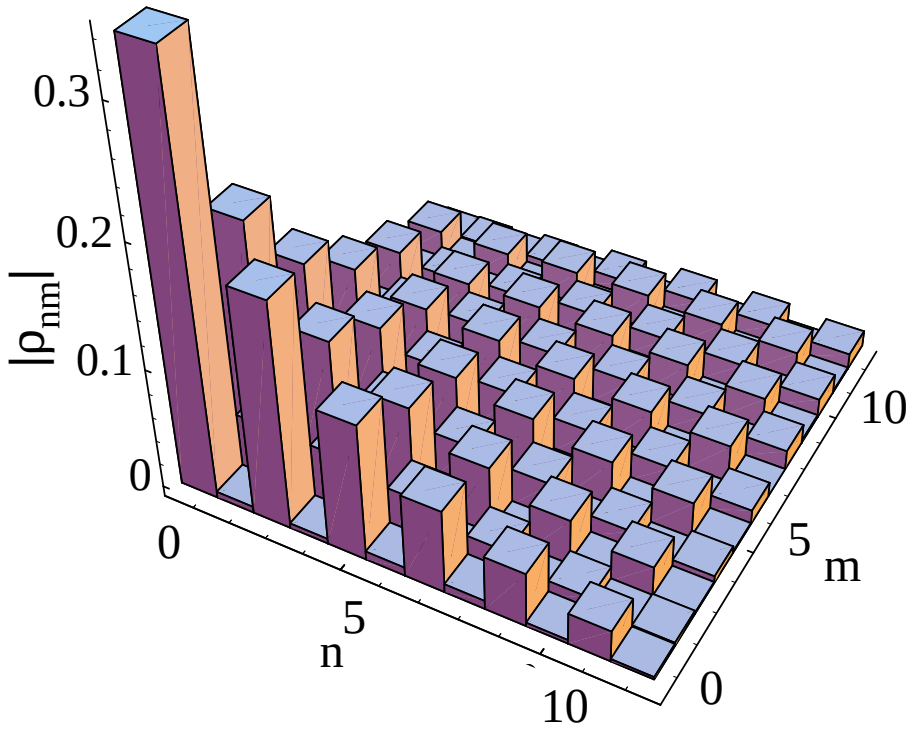

Figure 3.19: *Reconstructed density matrix of the squeezed vacuum state ($a^2 = 0.25$, $b^2 = 26.8$). Along the diagonal and the near off-diagonals the elements alternate in magnitude, which can be explained by quantum interference in phase space. Odd off-diagonals are zero within the error limit, due to the symmetry of the state's distribution in phase space, $W(x, y) = W(-x, -y)$*

The reconstructed density matrix of the squeezed vacuum is shown in Fig. 3.19. As has been mentioned for the photon number distribution, the odd/even oscillations in the diagonal and near off-diagonals are a striking evidence of the two-photon downconversion process. In more detail this is analyzed in the following section.

On a larger scale, the density matrix of a strongly amplitude-squeezed state exhibits a chessboard pattern similar to the one of a squeezed vacuum state. Equivalently the pattern can be explained by the state's symmetry in phase space and the Schleich-Wheeler oscillations in the photon number distribution. To some extend this can be seen in Fig. 3.20, showing a contour plot of the density matrix of the amplitude-squeezed state of Fig. 3.10. Since the detection efficiency was not high enough to observe the Schleich-Wheeler oscillations for bright squeezed states, the structure of the pattern seen in Fig. 3.20 is purely diagonal (symmetry) and not cross diagonal (interference effects).

This data analysis may be extended with the goal of taking into account the detection efficiency in our algorithms, thus trying to reconstruct the photon statistics of the signal *before* detection. In the photon counting picture the effect of losses in the detected photon number distribution can be understood figuratively very easy: If a photodetector with efficiency η detects the number state $|n\rangle$, the probability P_m to observe m photoelectrons is

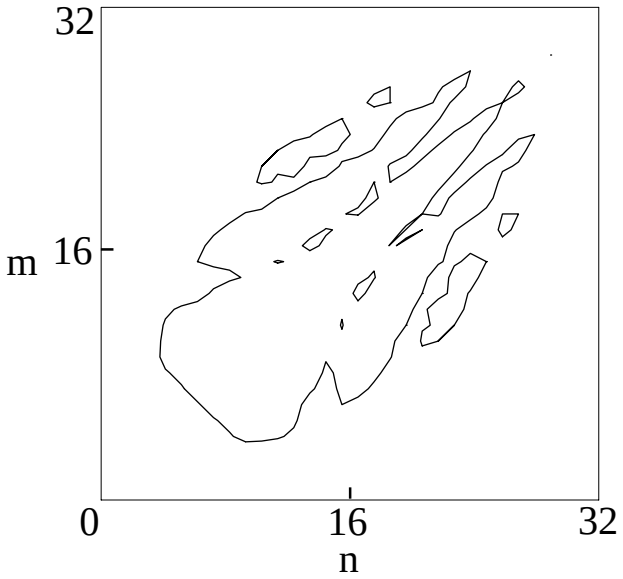

Figure 3.20: *Contour plot of the reconstructed density matrix of the amplitude-squeezed state of Fig. 3.10. The diagonal pattern due to the state's symmetry in phase space is clearly recognizable.*

given by the probability η^m to generate m photoelectrons times the probability $(1-\eta)^{n-m}$ not to observe the $n-m$ lost photons, times the combinational factor $\binom{n}{m}$, since the ordering of the photons is not known. Thus we arrive at a Bernoulli distribution [208]:

$$P_m^{(n)} = \binom{n}{m} \eta^m \, (1-\eta)^{(n-m)}. \tag{3.18}$$

This expression can also be derived via the theoretical model of coupling the undisturbed Hamiltonian to an external heat bath [159], here $\eta = \mathrm{e}^{-\gamma t}$, where γ is the coupling constant to the external reservoir (= decay time).

By applying the inverse Bernoulli transform to the reconstructed photon statistics the state's original photon number distribution can be obtained [117]. (Direct inclusion of detection efficiencies in the pattern functions of the reconstruction algorithm are based on the same ideas [52]). However, since this way to the detected photon number probability for n all probabilities for photon numbers $> n$ contribute, the reconstruction errors increase very rapidly even for small photon numbers n, thus no meaningful results were obtained this way. The analysis of the squeezed vacuum state and the amplitude-squeezed state with consideration of finite detection efficiency by more powerful reconstruction methods is described in section 3.5.1.

3.4.3 Comparison to theory

In general, all theoretical estimates were done numerically, using for comparison density matrices which were computed from calculated ideal marginal distributions. For the special case of the coherent and squeezed vacuum state the analytical expressions derived in Sec. 2.2.1 were used as well. Since the comparison theory-experiment is similar for all reconstructed states, it is shown here explicitly only for the squeezed vacuum state.

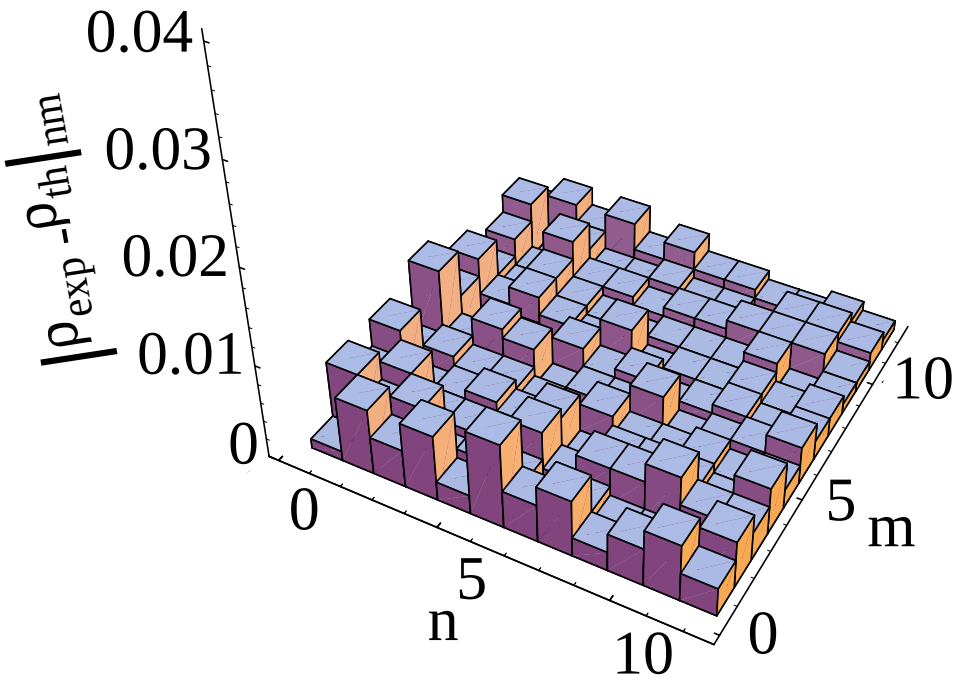

Figure 3.21: *Errors for the density matrix of the squeezed vacuum state.*

As pointed out in Sec. 2.2.1 the measured squeezed vacuum state is a mixed state. The issue of purity is adressed in Sec. 3.4.4. Considering the measured state as a squeezed thermal state with a degree of squeezing r and a number of thermal photons n_T we find for the experimental values $a^2 = 0.25$ and $b^2 = 26.8$

$$r = \frac{1}{2} \ln\left(\frac{a}{b}\right) = 1.17 \qquad \text{and} \qquad n_T = ab - 1 = 1.6. \tag{3.19}$$

Fig. 3.21 shows the discrepancy between the theoretical expectation of ρ given by Eq. 2.37 and the reconstructed matrix of Fig. 3.19. An estimate for the upper limit of the experimental reconstruction error of 0.01 is given by the largest density matrix element $\neq \rho_{00}$ of the vacuum state. Within this error limit the reconstructed density matrix of the squeezed vacuum state agrees with its theoretical estimation up to n=12. Usually up to n=60 the error is bounded by 0.02. These errors are still much larger than the purely statistical ones calculated in [135]. The main contributions to the overall error (in estimated order of importance) are:
(a) Phase fluctuations between signal and local oscillator wave (definition of the angle θ)
(b) offset drifts of the noise current
(c) amplitude and phase fluctuations of the pump wave
(d) electronic digitizing and amplification noise
(e) amplitude fluctuations of the local oscillator and imbalance of the homodyne system.

3.4.4 Purity of the measured quantum states

Another important feature of a quantum state that can be read off its density matrix is its purity: The trace of the square of the density matrix is a measure of the deviation

of the state from a pure one. For pure states $\mathrm{Tr}\rho^2 = 1$. This was verified in very good agreement with theory for the coherent state of Fig. 3.18. For the bright squeezed states we have

$$\mathrm{Tr}\rho^2 = \int\int \rho(x,x')^2 \mathrm{d}x\mathrm{d}x' = 2\pi \int\int W(x,y)^2 \mathrm{d}x\mathrm{d}y = \frac{1}{ab}. \tag{3.20}$$

Thus the larger the area ab of the ellipse of the Wigner function's contour, the more pronounced the mixed character of the quantum state. For the squeezed states of figure 3.18 $\mathrm{Tr}\rho^2$ amounted to 0.82-0.85 in agreement with the theoretical value given by $1/ab$. For the stronger squeezed states of figure 3.13 the agreement of $\mathrm{Tr}\rho^2 \approx 0.39$ with $1/ab \approx 0.45$ is reduced, since Fock states with high n contribute significantly to ρ, but could not be accurately reconstructed from the data. The effect of the cut-off due to the finite number $n_{\max}$ of reconstructed density matrix elements can be seen in the table below for the squeezed vacuum state with $a^2 = 0.25$, $b^2 = 26.8 \Rightarrow 1/ab = 0.39$:

	$\mathbf{n}_{\max}$	$\mathbf{Tr}\rho$	$\mathbf{Tr}\rho^2$	$\langle \mathbf{n} \rangle$	$\Delta^2\mathbf{n}$
exp	20	0.92	0.33	2.0	7.9
theo	20	0.92	0.33	2.0	7.9
exp	40	0.99	0.38	5.7	61.8
theo	40	0.99	0.39	5.6	59.8

The significant deviation from pure states arises mostly from loss experienced in the OPA-cavity and during propagation and detection. The fact that in general the value $\mathrm{Tr}\rho^2 = 1/ab$ is smaller for the generated squeezed states than the values expected for the given high overall detection efficiency, is due to the fact that the states' mixed character is also caused by additional noise of the pump beam. The higher value of the photon number variance in the experiment in comparison to theory is a general feature of all reconstructed states, due to artificial oscillations at high photon numbers. The trace of ρ is just the summation over the photon number probabilities and should amount to 1 in the ideal case.

3.4.5 Photon number oscillations and phase space interference

Oscillations in the photon-number distribution are by themselves not a signature of a nonclassical state, since classical states, generated via superpositions of coherent states, can also display such oscillations. Following an argument of Zhu and Caves [287], a criterion for a nonclassical photon number oscillation would be, that the distance of adjacent peaks at a photon number n are closer together than the local width $2\sqrt{n}$ of a Poisson distribution. This is undoubtedly the case for the odd/even oscillations observed here. The nonclassical character of these oscillations is elucidated by the concept of interference in phase space which was developed by Schleich and Wheeler in 1987 [214, 215, 216].

The basic idea can be understood easily by calculating the photon number probabilities via the Wigner distribution (see Eq. 2.34). For a squeezed thermal state with $W(x,y)$

given by Eq. 2.25 we have

$$p_n = 2\pi \int_{-\infty}^{\infty} \mathrm{d}x \int_{-\infty}^{\infty} \mathrm{d}y \; W(x,y)\, W_n(x,y)\,, \tag{3.21}$$

where

$$W_n(x,y) = \frac{(-1)^n}{\pi} \exp(-x^2 - y^2)\, L_n(2x^2 + 2p^2)\,, \tag{3.22}$$

is the Wigner function of the n-Fock state, L_n is the Laguerre polynomial. The shape of $W_n(x,y)$ is circular symmetric with oscillations of increasing amplitude from the center to its main characteristic, the outermost ring.

From a geometrical viewpoint, the integrand can be sketched as follows:

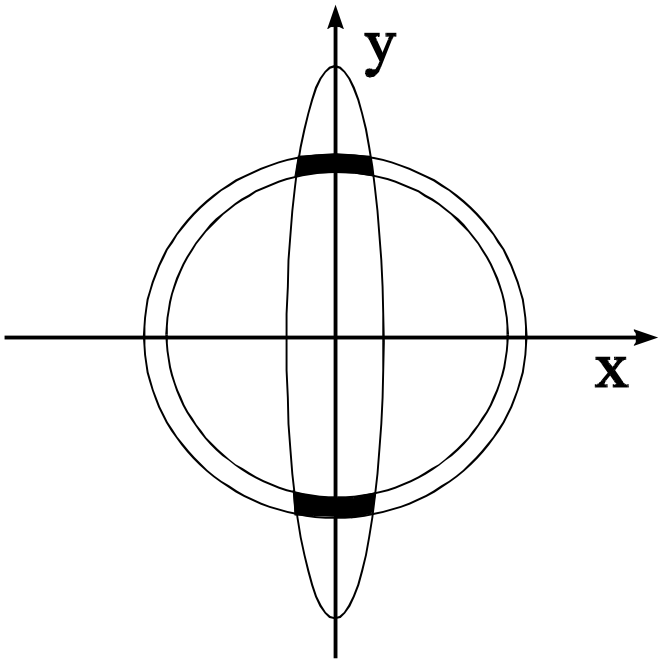

Figure 3.22: *Areas of overlap of the Wigner functions of a squeezed vacuum state and a Fock state.*

The main contribution to the integral stems from the two overlap regions of the elliptical area within the contour of the squeezed vacuum state with the outer ring of the Fock state Wigner function. The crucial point is the separation of these two regions, causing an interference analogous to the interference patterns occurring in the double slit experiment. It becomes visible in the oscillations of the photon number distribution.

It can be readily seen, that this idea cannot be extended straightforwardly to mixed states. If the area of the ellipse grows, the interference pattern would remain just the same according to the ideas outlined above. This cannot be correct, since for a purely classical state with $1 < a < b$ we don't expect to see any photon number oscillations. The solution to this paradox is, that quantum mechanical interference occurs only between pure states. To estimate the influence of the statistical mixture, we have to write the experimentally generated mixed squeezed vacuum state as a sum of pure states. This is done using the notion of the squeezed thermal state $S(r)\,\rho_T\,S^\dagger(r)$ described in section 2.2.1. The

squeezing operator acts on each Fock state $|n\rangle$ in the sum of Eq. 2.29. These squeezed number states have been analyzed in [210, 114, 168]. The Wigner function's contour of $S(r)\,|n\rangle$ has the form of an elliptically distorted ring, which results in four overlap regions in a plot analogous to Fig. 3.22 [114]. The interferences of these four regions are summed up for all n in Eq. 2.29, which washes out the photon number oscillations for states with a high number of thermal photons n_T. A detailed calculation of the oscillatory character of the density matrix elements of non-minimum-uncertainty squeezed vacuum states and its relation to phase space interference can be found in Ref. [133]. The good agreement of the experimental data presented here with asymptotical expressions derived from the concept of phase space interference is shown there as well.

3.4.6 Phase distributions of squeezed light

The definition of a quantum mechanical phase operator has been a subject of intense interest in the quantum optics community [145]. Several possible definitions exist, which are equally well usable from the point of view of quantum state reconstruction, as has been shown by a comparison of different phase operators by Beck et al. [11]. The Pegg-Barnett

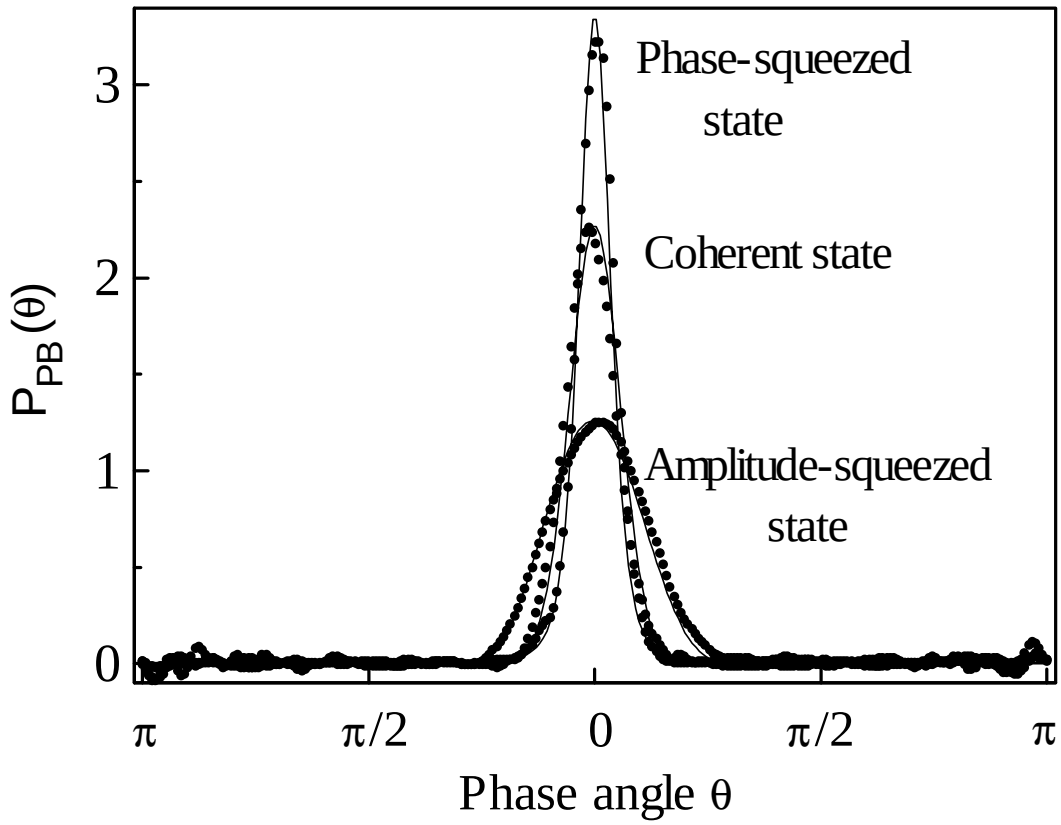

Figure 3.23: *Pegg-Barnett phase distribution for the states of Fig. 3.18 in comparison with a coherent state of the same amplitude. A pronounced narrowing of the phase distribution for the phase-squeezed state is found. Solid points refer to experimental data, lines to theoretical expectations.*

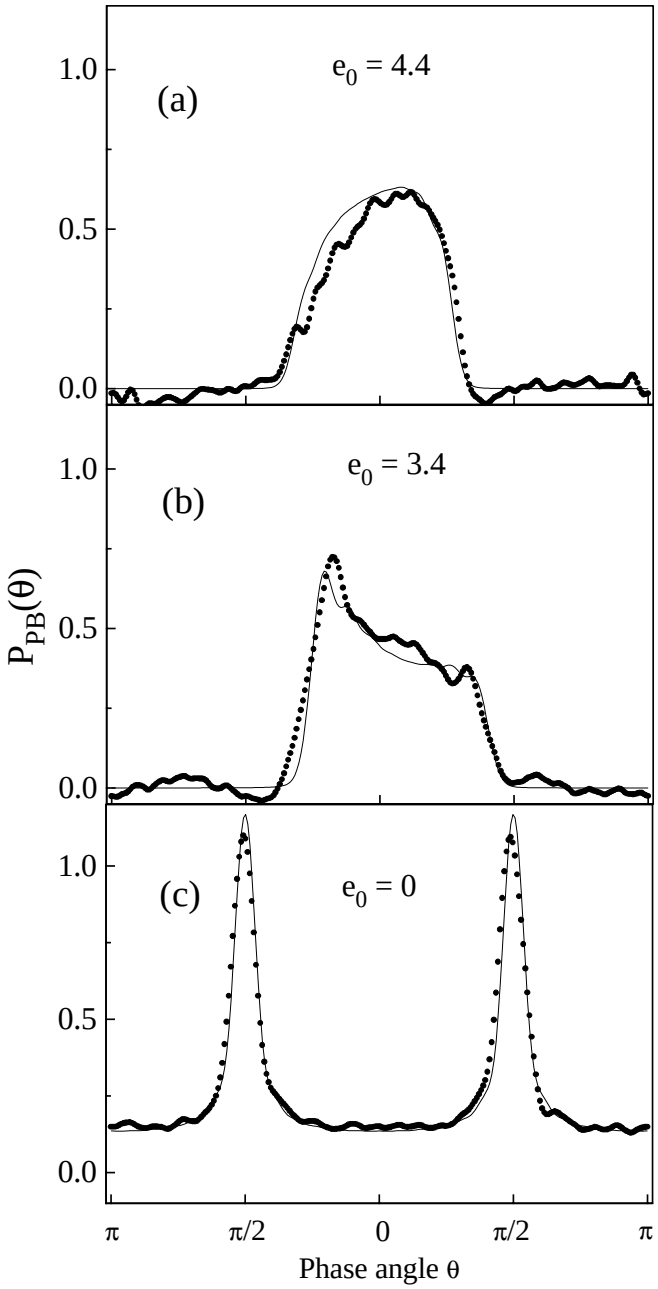

Figure 3.24: *A bifurcation of the phase distribution occurs when the amplitude-squeezed state is translated closer to the phase space origin. Shown here are the Pegg-Barnett phase distributions for two amplitude-squeezed states with amplitudes e_0 before (a) and after (b) the bifurcation point, where the two maxima of the phase distribution split, (c) the squeezed vacuum state of Fig. 3.19. Solid points refer to experimental data, lines to theory. The slight asymmetries are due to a variation of the squeezing angle ϕ.*

phase distribution [179], defined by

$$P_{PB}(\theta) = \frac{1}{2\pi} \sum_{n,m=0}^{s} \mathrm{e}^{\mathrm{i}(m-n)\theta} \rho_{nm} \tag{3.23}$$

on the $(s+1)$-dimensional subspace spanned by $\{|n\rangle\}_{n=0,..,s}$ is a convenient choice to analyze the measured states, since quantum state reconstruction techniques allow only the determination of a finite number of density matrix elements ρ_{nm}. For a direct reconstruction of the quantum mechanical phase distribution by a special integral transform, see section 3.5.2.

As the photon number distribution is the appropriate representation to verify intensity squeezing for amplitude-squeezed light, the phase distribution is intended to accomplish the same for the phase-squeezed states. Fig. 3.23 shows the phase distributions for the states of Fig. 3.18, demonstrating the phase squeezing and antisqueezing of these states in comparison with a coherent state of the same amplitude. The observed phase squeezing can be considered to be the quantum mechanical counterpart to the classical line narrowing due to parametric amplification mentioned in Sec. 2.4.

As the coherent excitation e_0 of the amplitude-squeezed state is reduced, a bifurcation of the phase distribution occurs (Fig. 3.24a,b). Finally the squeezed vacuum with $e_0 = 0$ displays a double-peaked phase distribution (Fig. 3.24c), due to the large ratio of the antisqueezed to the squeezed variance. This behavior was first pointed out by Schleich et al. [217] (see also [255, 165]). Figuratively one can think of this as follows: The closer a state of the light field is situated to the origin of the phase space, the more distinct features of it can be resolved by the phase operator.

3.4.7 The Special Number-Phase Wigner function

Another interesting complete state representation besides the Wigner function and the density matrix is given by the newly found special Number-Phase Wigner function by J. Vaccaro [256]:

$$S_{\mathrm{NP}}(n,\theta) \equiv \frac{1}{2\pi}\Big(\sum_{p=-n}^{n} \mathrm{e}^{i2p\theta} \,|n+p\rangle\langle n-p| + \sum_{p=-n}^{n-1} \mathrm{e}^{i(2p+1)\theta} \,|n+p\rangle\langle n-p-1|\Big). \qquad (3.24)$$

Instead of amplitude- and phase-quadrature, the state is represented in a space defined by the Pegg-Barnett phase and the energy eigenvalues (photon numbers). S_{NP} is easily gained from the data via the reconstructed density matrix elements. For the squeezed vacuum state the photon number oscillations and the splitting of its phase distribution can be clearly seen, thus the nonclassical character of the state becomes more apparent.

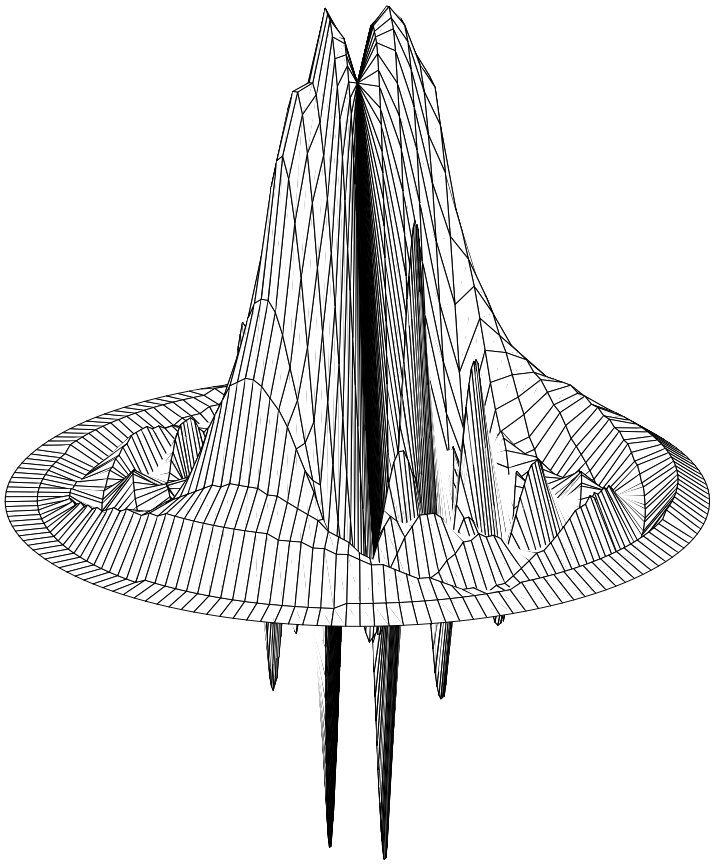

Figure 3.25: *Experimental special number phase Wigner function for a squeezed vacuum state. Each circle of the polar plot corresponds to a photon number n. The plot was generated using the data of the reconstructed density matrix of a 5.5 dB squeezed vacuum state. Distinct features are the photon number oscillations and the splitting of its phase distribution.*

3.5 Other reconstruction methods applied to the measured squeezed states

3.5.1 The inverse problem approach by Sze Tan Consideration of finite detection efficiency

Sze Tan adopted a different approach to homodyne tomography. Not an analytic inversion formula is employed but rather with the help of the Bayesian statistical formalism in the space of all possible density matrices the one most likely to belong to the measured data is found. This makes the method more powerful in so far, as it allows for taking into account finite detection efficiency, thus reconstructing the density matrix of the state of the light field before it has been disturbed by propagation and detection losses. Similar methods were already known in classical tomography, (see for example [100]). For related proposals of quantum state estimation see [172, 96, 9].

The best introduction is found in Tan's paper itself [241]. For the case of noiseless data Tan's method allows an easy and elegant derivation of the pattern functions defined in section 2.3.1. First we see from Eq. 2.41 that there exists a linear relation between the measured marginals and the density matrix. For reasons of simplicity, I consider only the diagonal elements of the density matrix $p_n = \rho_{nn}$ and the angle-averaged marginals $\bar{P}(x)$, the extension to the general case is straightforward. Given the state and its distribution $\mathbf{p} = \{\mathbf{p_n}\}$ we have

$$\bar{P}(\mathbf{x}) = \mathbf{A}\mathbf{p}\,, \tag{3.25}$$

with $\mathbf{A} = (a_{jn}) = |\langle x_j|n\rangle|^2$, where $\langle x_j|n\rangle$ are the energy eigenstates of the harmonic oscillator in the position basis. In the actual experiment we do not know the state, so we want to find a photon number distribution $\mathbf{p}$ that minimizes

$$\epsilon^2 = ||\bar{P}(\mathbf{x}) - \mathbf{A}\mathbf{p}||. \tag{3.26}$$

Setting $\partial\epsilon^2/\partial p_n = 0$ we get $(\mathbf{A}^t\mathbf{A})\mathbf{p} = \mathbf{A}^t\bar{P}(\mathbf{x})$, or

$$\mathbf{p} = (\mathbf{A}^t\mathbf{A})^{-1}\mathbf{A}^t\bar{P}(\mathbf{x}) \tag{3.27}$$

which is called Moore-Penrose solution. Plotting the x-dependent rows of the linear transform acting on the marginal vector $\bar{P}(\mathbf{x})$ gives exactly the previously analytically found pattern functions $f_{nn}(x)$. This formalism is easily modified to include detecion efficiency, replacing $\mathbf{A}$ by

$$\mathbf{A} = (a_{jn}) = \sum_{r=0}^{N-n-1} \binom{n+r}{r} \eta^n (1-\eta)^r \, |\langle x_j|n+r\rangle|^2. \tag{3.28}$$

For a more realistic treatment, Tan assumes a Gaussian noise on the data, described by a matrix $\mathbf{W}$ whose diagonal elements are given by the noise variances for each x_j. The maximum likelihood solution becomes then

$$\mathbf{p} = (\mathbf{A}^t\mathbf{W}\mathbf{A})^{-1}\mathbf{A}^t\mathbf{W}\bar{P}(\mathbf{x}) \tag{3.29}$$

Figure 3.26: *(a) Experimental phase-averaged homodyne amplitude histogram of the squeezed vacuum state of Fig. 3.10. (b) Maximum-likelihood reconstruction of the photon number distribution with no compensation for detection efficiency, (c) Maximum-likelihood reconstruction of the photon number distribution with compensation for detection efficiency.*

Fig. 3.26 shows the averaged marginals with the estimated errors, a first reconstruction assuming a detection efficiency $\eta = 1$ (giving the previous result of Fig. 3.16) and a second reconstruction assuming a detection efficiency $\eta = 0.85$. As can be seen, for the latter only the first six photon numbers yield plausible results. Exactly the same result is found by employing the analytically derived pattern functions with finite detection efficiency of D'Ariano et al. or by applying the inverse Bernoulli transform to the originally derived photon number distribution of Fig. 3.16. Obviously, reconstructions that take into account finite detection efficiencies need more sophisticated methods.

This is done by including prior information such as the non-negativity of the photon number probabilities. Thus in the space of all possible density matrices a certain subset is given the priority to be more likely to be measured before any data were recorded. Tan chooses a Tikhonov regularization, introducing as a prior probability function

$$Pr(\mathbf{p}) \propto \exp(-\frac{1}{2}\lambda^2 ||\mathbf{p} - \mathbf{p}_\infty||^2), \tag{3.30}$$

where $\mathbf{p}_\infty = \mathbf{0}$ is called the default reconstruction which is preferred in absence of any data, and λ the regularization parameter used to adjust the strength of the preference. Again the minimization problem is posed, and by carefully choosing the regularization parameter, realistic estimates of the quantum state can be gained.

Figure 3.27: *Reconstructions of the photon number distribution of the squeezed-vacuum state using the non-negative least-squares algorithm with Tikhonov regularization (a) $\lambda = 0.02$, (b) $\lambda = 0.11$. The error bars are calculated from 100 simulated data sets.*

Figure 3.28: *Reconstructions of the photon number distribution of the amplitude-squeezed state of Fig. 3.10 with Tikhonov regularization (a) $\lambda = 0.02$, (b) $\lambda = 0.11$. Shaded region: experimental values, dashed line: theoretical estimate, showing the expected but not detected Schleich-Wheeler oscillations.*

Fig. 3.27 shows the squeezed vacuum reconstructions for two choices of the regularization parameter. It can be seen that bigger λ tend to smoothen the data. Correcting for detection efficiency makes the oscillations become more pronounced but no additional oscillations for $n > 5$ can be detected.

The same is true for an evaluation of the data of the amplitude-squeezed state of section 3.2. For the assumed detection efficiency of 0.8 Schleich-Wheeler oscillations should clearly be visible. As can be seen in Fig. 3.28 the photon number distribution becomes realistic and close to theory for $\lambda > 0.05$, but no large period oscillations are detectable.

As conclusion, probabilistic methods are powerful and elegant tools for quantum state estimation, but applied to experimental data no additional quantum features besides the ones detected by standard reconstruction methods were revealed so far.

3.5.2 The number-phase uncertainty Direct reconstruction of the phase distribution

As mentioned earlier, employing different integral kernels in Eq. 3.15 allows to sample not only the density matrix but arbitrary field operators [53]. In collaboration with the group of Prof. Welsch in Jena we reconstructed the Susskind-Glogower phase distributions of the states presented in section 3.2 directly from their exponential moments [50] without detour via the density matrix (Sec. 3.4.6) or the Wigner function ([11, 230]).

The canonical phase distribution is defined as

$$P_{SG}(\varphi) = \frac{1}{(2\pi)} \langle \varphi \,|\, \hat{\rho} \,|\, \varphi \rangle, \tag{3.31}$$

where the phase states are given as [237, 145]

$$|\, \varphi \,\rangle = \sum_{n=0}^{\infty} e^{\mathrm{i}n\varphi} \,|\, n \,\rangle. \tag{3.32}$$

The exponential phase moments Ψ_k are defined by the Fourier components of the phase distribution $P_{SG}(\varphi)$, i.e., $\Psi_k = \int_{2\pi} d\varphi \, \mathrm{e}^{\mathrm{i}k\varphi} P(\varphi)$. Expressing the moments by means of the density matrix elements we find

$$\Psi_k = \sum_{n=0}^{\infty} \rho_{n+k,n}. \tag{3.33}$$

In Ref. [173] it is shown that Ψ_k can be obtained from the quadrature-component distributions $p(x, \vartheta)$ by the integral

$$\Psi_k = \int_0^{\pi} \mathrm{d}\vartheta \int_{-\infty}^{\infty} \mathrm{d}x \, K_k(x, \vartheta) \, p(x, \vartheta), \tag{3.34}$$

where $K_k(x, \vartheta)$ is a well-behaved integral kernel suited for direct sampling of Ψ_k from the homodyne output for any normalizable quantum state.

Knowing Ψ_k, the phase distribution $P(\varphi)$ can be obtained according to $P(\varphi) = (2\pi)^{-1} \sum_{k=-\infty}^{\infty} \mathrm{e}^{-\mathrm{i}k\varphi}\Psi_k$. However, the first moment already contains essential information about the phase properties. It can be used to introduce a mean phase $\bar{\varphi} = \arg \Psi_1$ and a phase uncertainty $\Delta\varphi = \arccos |\Psi_1|$, which implies a number–phase uncertainty relation [93, 171]

$$\Delta n \, \tan \Delta\varphi \geq \frac{1}{2}. \tag{3.35}$$

Note that for the number-uncertainty $\Delta n = (\langle \hat{n}^2 \rangle - \langle \hat{n} \rangle^2)^{1/2}$ the quantities $\langle \hat{n} \rangle$ and $\langle \hat{n}^2 \rangle$ can also be obtained by direct sampling according to a relation of the form (3.34), with the integral kernel being given in [53]. Hence, homodyne detection can be regarded as the most direct way that has been known so far for experimental verification of the number-phase uncertainty relation.

The following table shows the results of direct phase distribution reconstructions for some of the measured states.

state	A	B	C	D	E	F	G	H
$\bar{\varphi}$	0.02	1.59	3.13	3.13	-3.13	1.56	2.62	0.78
$\Delta\varphi$	0.17	0.14	0.30	0.54	0.17	0.14	1.56	0.31
$\bar{n}$	8.62	25.94	9.19	14.72	8.95	38.45	6.92	26.46
Δn	3.03	6.20	2.30	7.21	5.38	25.05	10.02	14.85
$\Delta n \, \tan\Delta\varphi$	0.52	0.87	0.71	4.32	0.92	3.53	$\sim$	4.75

Table 3.1: *Measured values of $\bar{\varphi}$, $\Delta\varphi$, $\bar{n} = \langle \hat{n} \rangle$, and Δn, and the resulting values of the number–phase uncertainty product $\Delta n \tan \Delta\varphi$ for various quantum states [(A,B) coherent states; (C,D) amplitude-squeezed states; (E,F), phase-squeezed states; (G) squeezed vacuum; (H) state squeezed in the 48°-quadrature].*

The last row of the table shows the resulting values of the number–phase uncertainty product $\Delta n \tan \Delta\varphi$, which are in full agreement with the predicted inequality. The coherent states (A,B) and phase-squeezed states (E,F) are seen to exhibit relatively small phase uncertainties. The smallest value of the uncertainty product is observed for the coherent state (A). It is close to the limit of 1/2. Relatively large phase uncertainties are observed for the amplitude-squeezed states (C,D) and the 48°-quadrature-squeezed state (H). As expected, the near-maximum phase uncertainty $\Delta\varphi \approx \pi/2$ is found for the squeezed vacuum (G), therefore its large uncertainty product $\Delta n \, \tan\Delta\varphi$ is not listed. For the evaluation of the complete phase distribution note that the Fourier transform of the exponential moments may lead to artificial oscillations, due to the finite number of accurately determined moments.

3.5.3 Probing of quantum phase space by photon counting

Banaszek and Wodkiewicz proposed a method of measuring the Wigner function via photon counting [7]. The idea is the following: The value for the Wigner function at the origin is given by the alternating sum of the states' photon number distribution: $W(0,0) = \frac{2}{\pi} \sum_{n=0}^{\infty} (-1)^n p_n$. By displacing the signal state to be measured in phase space via overlapping it with a coherent state within the range where the signal state shows

its distinct features, all values $W(x, y)$ are accessible by determination of the photon statistics of these overlap states.

In a restricted sense this method is applicable to our data: The state to measure is the squeezed vacuum, the displacing occurs when we inject a coherent state into our resonator, thus overlapping it without change of the quantum statistics with the squeezed vacuum state. These bright squeezed states are measured via quantum state reconstruction, thus the photon number distributions are accurately determined. Applying the Banaszek/Wodkiewicz-algorithm results in one point of the phase space distribution of the squeezed vacuum state for each measured bright squeezed state. To be able to apply the method, states with reasonably low mean photon numbers, and accurate distributions, had to be chosen and it had to be assured that the degree of squeezing for all states was precisely the same. Considering these restrictions only the sub-Poissonian amplitude-squeezed, the corresponding phase-squeezed state and the squeezed vacuum itself were appropriate. The amplitude-squeezed state shifted the Wigner function far away from the origin, so the result was 0 within the error bound. For the squeezed vacuum (1) and the phase-squeezed state (2) I got as values for the Photon Count Generating Function (PCGF), a function proportional to the Wigner function, (for its exact definition see [8]):

Theory PCGF(x,y)	reconst. PCGF(x,y)	point (x,y)
0.17	0.19	(0, 0)
0.0016	0.0020	(4.1, 0)

Thus two points of the squeezed vacuum Wigner function were determined. Obviously, this reconstruction technique is not the method of choice in our case, but the measurement demonstrates that in principle it can be applied to optical experiments. (Note that a similar method was employed in the trapped ion experiment in Boulder [132]).

3.6 The OPO at and above threshold

The (incomplete) measurements presented in this chapter were among my first motives to improve the quantum state reconstruction techniques, since here a field in quantum optics is entered, which is difficult to access for both theoreticians and experimentalists alike. Thus complete experimental quantum state descriptions might be of high value to improve our understanding of the dynamics of the OPO.

The behavior of the degenerate OPO at threshold is roughly sketched as follows: In a classical description the phase with which the OPO starts oscillating is determined by the pump wave 2ω only up to a phaseshift of π. Thus directly at threshold the OPO's subharmonic wave has to decide with which of the two possible phases it will start to oscillate. Fig. 3.29 shows that this behavior can indeed be observed in the laboratory.

The quantum mechanical description of the behavior leads to similar results. Starting with the elliptical Wigner function of the OPO below threshold, with rising pump power the state is squeezed further, until a double-peaked phase space distribution arises, a superposition of two states with nonvanishing mean field amplitude and a phase separation of π. The higher the pump power, the further apart both distributions are. This

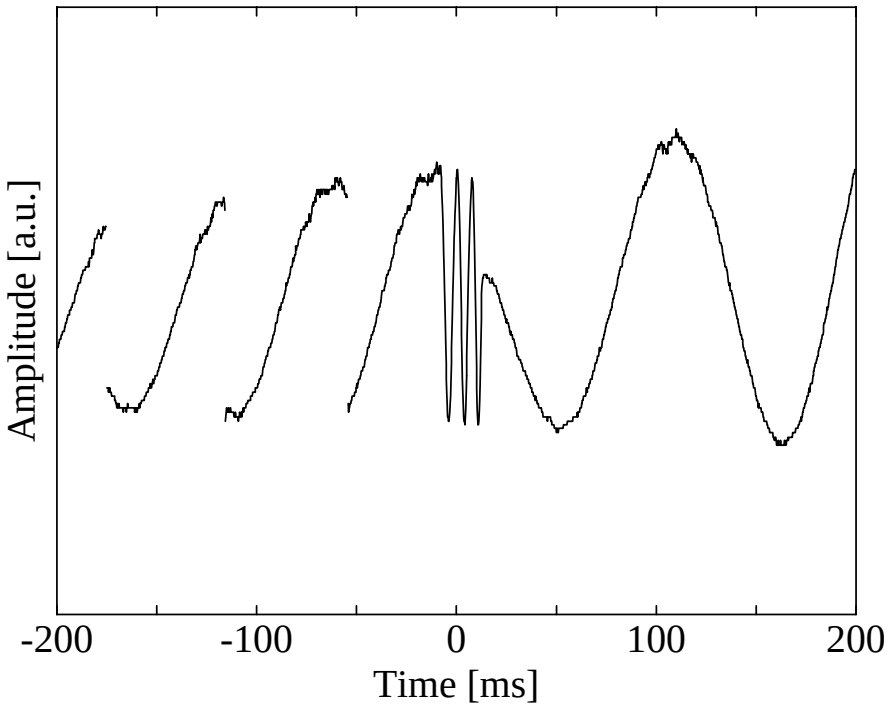

Figure 3.29: *Interference between the mean electric field amplitude of the degenerate OPO at threshold and a reference laser wave. Phase jumps of π are observable right after the start of the oscillation. Due to a change in temperature the amplitude of the OPO output rises continuously. For high amplitudes the phase remains constant. The rapid oscillation in the middle of the plot is due to the flyback of the piezo scanning the light wave's relative phase.*

state evolution has been treated in numerous theoretical papers, not all being in perfect agreement with each other (see for example [274, 116, 124, 257, 260]). Fig. 3.30 depicts the mean field amplitude (= maximum of the phase space distribution) as a function of the pump field strength (notation of Sec. 2.4).

For an ideal lossless OPO interference fringes between the two phase-separated distributions would appear, but, as pointed out by Timo Felbinger, already the loss of one photon causes this interference pattern to vanish [66]. What remains is a classical superposition of two (approximately) coherent states (for the process of decoherence see also [291, 33, 73]).

Is at least such a classical superposition experimentally observable? Fig. 3.31 shows some of the measured results. To be able to detect nonvanishing mean field amplitudes at the measurement frequency, the OPO-crystal itself was electrooptically modulated while the pump power was slowly varied from below to above threshold. The condition for degenerate operation was fulfilled by carefully tuning the temperature. The point of degeneracy was located by searching for interference between the signal wave and the reference wave (local oscillator) as depicted in Fig. 3.29. Lowering the temperature further led to a sudden extinction of the parametric oscillation. For measurements of the states above threshold, a 10 000-times attenuating optical filter was employed to ensure that the homodyning conditions are fulfilled. This of course made it impossible to detect nonclassical noise characteristics above threshold. That plots of this kind were recordable

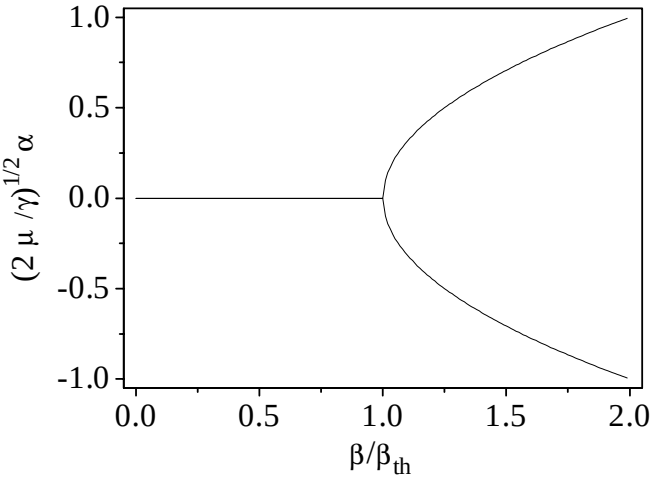

Figure 3.30: *Theoretical plot of the mean electric field amplitude of the OPO below and above threshold β_{th} in dependence of the pump wave's amplitude β. At threshold the mean field solution of the generated subharmonic splits into two stable solutions with a phase difference π, corresponding to the splitting of the phase space distribution into a double-peaked structure.*

at all, considering the extremely unstable behavior of a degenerate OPO at threshold, is due to the OPO's monolithic design, allowing frequency stable operation without locking.

The squeezed vacuum of Fig. 3.31 although only moderately squeezed (4 dB = 0.4 linear scale) is very strongly anti-squeezed (23 dB = 200). It can be seen, that the noise distributions of the transition state depicted in the the middle, have symmetric maxima away from 0. Taking the inverse Radon transform of the sampled distributions of this trace does indeed lead to a double-peaked structure, very similar to the one theoretically expected. It is, however, not clear whether such a 2-dimensional distribution does in fact correspond to a Wigner function of the light field, since there are several aspects of these measurements that are not yet understood:
(a) a frequently occurring overlay of the squeezed vacuum noise with a 2ω sine wave,
(b) the splitting into the double-peaked structure occurred sometimes also at other quadratures than the anti-squeezed one, leading, when applying the inverse Radon transform (which may not be sensible to do) to somewhat distorted phase-space distributions,
(c) the main obstacle: the alternation between the two phases should occur via quantum mechanical tunneling statistically distributed. For the recorded traces phase jumps occured in regular sequences with a frequency of 99 kHz (727 kHz for a different recording). This is the very same behavior which occurs for measurements of coherent states, when modulation frequency and detection frequency (in the MHz regime) are not phase locked to each other. In this setup this was definitely the case. Maybe it is possible, that at threshold the OPO-oscillation can set in at offset frequencies $\neq 0$ within the cavity linewidth. Note also that noise measurements of this kind may be restricted by our two-mode detection method due to considerations outlined in section 3.8.

The last trace in Fig. 3.31 is again well understood. It shows the OPO above threshold, running stably for minutes in the degenerate mode, making it easy to reconstruct its coherent state output in the mW regime (damped by the optical filter as mentioned above).

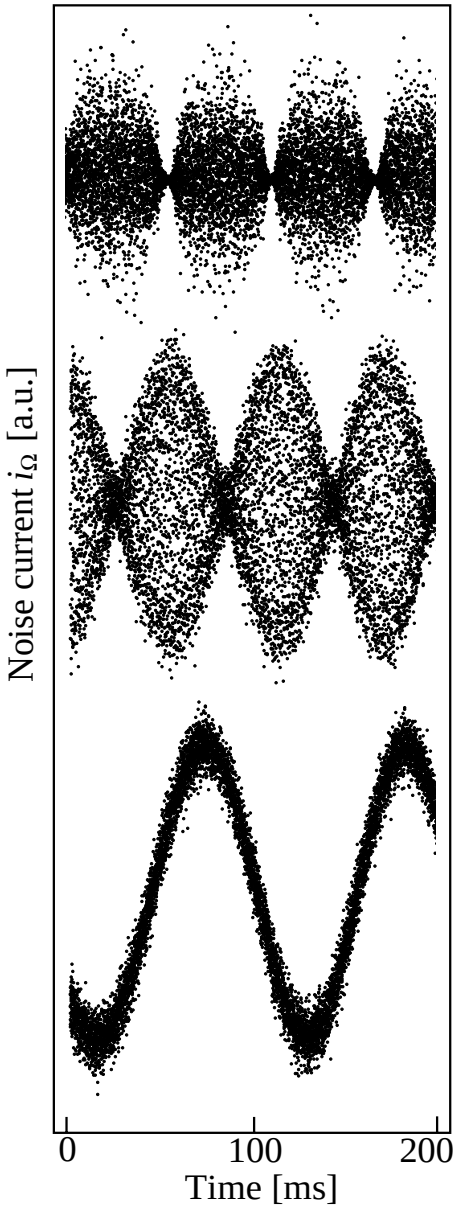

Figure 3.31: *Homodyne noise traces $i_\Omega(t)$ of the quantum states generated by the OPO below, at, and above threshold. The strongly (anti-) squeezed vacuum changes into a coherent state via the transition stage in the middle. The π-periodicity of the quantum noise below threshold changes to a 2π-periodicity of the signal wave.*

As a conclusion, more investigations regarding this system are necessary for a thorough understanding of the unstable regime of the OPO at its oscillation threshold. To do this, parametric devices with much lower threshold powers are needed. With a reduced mean amplitude it would be possible to detect the coherently excited OPO output wave without damping of the field amplitude. Pump power resonant OPOs with threshold powers below 1 mW have been demonstrated [107]. It should be a rewarding project to continue the investigations presented here with monolithic or semi-monolithic devices of this kind.

3.7 Classical superpositions of coherent states

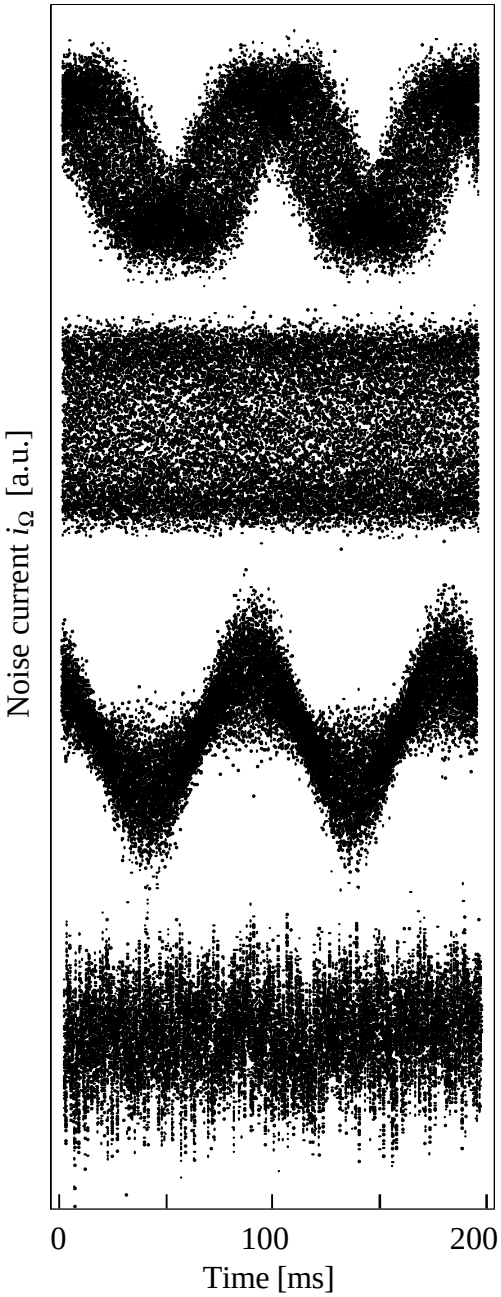

Figure 3.32: *Noise traces i_Ω of incoherent superpositions of coherent states as a function of time. From the top: Partially phase-diffused state, completely phase-diffused state, amplitude-diffused state ($a^2 = 1.0, b^2 = 5.4$), thermal state ($a^2 = b^2 = 14.8$).*

As a demonstration of the applicability of quantum state reconstruction methods to more general states of the light field and to investigate the influence of noise on the measurement system, we studied coherent states with controlled addition of classical noise. Similar experiments have been described in [193]. Since the noise was artificially introduced into the experiment, these measurements may be regarded as being situated somehow between real experiment and simulation. Nevertheless they provide some insight

into the measurement process. For example added phase noise may deteriorate or even extinguish the measured degree of quantum noise reduction of a squeezed state detected by a spectrum analyzer at the output of a homodyne system. Completely phase-diffused squeezed vacuum or coherent states, or thermal states are undistinguishable from one another by plain homodyne variance measurements. Their reconstructed photon number distributions, however, will not only allow to distinguish between these three states, but also furnish the exact degree of squeezing.

Experimentally in contrast to noise suppression below the vacuum level, the addition of noise is one of the easiest tasks to be accomplished in the laboratory. With the setup used to study coherent states, phase noise was added to the signal wave by applying a random modulation (Gaussian noise of 1 MHz bandwidth and, to achieve stronger modulation amplitudes, an additional 2 kHz sine wave) to a piezo-mounted mirror in the signal wave's path before the OPA cavity. Changing the amplitude of the modulation from zero up to one optical wavelength controls the degree of phase diffusion of the state. Amplitude noise was added to the signal wave by modulating with Gaussian noise the amplitude of the r.f. source driving the phase modulator that generated the sidebands at the measurement frequency Ω. Thermal noise is added by either combining these two noise sources, or directly by letting the beam pass through a rapidly rotating transparent wheel with a rough surface, which scatters the light randomly.

Other tested setups to generate classically mixed states involved random light diffraction in air turbulences caused by heating, scattering in suspensions of micrometer-sized latex particles, or a 40 W thermal light source (the latter gave no result at all due to the non-sufficient frequential and spatial mode overlap achieved). Note also that by using square waves instead of random noise for the amplitude modulation, mixtures between 2 (or more) single coherent states can be achieved, resulting in double (or more) peaked structures for the Wigner functions in contrast to the superposition by diffusion of infinitely many coherent states studied below.

The measured noise traces of some of the states are shown in Fig.3.32. Since the amplitude-diffused state's distribution is very similar to the one of a phase-squeezed state it is not analyzed further.

3.7.1 Phase diffused states

The reconstructed Wigner functions of the phase diffused states generated by random mirror modulation are depicted in Fig. 3.33. The process of phase diffusion smears out the Gaussian of the coherent state along a circle in phase space, given by the amplitude of the state. The completely phase-diffused coherent state has been mentioned in [140]. Its Wigner function can be derived as follows: Starting with a coherent state's Wigner function $W(x,y) = 1/\pi \exp[-((x-e_0)^2+y^2)]$, the rotated Wigner function is given by

$$\begin{aligned} W_\theta(x,y) = W(x_\theta, y_\theta) &= \frac{1}{\pi}\exp\left[-(x^2+y^2+e_0^2+2(x\cos\theta + y\sin\theta)e_0)\right] \\ &= \frac{1}{\pi}\exp\left[-(x^2+y^2+e_0^2+2e_0\sqrt{x^2+y^2}\cos(\theta+\alpha))\right] \end{aligned} \tag{3.36}$$

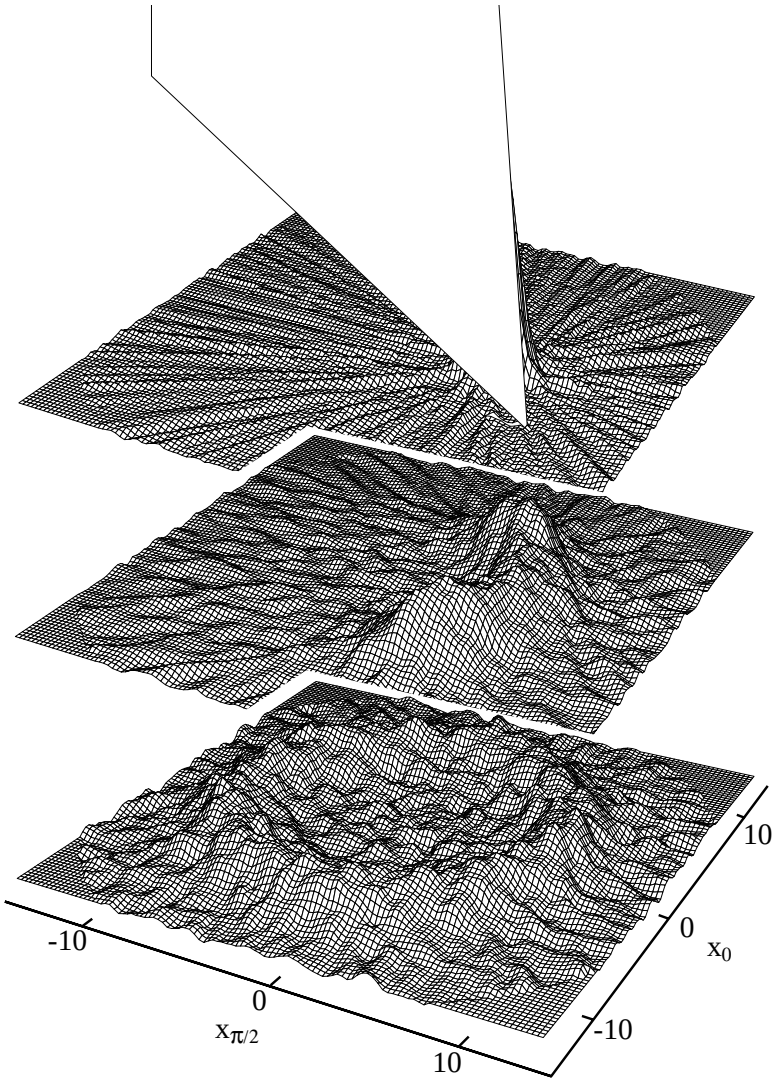

Figure 3.33: *From the top: reconstructed Wigner function of a coherent state, a partially phase-diffused state, and a completely phase-diffused state.*

with $\cos(\alpha) = x/\sqrt{x^2+y^2}$. Averaging $W_\theta(x,y)$ between 0 and 2π and using $\exp(z\cos\theta) = \sum_{-\infty}^{\infty} I_m(z)$ where I_m is the modified Bessel function of order m, we obtain for the completely phase-diffused coherent state

$$\frac{1}{2\pi}\int_0^{2\pi} W_\theta(x,y)\mathrm{d}\theta = \frac{1}{\pi}\mathrm{e}^{-(x^2+y^2+e_0^2)}\, I_0(2e_0\sqrt{x^2+y^2})\,. \tag{3.37}$$

This expression is in good agreement with the measured distribution of Fig. 3.33.

The coherence properties of the generated states are best visualized by the density matrix in the Fock representation. Fig. 3.34 shows how the addition of phase noise to the coherent state leads to an increasing extinction of its off-diagonal elements, while the diagonal elements, that is the Poissonian statistics, remain unchanged.

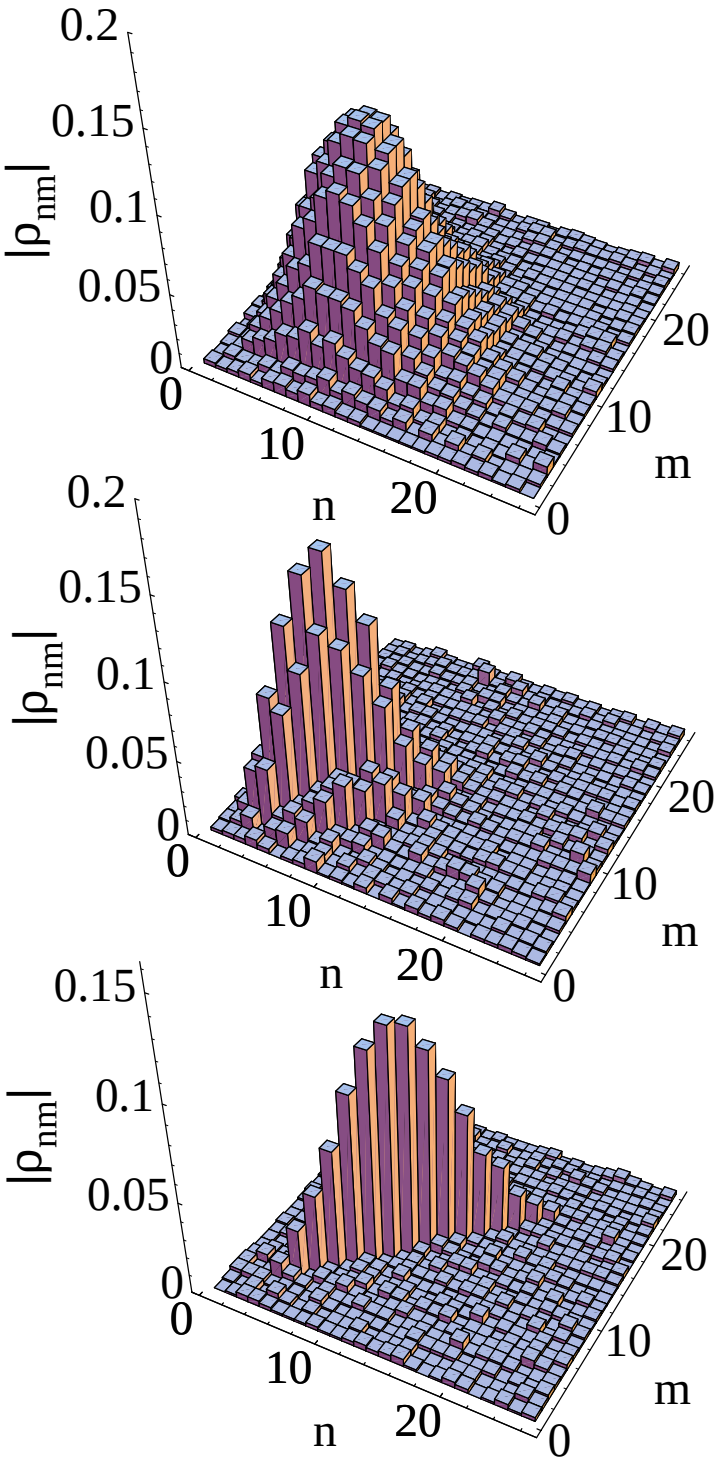

Figure 3.34: *Reconstructed density matrices: (a) coherent state with purity* $Tr\,\rho^2 = 1$*, (b) partially phase-diffused state with* $Tr\,\rho^2 = 0.26$*, (c) completely phase-diffused state with* $Tr\,\rho^2 = 0.09$*. Due to drifts of the signals laser power, the average photon number of the state (b) is slightly smaller than those of the states (a) and (c).*

3.7.2 Thermal states

The last state of the light field we investigated was the thermal state. Since thermal noise is not phase dependent, and has a Gaussian amplitude distribution, the Wigner function of a thermal state is a rotational symmetric two-dimensional Gaussian:

$$W(x,y) = \frac{1}{\pi c^2} \exp\left[-\frac{x^2+y^2}{c^2}\right] . \tag{3.38}$$

Using the expression for the photon statistics of the squeezed vacuum Eq. 2.39 with $a = b = c$ and noting that $P_n^{\mathrm{Leg}}(1) = 1$, we can readily obtain the photon number distribution of a thermal state:

$$p(n) = \frac{2}{c^2+1}\left(\frac{c^2-1}{c^2+1}\right)^n , \tag{3.39}$$

resulting in an average photon number of $\bar{n} = (c^2-1)/2$. Due to the complete phase diffusion of the state the off-diagonal elements of its density matrix are zero, therefore ρ is given by

$$\rho_{nm} = \frac{1}{1+\bar{n}}\left(\frac{\bar{n}}{1+\bar{n}}\right)^n \delta_{nm} , \tag{3.40}$$

in agreement with the experimentally reconstructed matrix shown in Fig. 3.35.

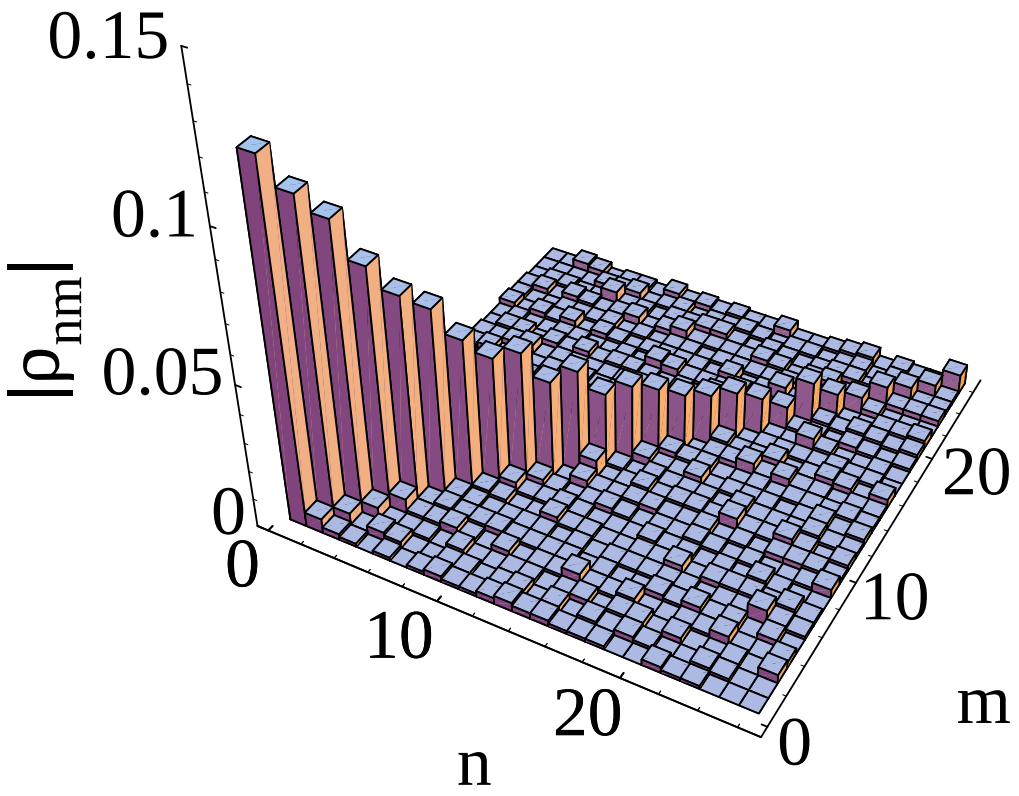

Figure 3.35: *Reconstructed density matrix of a thermal state with* $\langle n \rangle = 6.9$ *and* $Tr\,\rho^2 = 0.079$*, generated by random scattering via a rapidly rotating transparent wheel with a rough surface.*

3.8 Some remarks about two-mode detection

This chapter shows some inherent limitations of the present measurement method and points out possible mistakes when applying the method to general states of the light field.

The crucial attribute of a non-degenerate homodyne measurement, i.e. a measurement with offset frequency $\Omega \neq 0$, is that always two modes of the light field are detected simultaneously. For uncorrelated modes this has certain consequences. Given two modes at frequencies $\omega \pm \Omega$ described by their quadrature operators $\hat{x}_1, \hat{y}_1, \hat{x}_2, \hat{y}_2$ with marginals $P^1_{\theta 1}(x_1)$ and $P^2_{\theta 2}(x_2)$. Let us denote their joint two-dimensional quadrature distribution by $P^{12}_{\theta 1\,\theta 2}(x_1, x_2) = P^1_{\theta 1}(x_1) P^2_{\theta 2}(x_2)$. As pointed out in section 3.1.7, we detect the field difference of the two modes $x = x_1 - x_2$ at $\theta_1 = \theta_2$. In the case of two uncorrelated modes the observed distribution can be written as

$$P_\theta(x) = \int P^{12}_\theta(x_1, x_1 - x) dx_1. \tag{3.41}$$

If one of the modes is in the vacuum state, we have basically the case of heterodyne detection, which due to the overall detection efficiency of less than 0.5 does not yield results valid to perform a quantum state reconstruction [52]. If we assume that both modes are in the same state and have the same marginals $P^1_\theta(x_1) = P^2_\theta(x_2)$ (which is the case for the measurements of the coherent states and the mixed states of section 3.7), we have to have

$$P^1_\theta(x_1) = P_\theta(x) = \int P^1_\theta(x_1) P^1_\theta(x_1 - x) dx_1 \tag{3.42}$$

to be able to interpret the measured two-mode result correctly for the original single modes 1 and 2. This is a severe restriction, since only Gaussian distributions are invariant under autoconvolution.

For a coherent state the marginal of one individual mode is given by $P^1_\theta(x_1) = 1/\pi \exp(-(x_1 - e_0 \cos\theta)^2)$. Thus the measured two-mode distribution given by the integral over the joint marginal distribution amounts to $P_\theta(x) = 1/(2\pi) \exp(-(x - 2e_0 \cos\theta)^2/2)$, that is a distribution broadened by a factor of two with twice the amplitude. Since the vacuum noise is scaled by the same factor of two due to the two-mode vacuum detection, the overall detected state after normalization corresponds exactly to the same state that would be measured in a one-mode detection scheme.

That the measurement of non-Gaussian distributions generated from coherent states described in the preceeding section did yield valid reconstructions is due to the fact that each individual measurement was performed on a coherent state with the state mixing following at a slower time scale. This means, these mixed states or in general uncorrelated states with non-Gaussian marginals can only be detected with the present setup, if the diffusion time between the states (i.e. in our experiment the spectrum of the added classical noise) is long in comparison with the measurement time (i.e. the integration time for one measured point of the recorded noise traces). With a sampling speed of 1.25 MHz and a bandwidth for the introduced noise in the kHz regime, this condition was clearly fulfilled in our experiment.

Completely different is the case of two correlated modes. Here the simultaneous detection of both modes is essential to actually observe the properties that define the

state such as squeezing and photon number oscillations [42]. The decay of squeezing due to detection losses can be regarded as a loss of correlation between the two modes.

It is instructive to look at the joint Wigner distribution of the two-mode squeezed vacuum state. The two-mode squeezing operator

$$S = \exp\left[r(a_1^\dagger a_2^\dagger - a_1 a_2)\right] \tag{3.43}$$

is realized by the process of non-degenerate parametric down-conversion $2\omega \rightarrow \omega_1 + \omega_2$, where due to energy conservation the generated signal and idler waves can be written as $\omega_{1,2} = \omega \pm \Omega$. With the transformations

$$\begin{aligned} S^\dagger x_1 S &= x_1 \cosh(r) - x_2 \sinh(r) \\ S^\dagger y_1 S &= y_1 \cosh(r) + y_2 \sinh(r) \end{aligned} \tag{3.44}$$

the two-mode vacuum Wigner function $W(x_1, y_1, x_2, y_2) = 1/\pi^2 \exp[-(x_1^2 + y_1^2 + x_2^2 + y_2^2)]$ is mapped under the action of the squeezing operator to

$$\begin{aligned} &W(x_1, y_1, x_2, y_2) = \\ &\quad \frac{1}{\pi^2} \exp\left[-\cosh(2r)(x_1^2 + y_1^2) - \sinh(2r)(y_1 y_2 - x_1 x_2) - \cosh(2r)(x_2^2 + y_2^2)\right]. \end{aligned} \tag{3.45}$$

Obviously the quadrature operators of the two modes (x_1, y_1) at frequency Ω and (x_2, y_2) at frequency $-\Omega$ become cross correlated under the action of the squeezing operator. This becomes more transparent when using the decoupled coordinates

$$\begin{aligned} x &= (\alpha_1 + \alpha_2^*)/\sqrt{2} = (x_1 + i y_1 + x_2 - i y_2)/2 \qquad \text{and} \\ y &= (\alpha_1 - \alpha_2^*)/\sqrt{2} = (x_1 + i y_1 - x_2 + i y_2)/2. \end{aligned} \tag{3.46}$$

This substitution transforms the two-mode Wigner function into the well-known Wigner function for the one-mode squeezed vacuum given by Eq. 2.25.

To investigate the distribution of the individual mode at Ω we have to integrate the two-mode Wigner function over x_2 and y_2. Noting that in our previous notation for squeezing $a^2 = \mathrm{e}^{-2r}$ and $b^2 = \mathrm{e}^{2r}$, we arrive at

$$W(x_1, y_1) = \frac{2}{\pi(a^2 + b^2)} \exp\left[-\frac{2(x_1^2 + y_1^2)}{a^2 + b^2}\right]. \tag{3.47}$$

Thus each individual mode is in a thermal state. Only the correlations between the modes at Ω and $-\Omega$ bring about the squeezing properties. Comparing this with Eq. 2.25 of section 2.2 and setting $c^2 = (a^2 + b^2)/2$ we obtain for the mean photon number from Eq. 3.39 directly $\bar{n} = (a^2 + b^2 - 2)/4$. Which shows as expected that for two perfectly correlated modes the mean photon number of the individual thermal state is the same as for the two-mode squeezed vacuum state (Eq. 3.17). This also explains the exponential envelope of the even photon number probabilities for the squeezed vacuum state seen in Fig. 3.16.

To actually detect two-mode correlations via the two single mode thermal states explicitly, two-mode quantum state reconstruction schemes have to be applied as proposed in [193, 192]. For measurements of states of the light field, where the correlation of frequential modes is asymmetric or three- or more mode correlations exist, the method of non-degenerate homodyne detection is hardly usable anymore. In such cases the experiment has to be modified to allow for degenerate measurements at $\Omega = 0$ [228].

3.9 Broadband reconstruction
Generating a spectrum of quantum states

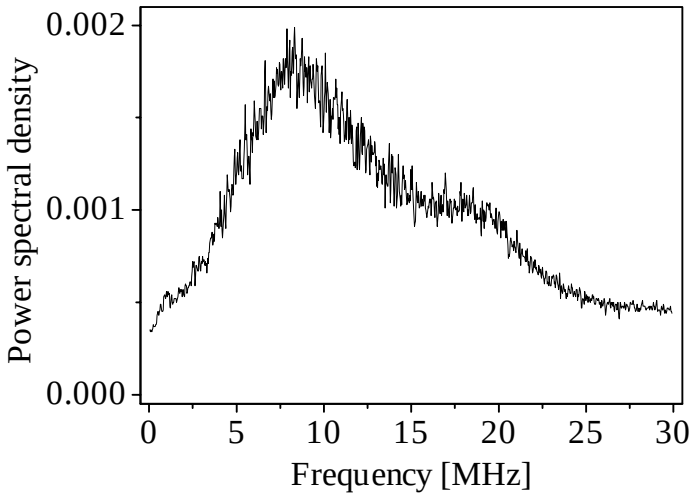

Figure 3.36: *Frequency response of the detection system for measurements of broadband quantum state reconstruction.*

The reconstructions presented so far were limited to essentially one particular pair of modes at frequencies $\omega \pm \Omega$. The spectral bandwidth of this mode pair was $\Delta\Omega/2\pi$ = 100 kHz. Since an OPA pumped below threshold emits a frequency *spectrum*, with a bandwidth determined by the cavity linewidth, the output of the OPA is described more precisely by a whole spectrum of quantum states. General schemes for multimode reconstruction become quite complicated already at the two-mode level [174, 192, 193]. So far only one experiment demonstrating photon-number correlations in the time domain by measuring the photon statistics via dual-pulse phase-averaged homodyne detection has been carried out [154]. In the measurements presented in this section the whole "spectrum" of density matrices and Wigner functions is obtained and the first order correlation function in the time domain is evaluated. Considering the whole information contained in the multimode space spanned by the emitted quantum states, we have measured exactly along the diagonal of this space.

In order to obtain simultaneously information about the quantum states of all modes emitted by the OPA, the homodyne detector current i_- was recorded with a bandwidth $\Delta\Omega$ covering the range from 2 to 30 MHz, exceeding the OPA's 17.5 MHz cavity linewidth. The data's frequency spectrum for a measurement of the vacuum state is shown in Fig. 3.36. This figure has to be compared with Fig. 3.7 in the previous single-mode measurements. The steep drop off at low frequencies is due to a low pass at 1 MHz employed only in these broad band measurements. The main (nonlinear) frequency dependence at higher frequencies is due to impedance mismatch of the A/D-converter. The photodetectors (including their amplification circuits) show only a very small power decrease in the shown frequency range, their responsivity (including amplification circuit) was measured to go beyond 80 MHz (140 MHz specified for ETX500T). With a local oscillator power of 2 mW the shot noise level is 14 dB above the electronic noise level of the detectors at lower frequencies and 5 dB for frequencies between 24 and 30 MHz. To avoid disturbances

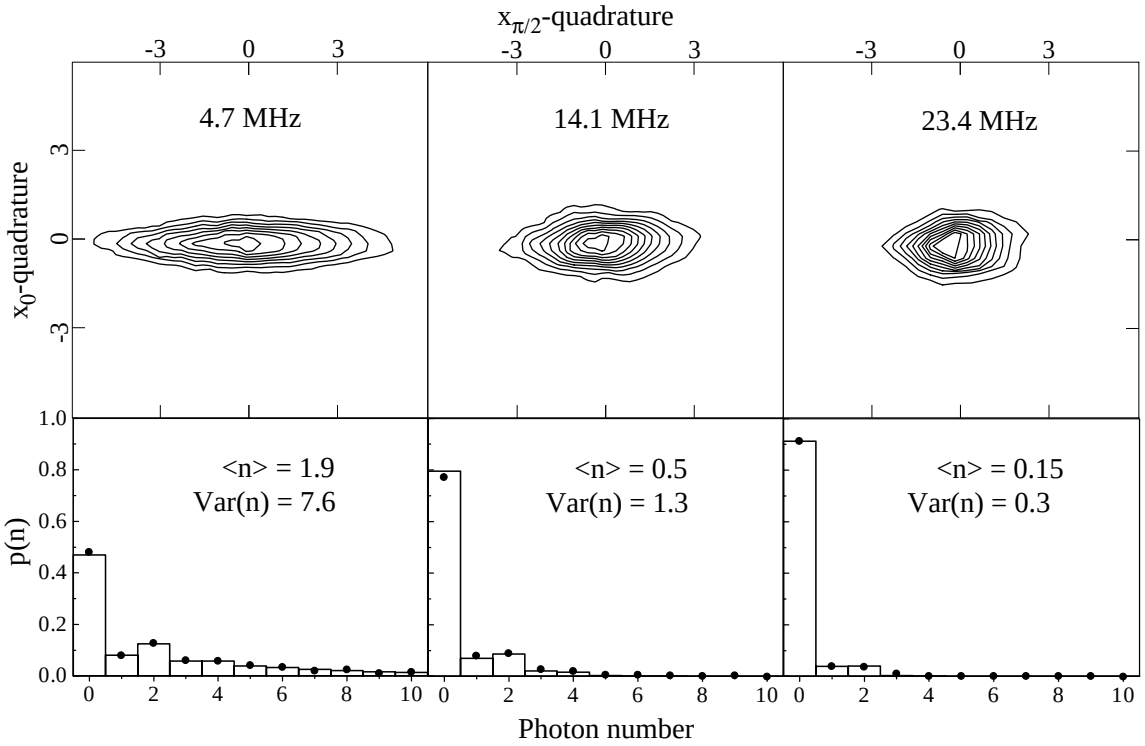

Figure 3.37: *Three examples of the simultaneously recorded squeezed vacuum states emitted by the OPA: Upper row: contours of the Wigner functions, lower row: corresponding reconstructed photon number distributions (dots) with theoretical expectations (histograms). For increasing offset frequency Ω from the OPA cavity center frequency the states aproach the vacuum state and the characteristics of squeezing such as photon number oscillations and ellipticity of the Wigner function vanish.*

in the spectrum by the frequency doubler, the locking frequency for the Pound-Drever stabilization was shifted to 75 MHz.

Although the strong frequency dependence of the data recording does account for a different quality of state reconstructions at different frequencies, it does not present a major obstacle for the measurement, since the noise traces can be normalized in Fourier space or normalized for each mode seperately by multimode vacuum state detection.

As in the single-mode measurements, the homodyne data of the squeezed vacuum state are taken while the local oscillator phase is swept by 2π, resulting in noise traces similar to the ones presented in section 3.2, the measurement time being approximately 8 ms. The recorded noise trace is split into 16 separate traces, each containing the information of a mode pair of small bandwidth, centered at a sideband frequency $\pm\Omega$. This is done by dividing the Fourier transform of the recorded trace into 16 equal intervals, and taking the inverse transform of each interval separately. The same is done for a measured $i\_$-trace of a vacuum state, in order to normalize each of the 16 traces. Due to high electronic noise at low frequencies the first of the 16 traces, containing the spectrum between 0 and 1.875 MHz, is discarded. The quantum states of the remaining 15 modes can be reconstructed the same way as before, employing the pattern fuctions of the harmonic oscillator and the inverse Radon transform. Thus a whole "spectrum" of Wigner functions and density matrices is obtained from a single temporal record.

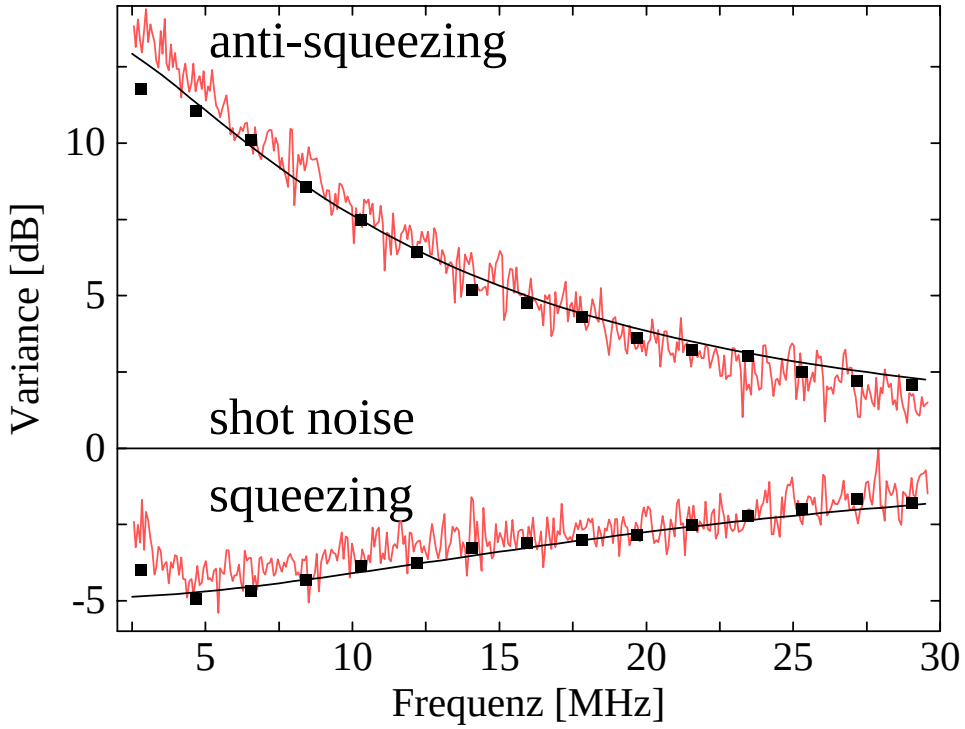

Figure 3.38: *Spectrum of squeezing and anti-squeezing: Spectrum analyzer traces (upper and lower grey lines) in comparison with a theoretical fit (smooth black lines). Each of the 15 pairs of black squares corresponds to one reconstructed quantum state at a specific frequency Ω and represents the maximum/minimum width of the sampled marginal distributions. The reduction in squeezing at frequencies below 4.5 MHz is due to classical laser noise at low frequencies.*

3.9.1 Analysis in the frequency domain

The main difference between the squeezed vacuum states reconstructed at different Ω is the amount of noise reduction (squeezing) and enhancement (antisqueezing). The spectra of quantum noise power of the squeezed quadrature Ψ_- and of the antisqueezed quadrature Ψ_+ of an OPA on resonance are given by Eq. 2.53.

In contrast to the single-mode measurements the mode cleaning cavity was not employed, since due to lack of space for another experiment the setup had already been partially dismantled. Thus classical noise of the pump wave was not negligible and the modematching between local oscillator and the OPA output signal was $\approx 95\%$. Furthermore the efficiency of the photo detectors had degraded slightly, thus the overall detection efficiency including escape efficiency $\xi \cdot \eta$ was fitted to be 0.7. The pump power was approximately half the threshold power and the cavity linewidth (HWHM) was , $/2\pi = 17.5$ MHz.

Fig. 3.38 shows the spectra of the maximally squeezed and anti-squeezed quadratures measured directly with a spectrum analyzer in comparison with the ones obtained via multimode reconstruction. Three of the reconstructed states are plotted in Fig. 3.37. They display strongly elliptical Wigner functions and oscillations in the photon number, characteristics that vanish when the state aproaches a vacuum state at frequencies sufficiently away from the OPA cavity center frequency.

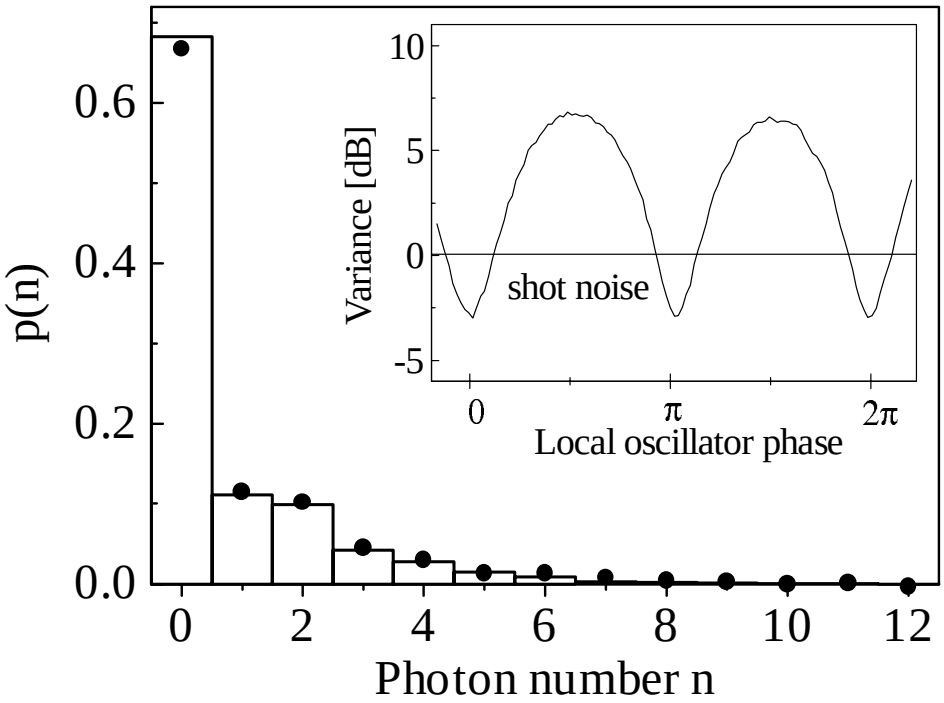

Figure 3.39: *Electric field variances in dependence of the local oscillator phase and photon statistics of the sum of all OPA modes between 2 and 30 MHz. The average photon number $\langle n \rangle = 0.8$ gives the average photon flux per Hz bandwidth. This implies a total photon flux of $2.2 \cdot 10^8$ photons/s ≈ 45 pW within the detection bandwidth of 28 MHz.*

A direct measure of the total noise of the squeezed and anti-squeezed quadratures $\int \Psi_{\pm}(\Omega, P) d\Omega$ of the overall OPA output within the bandwidth 1.9-30 MHz is obtained by analyzing the full quantum noise instead of its particular Fourier components (for this, the non-uniform spectral response of the A/D-board has to be eliminated via normalization in Fourier space). The inset of Fig. 3.39 shows the total electric field variances as a function of the local oscillator phase. Well-known figures of this type usually depicted only the E-field variances of a single mode of the light field [227, 276, 232, 184, 112, 31]. Here we obtain for the overall OPA output a total squeezing of -2.9 dB (= 0.47 linear scale) and 6.7 dB (= 4.7) for the total antisqueezing. The corresponding photon statistics is shown as well. This multimode light field would be detected if photon counters were employed instead of homodyne detection. Note that no photon number oscillations are observable in the total OPA output. This may seem surprising, since almost all the photon number distributions of the individual modes show oscillations and all the reconstruction transformations are linear. However, according to basic laws of probability theory the overall sampled distribution of the quantum noise is not given by the average but by the convolution of the distributions of the individual modes. Therefore the photon statistics of the total OPA output is not given by averaging the single mode statistics (for simple instructive examples consider for instance the two-mode mixing of a squeezed vacuum and a vacuum state or of two squeezed vacuum states with relative phase difference of $\pi/2$). What is averaged though in our case of uncorrelated Gaussian noise distributions is, as mentioned above, the variance at each particular phase angle.

3.9.2 Analysis in the time domain

A further perspective is gained by the analysis of our data in the time domain. At a fixed phase θ of the local oscillator, the recorded time trace can be regarded as the quantum trajectory of the quadrature $x_\theta(t) = 2^{-1/2}(a^\dagger(t)\,\mathrm{e}^{\mathrm{i}\theta} + a(t)\,\mathrm{e}^{-\mathrm{i}\theta})$, denoting by $a(t)$ the output field operator. Thus the recorded data contain all information needed to extract the first order correlation function of the field operators $g_{(1)}$ since the latter can be easily expressed in terms of the correlation function of the quadrature operators

$$\begin{aligned} g_{(1)}(\tau) &\equiv \frac{\langle a^\dagger(\tau)a(0)\rangle}{\langle a^\dagger(0)a(0)\rangle} \\ &= \langle (x(\tau)x(0) + y(\tau)y(0)\rangle/2 \\ &= \frac{\langle x_\theta(\tau)x_\theta(0)\rangle_\theta}{\langle x_\theta(0)x_\theta(0)\rangle_\theta}\,. \end{aligned} \tag{3.48}$$

Here $<>_\theta$ means averaging over all phase angles. This function is easily calculated using the input-output formalism for optical cavities of section 2.4. Since the frequency dependence of a and $a^\dagger$ is known in Fourier space, the application of the inverse Fourier transform directly gives the autocorrelation function by the Wiener-Khintchine theorem. Alternatively $g_1(\tau)$ is found by calculating the power spectrum of the electromagnetic field. For the squeezed vacuum, having no coherent excitation, this is given by the average of the variances of the quadrature component distributions $P_\theta(x,\Omega)$ over one oscillation period.

$$\begin{aligned} |E(\Omega)|^2 &= \frac{1}{2\pi}\int_0^{2\pi}\int_{-\infty}^{\infty} x^2 P_\theta(x,\Omega)dxd\theta \\ &= \frac{1}{2\pi}\int_0^{2\pi} w_\theta(\Omega)d\theta \\ &= \frac{1}{2}(a(\Omega)^2 + b(\Omega)^2) \end{aligned} \tag{3.49}$$

where $w_\theta(\Omega) = \sqrt{a(\Omega)^2\cos^2\theta + b(\Omega)^2\sin^2\theta}$ and $a(\Omega)^2 = \Psi_-(\Omega,P)$ and $b(\Omega)^2 = \Psi_+(\Omega,P)$ are the spectra of squeezing and anti-squeezing defined by equation 2.53. The first order correlation function follows straight by taking the inverse Fourier transform and normalizing to $g_1(0) = 1$. Both ways we arrive at

$$g_{(1)}(\tau) = \frac{1-d^2}{2d}\left[\frac{1}{1-d}e^{-(1-d)\Gamma\tau} - \frac{1}{1+d}e^{-(1+d)\Gamma\tau}\right]. \tag{3.50}$$

Fig. 3.40 shows this quasi-exponential decay similar to the one of a thermal state [140]. The experimental data are in good agreement with theory.

Since the Fokker–Planck equation of the system is linear in the fluctuation terms, its stationary solution is Gaussian, thus all the normalized higher–order, multi–time correlation functions $g_{(n)}(a^\dagger(t_1),...,a(t_n))$ can be expressed as sums of products of the second moments of the distribution. Therefore, knowledge of the normalized two–time correlations $g_{(1)}(\tau)$ and $g_{(2)}(\tau)$ is enough to reconstruct the whole time statistics.

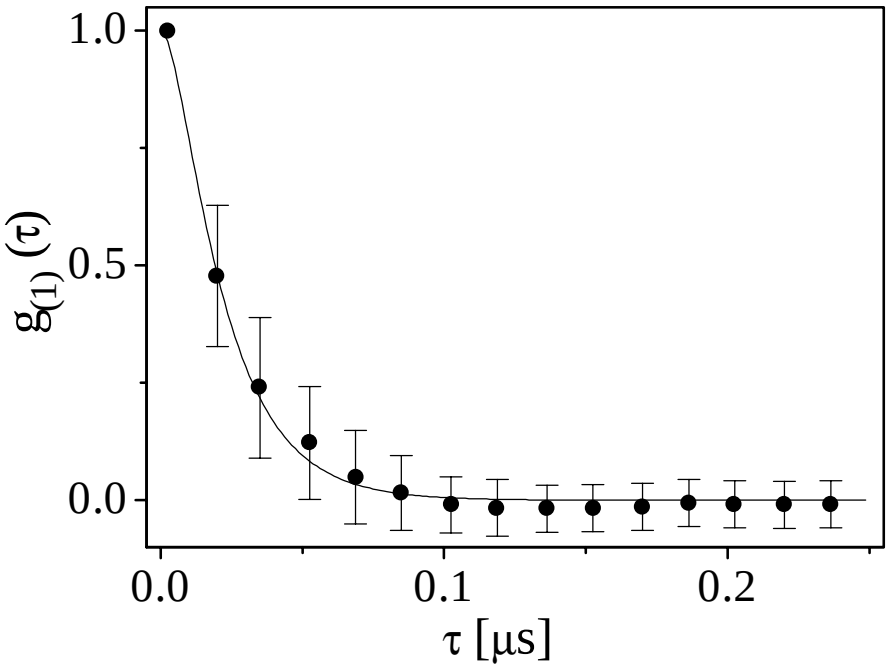

Figure 3.40: *First order time correlation function $g_{(1)}(\tau)$ of the squeezed vacuum state (dots) in comparison with theory (line).*

Applying the Gaussian decomposition to the intensity–intensity correlation $g_{(2)}$ we get

$$\begin{aligned} g_{(2)}(\tau) &\equiv \frac{\langle a^\dagger(0)a^\dagger(\tau)a(\tau)a(0)\rangle}{\left(\langle a^\dagger(0)a(0)\rangle\right)^2} \\ &= \frac{\langle a^\dagger(0)a^\dagger(\tau)\rangle\langle a(\tau)a(0)\rangle + \langle a^\dagger(0)a(\tau)\rangle\langle a^\dagger(\tau)a(0)\rangle + \langle a^\dagger(0)a(0)\rangle\langle a^\dagger(\tau)a(\tau)\rangle}{\left(\langle a^\dagger(0)a(0)\rangle\right)^2} \\ &= \frac{(1-d^2)^2}{4d^2}\left[\frac{e^{-2(1-d)\Gamma\tau}}{(1-d)^2} + \frac{e^{-2(1+d)\Gamma\tau}}{(1+d)^2} + \frac{e^{-2\Gamma\tau}}{1-d^2}\right] + g^2_{(1)}(\tau) + 1\,. \end{aligned} \tag{3.51}$$

The normalized intensity–intensity correlation at equal times is then

$$g_{(2)}(0) = \frac{3+d^4}{4d^2} + 2\,. \tag{3.52}$$

The vacuum limit $d \to 0$ of the normalized intensity–intensity correlation is known to be ill–defined and strongly dependent on the initial state; for instance, it is 1 if one starts from a single mode in a coherent state. It instead diverges as the inverse of the second power of the squeezing parameter if one starts from a pure single mode squeezed state [266]. One can immediately see that this peculiar behavior is preserved also in the case of the multimode squeezed output from the parametric amplifier.

For the evaluation of higher order correlation functions $g_{(n)}$, $(n > 1)$ from the measured data we need to substitute the time dependent field operators $\hat{a}(t)$ and $\hat{a}^\dagger(t)$ by the quadrature operators $X(t)$, $Y(t)$. Due to the time dependent commutators this substitution is quite complicated. In particular it involves terms like $X(t)Y(t)$, i.e. products

of conjugated quadrature operators at equal times. These are not measurable with the present setup where different quadratures are detected by changes in the phase of the light field. A possible solution would be to employ an eight port homodyning scheme, such as the one used for Q-function determination [263]. This is possible, since detection efficiency does not play the same crucial role in time correlation measurements which it does for quantum state reconstructions. In fact ideally $g_{(n)}$ is independent of η. Such a scheme would also render possible single-mode time correlation measurements instead of the here presented two-mode measurements.

The quantities that are in principle measurable though with the present setup are all higher order time correlations of the field quadratures $\langle x_\theta(\tau_1)x_\theta(\tau_2)...x_\theta(\tau_n)\rangle$. Except for one special case [150] their significance does not appear to have been studied. For the measured data the evaluation of these correlations could not be done reliably, because of difficulties with a proper normalization at $\tau = 0$ and since the minimum recordable timestep of 1.7 ns was too large in comparison to the expected rapid exponential decay times $e^{-n(1-d)\Gamma\tau}$.

3.10 Overview

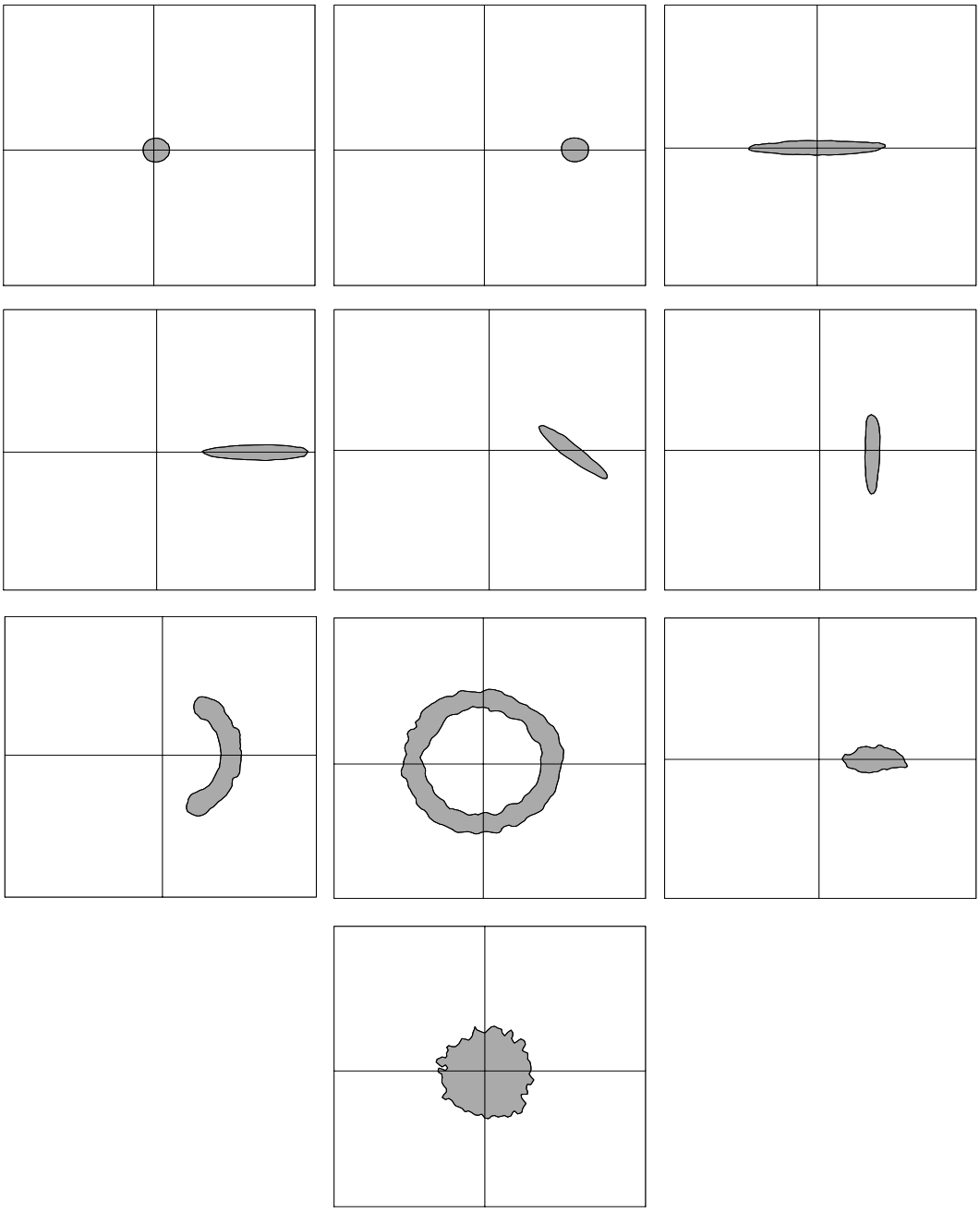

Figure 3.41: *Wigner function contours of the reconstructed states of the preceding chapters. All basic types of squeezed states and classical diffused states have been generated and in detail analyzed. Top row from left to right: vacuum state, coherent state, squeezed vacuum state; second row from left to right: phase-squeezed state, 48°-quadrature-squeezed state, amplitude-squeezed state; third row from left to right: partially phase-diffused coherent state, completely phase-diffused coherent state, amplitude-diffused coherent state; bottom row: thermal state. Since there is still some space left, the gentle reader may attempt to his own delight the drawing of the contour plot of a partially phase-diffused squeezed vacuum state.*

3.11 Outlook part I

Besides the mentioned unfinished projects: Schleich-Wheeler oscillations for bright squeezed states (Sec. 3.4 and 3.5.1), investigation of the OPO above threshold (Sec. 3.6), and the measurement of higher order correlation functions (Sec. 3.9), possible continuations of the here presented measurements are the generation and quantum state analysis of new states of the light field with non-Gaussian statistics using higher order nonlinear processes [65] or the investigation of the one-photon (Fock) state by coincidence homodyne measurements [284] (for latest developments see [83]).

Quantum optical investigations of higher order nonlinear processes started already in the eighties, labeled by the term "generalized squeezing" [68, 27]. The case of a third order nonlinear susceptibility $\chi^{(3)}$, resulting in three-photon downconversion $3\omega \rightarrow \omega + \omega + \omega$, which up to now has not been demonstrated experimentally, was considered theoretically in detail by Timo Felbinger in our group [65]. A degenerate resonant three-photon downconversion oscillator (TDO) exhibits a behavior similar to the one of an OPO [6, 65]: The TDO, pumped by the 3ω-wave, has a certain threshold P_{th} for the pump field strength P, above which it starts oscillating at ω. The phase of the ω-wave is defined up to a phase factor of $2\pi/3$. Thus, including the zero solution which, in contrast to the 2-photon OPO remains a stable solution for the subharmonic wave above threshold, four stable solutions for the ω-wave exist. Accordingly, the phase space distribution of the light field at frequency ω exhibits a threefold symmetry below and above threshold. Fig. 3.42 shows the noise trace of such a subthreshold pumped TDO. It was generated by Timo Felbinger, using the method of quantum trajectory simulations. Applying to these data the inverse Radon transform yields the phase space distribution depicted in Fig. 3.43. In a single pass configuration, as opposed to the cavity-resonant scheme, oscillations between the three arms of the Wigner function occur due to phase space interference [8] similar to the one described in Sec. 3.4.5. As outlined in Sec. 3.2.2, the measurement of the third-order statistical moment of the light field's quadrature distributions may provide the first evidence indicating the third order nonlinear interaction at the quantum level. Care has to be taken when considering the technique of non-degenerate homodyne detection as applied in this thesis, since the relevant output field of the TDO at frequencies $\neq 0$ is a three-mode field.

First practical considerations: Assuming a doubly resonant cavity and degenerate operation with an interaction hamiltonian

$$\hat{H}^{(3)} = -\frac{\hbar}{i}\kappa^{(3)}\left(\hat{a}^{\dagger 3}\hat{a}_3 - \hat{a}^3\hat{a}_3^{\dagger}\right) , \tag{3.53}$$

the threshold for the TDO is given by

$$P_{\mathrm{th}} = \frac{8}{27}\frac{\hbar\omega_3\gamma^{\frac{3}{2}}\gamma_3^{\frac{1}{2}}}{\kappa^{(3)}} , \tag{3.54}$$

where $\gamma_3 = T_3/2\tau$ and $\gamma = T/2\tau$ are the scaled losses of the harmonic and subharmonic wave in a resonator of length L with index of refraction $n = \epsilon^2$, round trip time $\tau = nL/c$, and linear losses T_3 and T respectively, $\omega_3 = 3\omega$ is the frequency of the pump wave, and

$$\kappa^{(3)} = -\frac{3\sqrt{3}\hbar\omega^2}{16\epsilon_0\epsilon^2}\chi^{(3)}\frac{1}{V} \tag{3.55}$$

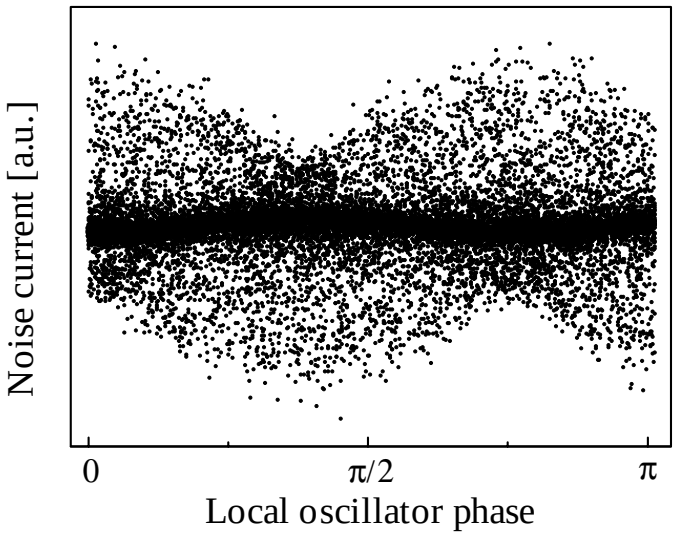

Figure 3.42: *Noise trace of the output of a 3-photon OPO generated by quantum trajectory simulations.*

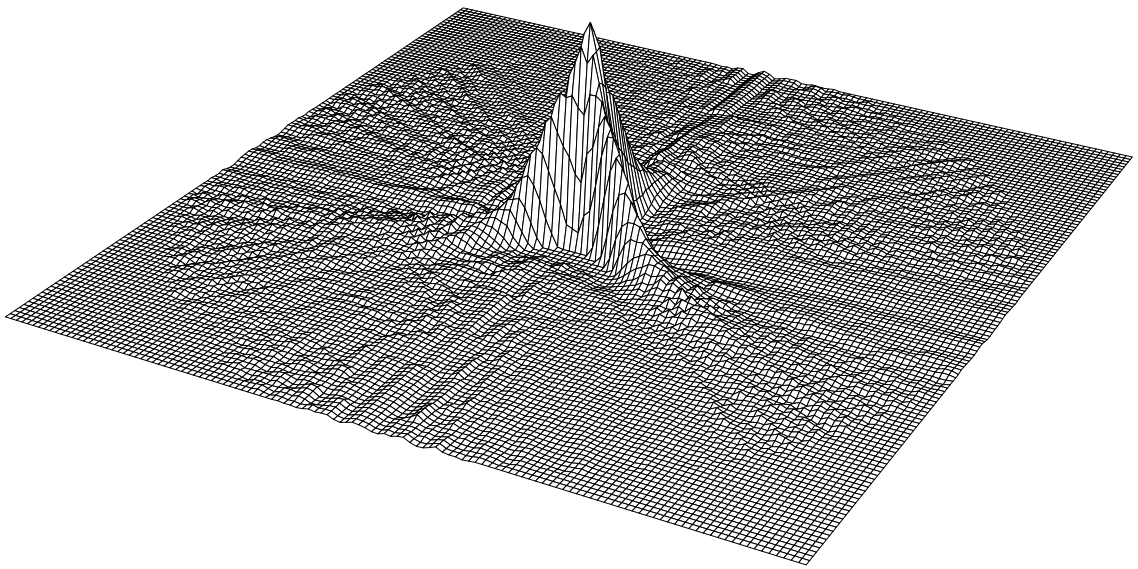

Figure 3.43: *Corresponding Wigner function. Because of its threefold symmetry, the state is also called star state.*

is the coupling constant assuming a mode volume V. To get first estimates we can approximate

$$P_{\text{th}} \approx 10^{-16}\text{W}\frac{\sqrt{T^3 T_3}}{\chi^{(3)}}\frac{m^2}{V^2} \tag{3.56}$$

As mentioned above, so far no experiments demonstrating 3-photon down conversion have been done. Values for $\chi^{(3)}$ have been obtained via third harmonic generation. The following table gives an overview over the main experiments performed so far (another class of materials, doped fibers, is still under investigation):

Material	$\chi^{(3)}$ [m^2/V^2]	**Wavelength [nm]**	**Reference**
BBO, crystal	$4.2 \cdot 10^{-22}$	1064	[186, 248] (see also [277])
$LiIO_3$, crystal	$9.1 \cdot 10^{-21}$	1064	[170]
rutile, crystal	$5.6 \cdot 10^{-20}$	1900	[84]
org. crystals	$\approx 5 \cdot 10^{-18}$		[125, 181]
Rb:Xe, gas	$3.9 \cdot 10^{-27}$	1064	[282, 15, 187]
doped glasses	$5.6 \cdot 10^{-19}$	2100	[121, 243]

As can be seen, even without adressing the problem of phase matching [87], threshold powers in the order of 100 W can be expected. In addition, related to the different classical behavior at threshold it was found that in contrast to the 2-photon OPO for the light field emitted from the TDO-cavity a significant deviation from the vacuum state Wigner function does not occur for pump powers near threshold but much higher [65]. In conclusion further developments of $\chi^{(3)}$-materials are necessary before successful measurements of the light field of a star state can be performed.

A second proposal, suggested to us by Ulf Leonhardt, is the investigation of the one-photon state by coincidence honodyne measurements [284]: Of the output of a two-photon source (a non-degenerate parametric downconverter) one photon serves as the trigger photon (state preparator) for the measurement of the second photon by a homodyne detector. By statistical analysis of the homodyne detector output, similar to the one presented in this thesis, the quantum state of the single photon can be mapped out, providing an unprecedent detailed experimental description of the elementary excitation of the electromagnetic field.

*

4 Introduction to part II

At the quantum level, a measurement disturbs the system being measured. The back action due to the quantum nature of the probe is usually very small and has not yet been observed for a macroscopic system. The existence of the quantum back action leads to the appearance of a quantum limit in the accuracy of measurements, the standard quantum limit (SQL) [25]. For measurements of the position of a harmonic oscillator of mass m and resonance frequency ω_m this is $\Delta x_{SQL} = \sqrt{\hbar/m\omega_m}$. For a laser interferometric position measurement, the back-action can be understood in a straightforward manner [61, 175]. The probing laser wave carries quantum fluctuations. For a coherent state of light, the quantum uncertainties of phase and intensity are equal and proportional to the square root of the laser power P. The intensity quantum fluctuations cause radiation pressure noise which leads to displacement noise whose uncertainty scales with $\sqrt{P}$. At a high enough laser power this noise will become appreciable. On the other hand, the read-out uncertainty due to quantum noise scales with $1/\sqrt{P}$, since the signal is $\sim P$, thus it dominates at low laser powers. An optimum laser power exists that minimizes the sum of the read-out noise and that due to back action. The measurement accuracy corresponding to this optimum readout precision is the standard quantum limit (SQL). The SQL is of fundamental interest, because it limits the sensitivity with which an external force acting on the macroscopic body may be detected using coherent light [17].

The observation of quantum effects with optomechanical sensors requires the development of oscillators with low loss and low spring constant, their integration into a sensitive read-out system, and minimization of the oscillator's thermal noise, which can easily mask the quantum effects. While optomechanical systems have received considerable theoretical attention [61, 39, 40, 141, 253, 20, 157, 138, 101, 88, 143, 175, 63, 148, 86], only few experimental studies have been performed after the first observation of the DC radiation pressure in an optical cavity [58].

In this second part of the thesis the setup of a cryogenic optomechanical system based on a Fabry-Perot cavity with a movable mirror is presented which has the essential features to allow observation of quantum back action and the standard quantum limit.

After a brief introduction to the theory of optomechanical systems, the experimental work is presented, starting with a characterization of the employed mechanical oscillator, in section 6.1, followed by a description of the overall setup in section 6.2–6.4, and the first measurements in section 6.5. A comparison with similar experiments by other groups is given in section 6.5.1, concluded by a short outlook.

5 Theory II: A cavity with a movable mirror

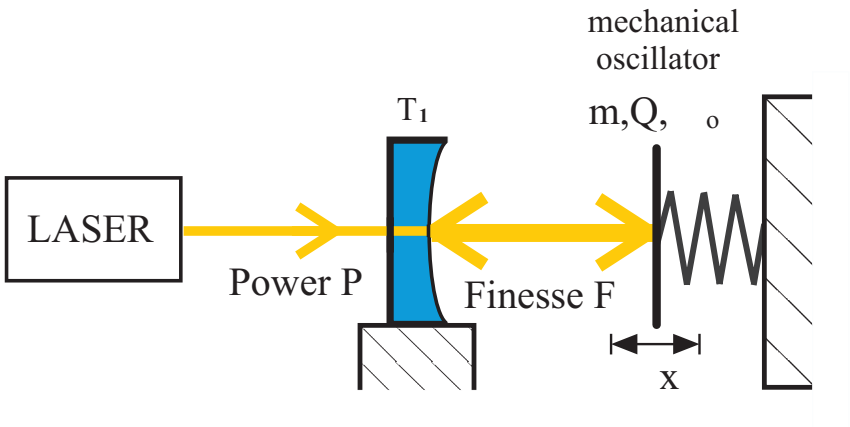

Figure 5.1: *Sketch of the experiment consisting of a laser source and a Fabry-Perot cavity. Goal is a precision measurement of the movable mirror's position.*

5.1 Mechanical harmonic oscillation

The one dimensional mechanical harmonic oscillator without application of external forces is decribed by the equation of motion

$$m\ddot{x} + \delta\dot{x} + kx = 0, \tag{5.1}$$

where m is the oscillator's mass, δ is the friction, and k is the spring constant. The equation is solved by an exponentially decaying harmonic oscillation

$$x(t) = x_0 \mathrm{e}^{-\gamma t} \mathrm{e}^{i(\omega_m t + \Phi)} \,. \tag{5.2}$$

Here $\gamma = \delta/2m$ denotes the damping coefficient, which is the inverse of the decay time $\tau^* = 1/\gamma$ and

$$\omega_m = \sqrt{\frac{k}{m} - \frac{\delta^2}{2m^2}} = \omega_0 \sqrt{1 - \frac{1}{2Q^2}} \tag{5.3}$$

denotes the oscillator's resonance frequency, with $\omega_0 = \sqrt{k/m}$ being the resonance frequency of the undamped oscillator and $Q = \omega_0 \tau^*/2 = \sqrt{k\,m}/\delta$ being the mechanical quality factor. The Q-factor is proportional to the oscillator's relative energy dissipation

per oscillation period. In the following sections I will use the experimentally realistic approximation $\omega_m \approx \omega_0$.

The response of the mechanical oscillator to the excitation by an external harmonic force $F(t) = F_0 \exp(\mathrm{i}\omega t)$ is given by the mechanical susceptibility

$$\chi(\omega) = \frac{x(t)}{F(t)} = \frac{1}{m(\omega_0^2 - \omega^2 - i\omega\omega_0/Q)}\,. \tag{5.4}$$

Consequently the spectral displacement density $S(\omega)$ of the response to an external force F with spectral density $S_F(\omega)$ is given by

$$S(\omega) = |\chi(\omega)|^2\, S_F(\omega)\,, \qquad \text{with} \tag{5.5}$$

$$\begin{aligned} |\chi(\omega)|^2 &= \frac{1}{m^2\left[(\omega^2 - \omega_0^2)^2 + \omega^2\omega_0^2/Q^2)\right]} \\ &= \frac{1}{m^2\left[\left(\omega^2 - \omega_0^2(1-\frac{1}{2Q^2})\right)^2 + \frac{\omega_0^4}{Q^2}(1-\frac{1}{4Q^2})\right]} \end{aligned} \tag{5.6}$$

The latter expression makes it easier to read off the response's maximum at ω_m and the corresponding resonance width $\Delta\omega \approx \omega_0/Q$ (FWHM) for $Q \gg 1$.

The overall response of the system to an external force is given by the integral $\int S(\omega)\mathrm{d}\omega$. Since the forces considered in this experiment, photon recoil and Brownian noise, are not explicitly frequency dependent, i.e. stem from white noise sources, the total displacement in response to these forces is proportional to the integral over the squared susceptibility. This integral is solved by residue calculus to

$$\int_0^\infty \chi(\omega)^2\,\mathrm{d}\omega = \frac{\pi\, Q}{2m^2\omega_0^3}\,. \tag{5.7}$$

5.2 The Fabry-Perot interferometer, FM detection

The position of the mechanical oscillator, which forms one mirror of a Fabry-Perot cavity, can be monitored by detecting intracavity phaseshifts of the light reflected from the resonator. This is done by using a frequency modulation (FM) technique described in [59, 91]. For an empty cavity with internal losses A, an incoupling mirror with reflectivity R_1 and a rear mirror with reflectivity R_2, the ratio of the E-field of the reflected wave versus the one of the incoming wave as a function of the detuning Φ is given by [226]

$$C(\Phi) = \frac{E_r}{E_i} = \frac{\sqrt{\rho/R_1}\, e^{i\Phi} - \sqrt{R_1}}{1 - \sqrt{\rho}\, e^{i\Phi}}\,, \tag{5.8}$$

where $\rho = R_1 R_2 A$ is equal to one minus the overall losses.

The incoming wave of frequency ω_L is frequency modulated with a modulation index ϵ at the frequency Ω

$$E_i = E_0 \exp[\,\mathrm{i}\,(\omega_L t + \epsilon \sin \Omega t)]\,. \tag{5.9}$$

This expression simplifies in first order approximation to

$$E_i = E_0\,[J_0(\epsilon) + J_1(\epsilon)(e^{\mathrm{i}\Omega t} - e^{-\mathrm{i}\Omega t})] \exp(\mathrm{i}\omega_L t)\,, \tag{5.10}$$

denoting by J_n the n^{th} Bessel function. The reflected wave consists of three terms

$$E_r = E_0\,J_0(\epsilon)\,C(\Phi) + E_0\,J_1(\epsilon)\,C(\Phi_\Omega) - E_0\,J_1(\epsilon)\,C(\Phi_{-\Omega})\,, \tag{5.11}$$

where we used Eq. 5.8 with $\Phi_\Omega = \Phi + \Omega 2L/c$ and $\Phi_{-\Omega} = \Phi - \Omega 2L/c$.

The intensity I_r of the back reflected wave is recorded by a photo detector. Mixing the detector output with an electrical local oscillator at frequency Ω, we obtain in the high finesse approximation $R_1 \approx R_2 \approx 1$

$$I_r(\Omega) \sim E_0^2 J_0(\epsilon) J_1(\epsilon)(1 - R_1) \left(\frac{\mathcal{F}}{\pi}\right)^2 \frac{1}{1 + (2\mathcal{F}\sin(\Phi/2)/\pi)^2} \cos(\phi)\,. \tag{5.12}$$

Here ϕ denotes the phase between the modulation frequency and the local oscillator and

$$\mathcal{F} = \frac{\pi\sqrt{\rho}}{1-\rho} \approx \frac{\pi}{1-\rho} \tag{5.13}$$

is the cavity finesse. This error signal provides a sensitive readout for the intracavity phase, thus it can serve to monitor the oscillator's position. A typical error signal is shown in Fig. 6.14 in the experimental section. Note that in order to treat the motion of the movable mirror quasi-stationary, the cavity decay time $\tau_L = \mathcal{F}L/c\pi$ has to be short in comparison to the oscillator's round trip time $2\pi/\omega_0$. This is achieved by choosing a short cavity length L.

5.3 Position measurements with a Fabry-Perot interferometer

The sensitivity with which the interferometer can detect changes in the mirror's position, is limited by the sensitivity in detection and by the intrinsic displacement uncertainty of the mirror's position. The sensitivity in detection originates from the amplitude and phase fluctuations of the laser probe beam, which for a laser without additional classical noise is given by the shot noise. The mirror's displacement uncertainty has its origin in its thermal motion and in the displacement noise caused by the irregularity of the photon arrival time at the mirror (quantum back action).

To calculate explicitly the amount of each contribution we note, that the average power of a coherent laser beam of frequency ν is given by

$$P = \frac{\langle\, n \,\rangle\, h\nu}{t}\,. \tag{5.14}$$

From the Poissonian distribution of the photon number follows $\langle \Delta^2 n \rangle = \langle n \rangle$ and therefore the spectral density of the shot noise is given by

$$S_{SN} = \frac{\langle \Delta^2 P \rangle}{\Delta f} = \frac{hc}{\lambda} \langle P \rangle , \tag{5.15}$$

where $\Delta f = 1/t$. A more detailed calculation for FM measurements [164] results in

$$\Delta x_{SN}^2 = \frac{S_{SN}}{\tau} = \frac{\lambda hc}{4\eta P \mathcal{F}^2 \tau} \frac{(J_0(\epsilon)\alpha)^2 + 2J_1(\epsilon)^2}{4(R_1 - \alpha)^2 J_0^2(\epsilon) J_1^2(\epsilon)} , \tag{5.16}$$

where η is the quantum efficiency of the photodetector and the parameter α is given by $\alpha = [\sqrt{R_1} - \sqrt{R_2}(1-A)]/(1-\sqrt{R_1 R_2})$. Expression 5.16 is valid for a measurement time τ longer than the cavity decay time τ_L and perfect mode-match of the laser wave into the resonator. For simplicity, we consider in the following the case of a loss-less input coupler ($A = 0$), perfect impedance matching ($R_1 = R_2$), and high finesse ($R_1 \simeq R_2 \simeq 1$), so that

$$\Delta x_{SN}^2 = \frac{\lambda hc}{8\eta P \mathcal{F}^2 J_0^2(\epsilon)} \Delta f . \tag{5.17}$$

with a measurement bandwidth $\Delta f = 1/\tau$.

The back-action due to radiation pressure fluctuations is described by the momentum uncertainty transferred by the circulating light to the oscillator:

$$\Delta p_{BA} = 2\hbar k \sqrt{\frac{\lambda P J_0^2(\epsilon)\tau}{hc}} \frac{\mathcal{F}}{\pi} . \tag{5.18}$$

Here, $2\hbar k$ is the momentum transfer per photon and the other terms arise from the uncertainty of the number of photons hitting the oscillator mirror. Note the linear dependence on $\mathcal{F}$, which results from the fact that the signal to quantum noise ratio of the intensity of the light circulating within the cavity must be the same as that outside the cavity. From this expression the spectral density of the quantum back action is derived to be

$$S_{BA}(\omega) = \chi^2(\omega) 4 \frac{\hbar k}{c} P J_0^2(\epsilon) \left(\frac{\mathcal{F}}{\pi}\right)^2 , \tag{5.19}$$

where $\chi(\omega)$ is the mechanical susceptibility defined in Eq. 5.4. Integrating over the whole resonance gives the expected displacement

$$\Delta x_{BA}^2 = \frac{1}{2\pi} \int_0^\infty S_{BA} \, \mathrm{d}\omega = \frac{Q}{\omega_0^3 m^2} \frac{\hbar k}{c} P J_0^2(\epsilon) \left(\frac{\mathcal{F}}{\pi}\right)^2 , \tag{5.20}$$

where we used Eq. 5.7. The inclusion of classical noise of the laser in these equations which leads to back action effects as well (see next section) can be found in [246].

Finally, the spectral density of the displacement of the mass due to thermal excitation is given by

$$S_{TH}(\omega) = \frac{4 k_B T m \omega_0}{Q} \chi^2(\omega), \tag{5.21}$$

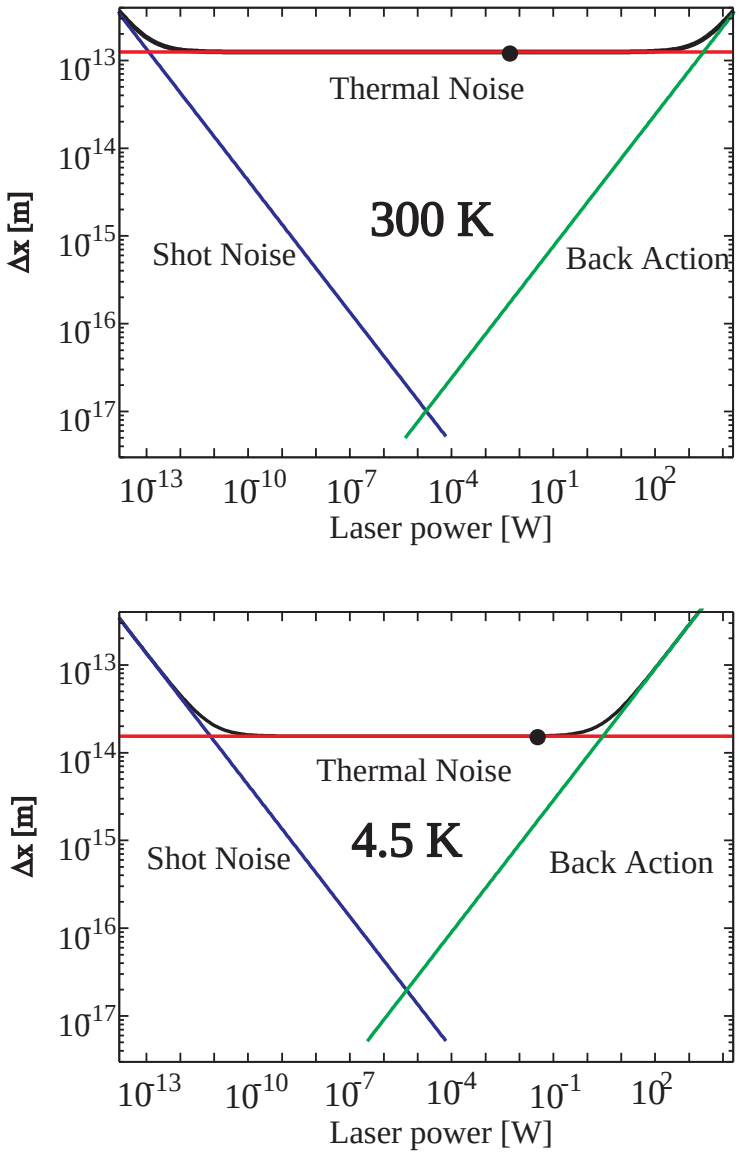

Figure 5.2: *The three contributions to the total displacement noise Δx at the oscillator's resonance frequency ω_0 and their sum in dependence of the optical input power. For lower temperatures the thermal noise decreases considerably. The shift of the back action contribution to lower laser powers is due to the higher mechanical Q-value at 4.5 K. The parameters used for the two graphs are listed in the text. As in the experiment, the measurement bandwidth is assumed to be large compared to the bandwidth of the oscillator's resonance. The two black dots correspond to measurements explained in Sec. 6.5.1.*

resulting in an expected displacement

$$\Delta x_{TH}^2 = \frac{1}{2\pi}\int_0^\infty S_{TH}\,\mathrm{d}\omega = \frac{k_B T}{m\omega_0^2}\,. \tag{5.22}$$

This is the same result as the one, that would be obtained by the equipartition theorem: The probability to measure the amplitude x of a harmonic oscillator subject to thermal noise is given by

$$P(x) \simeq \exp\left(-\frac{m\omega_0^2\langle x\rangle^2}{2\,k_B T}\right)\,. \tag{5.23}$$

Thus the uncertainty of the oscillator's amplitude is equal to the variance of this Gaussian, resulting in Eq. 5.22. For the influence of the finite measurement time see Sec. 6.5.1.
The overall displacement noise consists of the sum of these three contributions

$$\Delta x_{TOTAL} = \Delta x_{SN} + \Delta x_{BA} + \Delta x_{TH}\,. \tag{5.24}$$

For a derivation of this equation directly from the quantum Langevin equations of the complete coupled optomechanical system see [246]. Note that correlations between detection shot noise and back action noise do not play a role in our scheme, since the relevant photo detection shot noise is the one at the FM frequency in the RF range, far away from the kHz range where the back action takes place.

Two plots of this expression, one at $T = 300\,\mathrm{K}$ and one at $T = 4.5\,\mathrm{K}$ are shown in Fig. 5.2 for the experimental values $\mathcal{F} = 15\,000$, $\omega_0 = 2\pi \cdot 2.6 \cdot 10^4\,\mathrm{s}^{-1}$, $m = 10^{-5}\,\mathrm{kg}$, $k = 2\pi/\lambda = 5.9 \cdot 10^6\,\mathrm{m}^{-1}$, $\eta = 70\,\%$, $J_0(\epsilon) = 2/3$, and $\Delta f = 4\mathrm{Hz}$. The main difference between the two plots is that the operation at cryogenic temperatures leads to a reduction of the thermal noise level Δx_{TH} and an increase in the mechanical Q-value: $Q(T = 300\mathrm{K}) = 2 \cdot 10^5$, $Q(T = 4.5\mathrm{K}) = 2 \cdot 10^6$ (see Sec. 6.1.3).

Both figures show that the point of the SQL, where shot noise and back action limited sensitivity meet (the crossing of the two straight lines) is concealed by the oscillator's thermal noise. For the experimental values from above at cryogenic temperatures we get a value of $\Delta x_{SQL} = 2 \cdot 10^{-17}\,\mathrm{m}$ at a power of $4 \cdot 10^{-6}\,\mathrm{W}$. Note that this value is not a true quantum mechanical limit, since it is dependent on the measurement bandwidth. For estimates of the real SQL spectral densities instead of displacement variances have to be used. However, since experimental spectral measurements were limited so far to relatively large bandwidths and since the ratio thermal noise/back action is independent of the bandwidth, the here presented theoretical figures are more useful for a comparison with the experiment.

For the plot at 4.5 K it can be seen that thermal noise and back-action noise become equal at laser powers of 3 W. With improvements of the Finesse values by a factor of 10, this borderline to the back action regime would move to the experimentally accessible 30 mW.

A different approach to investigate the power dependence of the interferometer's sensitivity is, to adjust the measurement time in dependence of the input power, in order to maximize the sensitivity. With such a scheme the SQL becomes directly apparent when using measurement times short to the mirror oscillator's decay time [245]. The same is

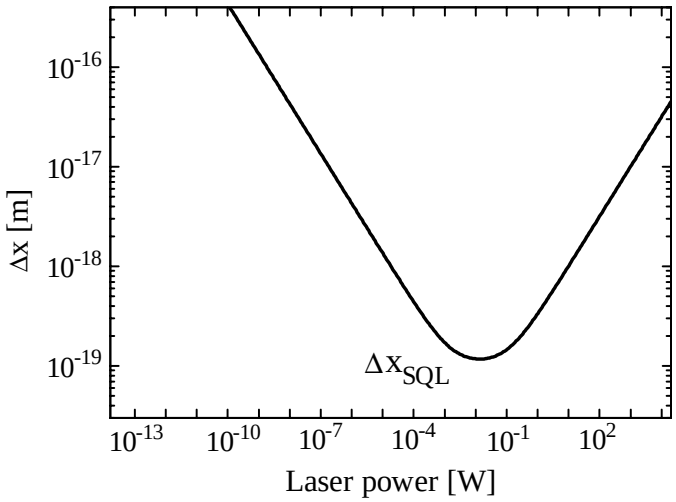

Figure 5.3: *Sensitivity of the interferometer for off-resonance detection. The parameters at $T = 4.5\,K$ are the same as before, except for the finesse which was assumed to be 150 000. The SQL can be reached at laser powers in the mW range.*

true for the (not yet experimentally accessible) detection at frequencies away from the oscillator's resonance frequency. Due to the high Q-factor thermal noise is greatly supressed, but of course the responsivity of the oscillator is much smaller as well. For the experimental parameters at 4.5 K given above, using a susceptibility $\chi(0)^2 = 1/m^2\omega_0^4$, we get a value of $\Delta x_{SQL} = 1 \cdot 10^{-19}$ m at an input power of 2 W. For the improved Finesse of $\mathcal{F} = 150\,000$ the numerical value of Δx_{SQL} remains the same, but the laser power at which it is reached changes to the moderate value of 10 mW (Fig. 5.3).

5.4 Radiation pressure effects

Although all interactions between the moving mirror and the light field have the same basic physical origin, the recoil of the reflected single photon, it is helpful for an understanding of physical effects and for having a defined nomenclature in further descriptions of the experiment, to distinguish between several effects of this opto-mechanical interaction. These effects are not unrelated to or even may include each other.

5.4.1 List of possibly occurring effects

a) quantum back action
b) squeezing of the light field due to the interaction with the moving mirror.
c) classical back action,
d) optical excitation of the oscillator at resonance,
e) DC radiation pressure effects and optical bistability,
f) back action caused by periodic radiation pressure changes due the oscillator's motion,
g) back action caused by periodic changes in the cavity modematching,
h) classical back action due to frequency noise of the laser,
i) radiation pressure damping,

The issue of photothermal excitation is addressed in section 6.5.2. The effects in detail:

(a) has been described above.

(b) is a direct consequence of (a): If the mirror oscillator responds to the intensity fluctuations of the light wave, then conversely these fluctuations are influenced by the mirror motion and are in the ideal case smoothed out below the shot noise limit [88, 63, 148, 261, 86].

(c) is the counterpart of (a) in the classical domain: If the laser wave carries in addition to its coherent state quantum noise classical intensity fluctuations, the stochastic force driving the mirror will be larger, so the back action will be detectable for light powers lower than those needed in (a).

(d) is in principle the same as (c), only that here the laser's intensity fluctuations are not random, but due to an amplitude modulation at the mirror's resonance frequency.

(e) is just the classical radiation pressure due to the mean electric field of the laser wave. It leads to a cavity lengthening due to the circulating light power. The bistable response of the cavity in dependence of the input laser power or the laser frequency described in [58, 157, 75] is a direct consequence of this effect, since the DC radiation pressure makes the cavity length and thereby the cavity detuning intensity dependent.

(f) is an important classical radiation pressure effect, which may lead to opto-mechanical feedback: Due to the mirror's motion and the cavity detuning thus caused, the laser wave's mean field amplitude inside the resonator and accordingly the radiation pressure changes in phase with the oscillator's movement. This leads to a power dependent excitation or damping of the oscillator's motion.

(g) is similar to (f), only that here the change in the circulating laser power is due to the modematching of the laser wave into the resonator. Since the torsional motion of the oscillator leads to an angular modemismatch, again a DC radiation pressure change in phase with the oscillator's movement occurs.

(h) is due to the classical frequency noise of the laser, which is transformed by the detuning relative to the cavity resonance into an amplitude fluctuation inside the resonator.

(i) is a somewhat exotic effect, to be calculated relativistically. It was first pointed out by Braginsky [22] and recently reanalyzed in [153]: If a mirror moves in the same direction as the incident light wave, the flux of the incident photons decreases because of the increase of the light path (reverse for a mirror moving in the opposite direction). This causes an effective damping of the mirror motion, since the force of the light pressure depends on the mirror's velocity.

It should be noted that only (e)-(i) are dependent on fact that an optical resonator is employed in the experiment. For all other effects, the resonator is merely an instrument to gain sufficiently high light power.

5.4.2 Estimation of influence of the effects

(a) is the primary goal of the setup, see also Sec. 6.7 for efforts of other groups.

(b) would a stringent way of proving quantum back action, when (a) has been detected for example by power dependence measurements. The setup would only require a homodyne system for the light back-reflected from the moving mirror cavity.

(c) According to [246] the influence of classical noise inside the resonator on the moving mirror is the same as the shot noise. Since the scaling of classical noise outside of the cavity goes with the power P instead of $\sqrt{P}$ as for the shot noise, we have the curious fact, that taking half the finesse and four times the input power, yields a smaller classical back action whereas the quantum back action remains unchanged. Amplitude noise measurements of the laser have been described in the first part of this thesis, Sec. 3.1.1. For measurements at the frequencies of interest (20-30 kHz) only slight changes of the detection system are necessary. For powers of 10 mW typical values of 20 dB excess noise of the laser with respect to shot noise were measured at 20 kHz. Thus classical back action should be $\approx$100 times stronger at $P = 10$ mW than quantum back action.

In the long run the influence of classical noise on the mirror motion should be prevented. This can be done by implementing an intensity stabilization of the laser. Noise reductions close to the shot noise level at low frequencies have been achieved [250] (see also [35]). On the other hand, the presence of technical intensity noise may be used in a first step to demonstrate the possibility to observe opto-mechanical back action effects in an experiment.

(d) has been observed in our experiment quite easily even at room temperature, which shows that in principle the detection of radiation pressure effects is experimentally feasible with the present setup. Some remarks about possibly involved thermal effects are noted in Sec. 6.5.2. For excitation of micromechanical sensors by modulated laser beams see also Sec. 6.6.2.

(e) has been described for example in [152, 44]. The corresponding optical bistability has been demonstrated beautifully in [58] and [75]. Both do not play a major role in our experiment, since our oscillator mirror responds mechanically only in a narrow band around its resonance frequency and not at 0 Hz DC. It has, however, important side effects when the mean electric field amplitude is influenced by the oscillator's motion (see (g),(h)).

(f) is an effect strongly dependent of the linewidth of the cavity: The expected displacements of the oscillator of $\Delta x \approx 10^{-14}$ m cause a frequency shift of $\Delta\nu = 2\,\Delta x\,\mathrm{FSR}/\lambda \approx$ 660 Hz. With a present linewidth of 1 MHz this results in power fluctuations of $\Delta P \approx$

$4 \cdot 10^{-7} \cdot P_c$, where P_c is the circulating intracavity power.

It was clearly observed in our experiment that the excitation of the mechanical oscillator by a piezoelectric transducer to displacements one or two orders of magnitude above the one of its thermal motion does in fact lead to classical feedback effects with the circulating light wave. At room temperature a damping and enhancing of the oscillator's movement in dependence of the injected light power was observed. This made decay time measurements of the mechanical oscillation via the error signal very imprecise. These effects, dependent on the relative detuning between cavity and laser frequency, were difficult to quantify. (It has to be noted that feedback effects due to laser detuning by the employed locking circuit may have had an influence as well, since for large detunings the feedback signal around 26 kHz could not be completely eliminated.) Similar effects have been observed and made use of in setups employing microoscillators. For strong light powers and non-zero detuning even self-oscillation has been observed (c.f. Sec. 6.6.2, see also chapt. 1.3 of Ref. [23]).

In principle for a stabilization exactly on resonance, not an ω_0-dependence of the generated amplitude modulation of the intracavity field arises, but a $2\omega_0$-dependence, which provides no direct feedback to the oscillator's motion. Such a stabilization however is difficult to achieve with a moving mirror cavity and maybe in this case parametric effects as the ones described in Sec. 6.1.5 have to be taken into account. For clarification, note that for the intended interferometric measurement method it is crucial that at the measurement frequency, which is equal to the oscillator's resonance frequency ω_0, the laser frequency does not follow the cavity length changes. Thus the power fluctuations outlined here form an intrinsic part of the system and are not compensatable via feedback.

For the planned improved finesse, these effects become stronger, since the relative power fluctuations scale quadratically with the finesse, due to the cavity resonance's Lorentzian line shape. For high finesse values we can approximate the cavity resonance by $f(\delta) = 1/(\delta^2 + a^2) \approx 1/a^2 - \delta^2/a^4$ where $\delta = 2\Delta x \cdot \mathrm{FSR}/\lambda$ is the detuning for a cavity length change Δx and $a = \mathrm{FSR}/2\mathcal{F}$ is half the linewidth. Thus expected displacements $\Delta x \approx 10^{-14}\,\mathrm{m}$ and improvements of the finesse by a factor of 10 lead to non-negligible fluctuations

$$\Delta P = \left(1 - \frac{f(\delta)}{f(0)}\right) P_c \approx \frac{\delta^2}{a^2} P_c = \left(\frac{4\Delta x\, \mathcal{F}}{\lambda}\right)^2 P_c \approx 4 \cdot 10^{-5} \cdot P_c\,. \tag{5.25}$$

To set these power fluctuations in relation to the shot noise we note that the relation of circulating to incident power is $P_c/P \approx (1 - R_1)\mathcal{F}/(1 - \sqrt{\rho})\pi \approx \mathcal{F}/\pi$. Thus $\Delta P \approx (4\Delta x/\lambda)^2/\pi\mathcal{F}^3\, P \approx 1 \cdot 10^{-15}\, \mathcal{F}^3\, P$. In comparison, the intracavity shot noise fluctuations per unit bandwidth Δf can be approximated by $\Delta P/\sqrt{\Delta f} \approx \sqrt{hc/\lambda} \cdot \mathcal{F}/\pi \cdot \sqrt{P}$, which results in power fluctuations of $\Delta P \approx 1 \cdot 10^{-11} \sqrt{W}\, \mathcal{F} \sqrt{P}$ within the bandwidth of the oscillator $\Delta f \approx 10^{-2}$ Hz. For incident powers P in the mW range this is less than the estimated classical fluctuations, already for moderate finesse values.

The reason why this problem usually does not appear in theoretical calculations regarding quantum effects optomechanical systems is, that the parameter of the cavity detuning is usually cancelled in the mean field approximation [175, 63, 246].

(g) is given by the mode overlap of the incoming Gaussian beam $\Psi(x,y,z)$ with the Gaussian beam inside the resonator $\Psi_\theta = \Psi(x_\theta, y, z_\theta)$, which is rotated by an angle θ due to the oscillator's torsional motion. Here $x_\theta = x - \theta z$ and $z_\theta = \theta x + z$ are the rotated coordinates. The Gaussian beam is given by [122]

$$\Psi(x,y,z) = \frac{1}{w(z)}\sqrt{\frac{2}{\pi}}\exp[-\frac{x^2+y^2}{w(z)^2} - \mathrm{i}\frac{x^2+y^2}{2R(z)^2} - \mathrm{i}kz + \mathrm{i}\mathrm{Arctan}(\frac{z}{z_0})], \tag{5.26}$$

where $w(z) = w_0\sqrt{1+(z/z_0)^2}$ is half the beam's diameter at point z of a beam with waist w_0 and Raleigh range $z_0 = \pi w_0^2/\lambda$. The overlap function is given as the integral over the cavity volume

$$I(\theta) = \frac{1}{L_z}\mathrm{Re}\int\int\int \Psi\Psi_\theta^* \, dxdydz, \tag{5.27}$$

where L_z is the cavity length. Approximating for small angles and a short cavity gives

$$I(\theta) \approx \mathrm{Re}\int \mathrm{e}^{-\frac{x^2}{w_0^2} - \mathrm{i}kz} dx \approx 1 - \frac{\theta^2 k^2 w_0^2}{8}, \tag{5.28}$$

With a distance $d = 1\,\mathrm{mm}$ of the laser beam from the torsional axis, the torsion angle for a displacement $\Delta x = 2\cdot 10^{-14}\,\mathrm{m}$ is given by $\theta = \mathrm{Arctan}(\Delta x/d) \approx 2\cdot 10^{-11}\,\mathrm{rad}$. This results in power fluctuations $\Delta P \sim 1 - I(\theta)^2 \approx 10^{-17} P_c$. These are negligible compared to the ones estimated in (f).

(h) The frequency noise of the laser is expected to be about $S_{FN} = 1\,\mathrm{Hz}^2/\mathrm{Hz}$ around ω_0 [45]. Integrated over the width of the resonance of the mechanical oscillator $\Delta\nu_0 \approx 0.013\,\mathrm{Hz}$ gives a frequency uncertainty of $\Delta\nu = 1\,\mathrm{Hz}^2/\mathrm{Hz}\cdot\Delta\nu_0\,\pi/2 = 0.014\,\mathrm{Hz}$, which is small compared to the frequency fluctuations introduced by the oscillator's motion (g).

Nevertheless this noise source must not be neglected, since it disturbs the shot noise limited detection at frequencies away from the oscillator's resonance. A reduction of the laser frequency noise to $10^{-3}\mathrm{Hz}^2/\mathrm{Hz}$ by means of a high finesse reference cavity has been demonstrated [19]. In our case, a combination of such an active frequency noise reduction and an increase of the FSR of the sensor cavity can be used.

(i) The effect of "radiative friction" is described in [153]: With the values of our experiment, the damping factor of the mechanical oscillation $\delta_{RF} = P/(mc^2\mathcal{F}^2) \approx 2\cdot 10^{-4}s^{-1}$ (corresponding decay time $1/\delta_{RF}$) is presently 2 orders of magnitude smaller than one that would be detectable with our oscillators which have decay times in the range of 20-50 s. However, an improvement of the finesse by one order of magnitude would bring this effect into the realm of measurability.

6 Experiment II: Interferometric position measurements

6.1 The mechanical oscillator

6.1.1 Basic description

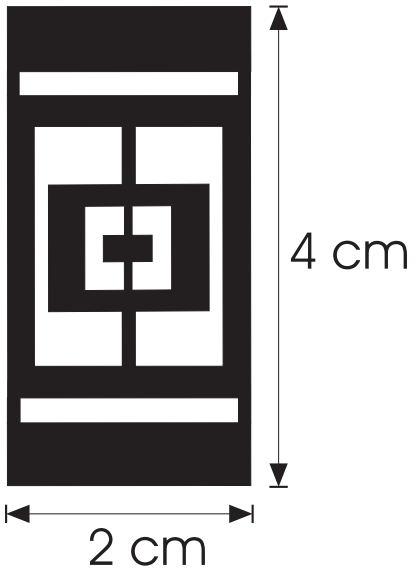

Figure 6.1: *Silicon torsional oscillator employed as the moving mirror in the experiment.*

In our experiment, the movable mirror is a silicon torsional oscillator. The devices employed in the experiment were manufactured at the Institute of Microtechnology, Neuchâtel in collaboration with N. Blanc, and N.F. de Rooij and by E. Steinsland at the company Sintef, Oslo. Micromachined oscillators of this kind have already found use in condensed matter studies [118, 119, 158, 270]. A general overview about the techniques of silicon micromachining is given in [55]. Our oscillator has been fabricated the following way: A thick oxide layer was thermally grown on both sides of a highly polished commercial p-type 5Ω/cm silicon wafer with $< 100 >$ orientation. The oscillator was defined by double sided lithography and the structure was etched free in a 60°C KOH solution. The size of the whole structure is $4\,\mathrm{cm} \times 2\,\mathrm{cm}$. The design and room temperature properties are reported in [37]: It is made up of two coupled oscillators consisting of an inner frame and a vane connected by two torsion bars. The oscillator has a symmetric and an antisymmetric mode. Only the antisymmetric mode has a high Q resonance due to low stress concentrations in the beams connecting the two coupled oscillators to the frame. Fig. 6.2 left shows this vane-frame torsional oscillation with an exaggerated amplitude.

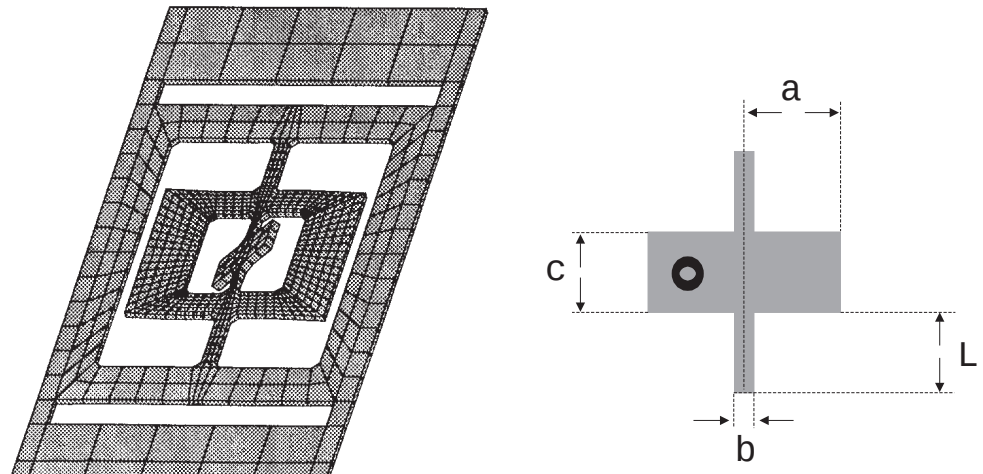

Figure 6.2: *Left: Vane-frame torsional oscillation (exaggerated amplitude) generated by an FEM-simulation. The point off-axis where the laser beam is reflected from the coated inner vane in the cavity setup is depicted in the sketch on the right side.*

The geometry of the vane is shown in Fig. 6.2 right, with the corresponding proportions listed in the following table:

a [mm]	**b** [mm]	**c** [mm]	**L** [mm]	**h** [mm]	Θ_0 [kgm^2]	J_t [m^4]
2	0.39	2	2.2	0.39/0.29	$9.6 \cdot 10^{-12}$	$3.3 \cdot 10^{-15}$

The resonance frequency ν_0 and the oscillator's effective mass m can be obtained from these data by the equation of motion (without damping)

$$\Theta\ddot{\phi} = -M = -\frac{2J_tG}{L}\,\phi, \tag{6.1}$$

where M is the torque, G the shear modulus in the appropriate crytallographic orientation and J_t the static torsional moment of inertia of the bar. The factor 2 comes from the fact, that the vane is held by two bars. Comparing with Eq. 5.1 we see that $2J_tG/L$ plays the role of the spring constant for the torsional motion. Writing the equation as

$$\ddot{\phi} + \omega_0^2\,\phi = 0, \tag{6.2}$$

we get

$$\nu_0 = \frac{1}{2\pi}\omega_0 = \frac{1}{2\pi}\sqrt{\frac{2J_tG}{\Theta L}}. \tag{6.3}$$

The total moment of inertia Θ is given by the moment of inertia of the vane $\Theta_v = 2\rho cha^3/3$ plus a small correction term of the moment of inertia of the moving part of the torsion bar $\Theta_b = \rho bh(b^2+h^2)/12$. The correction term can be estimated according to [239](p.344) by assuming that the rotation angle of the bar is fixed at one end and at the

other end is equal to that of the vane. Integration over the whole bar and taking into account that there are two of them that hold the vane yields $\Theta = \Theta_v + 2\Theta_b/3$. Note that Θ_b is usually 2 orders of magnitude smaller than Θ_v.

The static torsional moment of inertia J_t of a single bar with a rectangular cross section has been derived in [238]:

$$J_t = \frac{hb^3}{3}\eta_l, \tag{6.4}$$

where η_l is a numerical factor, depending on the ratio h/b. For $h \approx b$ we have $\eta_l = 0.141$. (Note that for $h \neq b$ always the smaller one of the two values has to be taken to the third power).

For the proportions listed in the table above we calculated and measured resonance frequencies of $\nu_0 \approx 21$ kHz for the oscillators with thickness $h = 290\,\mu$m, and $\nu_0 \approx 26$ kHz for the ones with $h = 390\,\mu$m.

After fabrication of the structure and removal of the oxide, the vane was coated on one side with a high-reflectivity dielectric coating for 1064 nm. Since the torsion bars were protected by a steel mask during the coating run, the 4.3 micron coating of SiO_2/Ta_2O_5 did not cause a substantial change in the mechanical properties of the oscillator. The higher mass of the coated vane led to a slight decrease of the resonance frequencies (see also [182, 270]).

As shown in Fig. 6.2, when the oscillator is part of the optical cavity the laser beam is reflected at a distance d from the torsional axis, so that the torsional motion leads to a cavity length change. The effective mass m in the expressions of Eq. 5.1 is for a torsional oscillator given by Θ/d^2. With a distance d of ≈ 1 mm this leads to $m \approx 10$ mg.

6.1.2 Fastening of the oscillator

Since any contact of the oscillator to the external world contributes to its energy dissipation, fastening the oscillator without introducing mechanical losses is a crucial task in our experiment. In the first series of measurements the oscillator was clamped by a gilded tip pressed by a spring onto the center of one of the two large areas at the head or the bottom of the oscillator. Since this fastening method did not yield a completely stable position of the oscillator in cavity measurements and especially led to problems during the cool down periods in the cryostat, it is now only used for testing new oscillators.

The most promising method of mounting the oscillator is until now the following: The oscillator is glued by stycast epoxy onto an Invar holder at four small spots situated at its four corners. Since both silicon and Invar have very small temperature expansion coefficients ($\Delta L/L$ from 300 K to 4 K Si: ≈ 0.03 [130], Invar: 0.05 [183]), this mounting does not introduce too much strain onto the oscillator when cooled down to 4 K. It has the big advantage that the cavity setup remains in a fixed position even during drastic temperature changes. Furthermore, the bending motion of the oscillator (≈ 2 kHz) which makes cavity stabilizations very difficult, is largely suppressed. For changings in the setup, the oscillator can be released from the Invar holder by application of formic acid. The finesse of the mirror coatings did not degrade by such a treatment.

6.1.3 Measurement of the quality factor

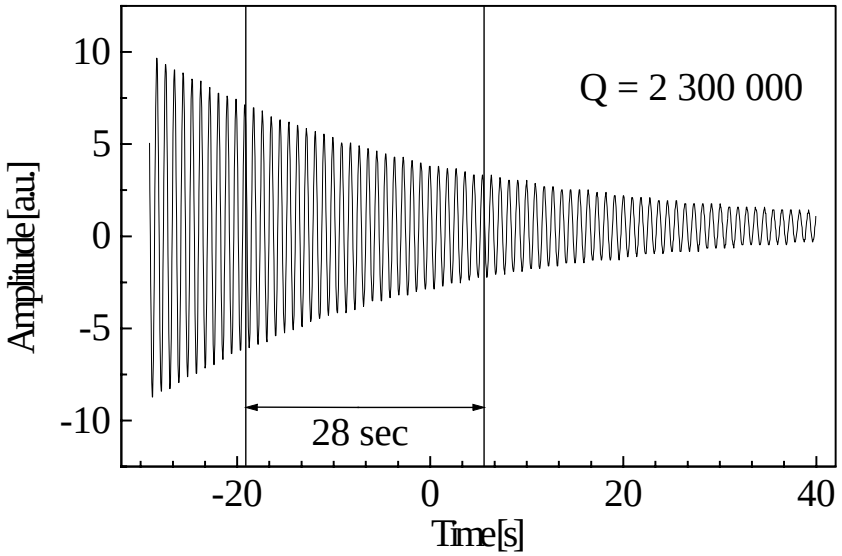

Figure 6.3: *Typical decay time measurement at cryogenic temperatures. After the excitation via a piezoelectric transducer is switched off, the oscillator rings down in* $\approx$ *100 s. The oscillation frequency shown is the beat frequency between the natural oscillation at* ω_0 *and the detection frequency of the lock-in amplifier.*

Mechanical damping depends both on gas pressure and temperature. Best values are obtained in vacuum and at low temperatures, but usually still depend on clamping loss. Physical limits for highest obtainable Q-values are given in [24]. A general overview of effects responsible for internal friction is given in [67] and chapt. 2 of Ref. [24]. Thermoelastic internal friction is discussed in [203].

To characterize the properties of our oscillator, a simple optical setup was used. The oscillator is clamped to a mount attached to a piezoelectric transducer in a cryostat vacuum chamber. A diode laser is shined on the torsional vane and the reflected light is detected with a segmented photodiode, which gives a signal proportional to the angular displacement of the torsional oscillator. The oscillator is mechanically excited at resonance. After the excitation is turned off, the amplitude decay is measured using a lock-in amplifier as a demodulator with a slightly detuned reference frequency. A typical measurement is shown in Fig. 6.3. The curve's envelope is fitted by a single exponential.

Another method of determining the Q-value is the measurement of its linewidth. The setup is the same as before and the excitation frequency is gradually increased via computer control, while the oscillator's amplitude response is recorded. Typical measurements are shown in section 6.1.6 for microoscillators. For medium decay times (room temperature) both methods gave comparable results, for long decay times (cryogenic temperatures) the ring down measurements were more accurate, for very short decay times (microoscillators) scanning the linewidth worked best. A third method for determining the oscillator's Q-value is the measurement of its linewidth via the Fabry-Perot interferometer, described in section 6.5.

The pressure dependence of the oscillator's Q-factor has been described in [37]. It was found that for a pressure $< 10^{-2}$ mbar the friction due to the gas molecules of the

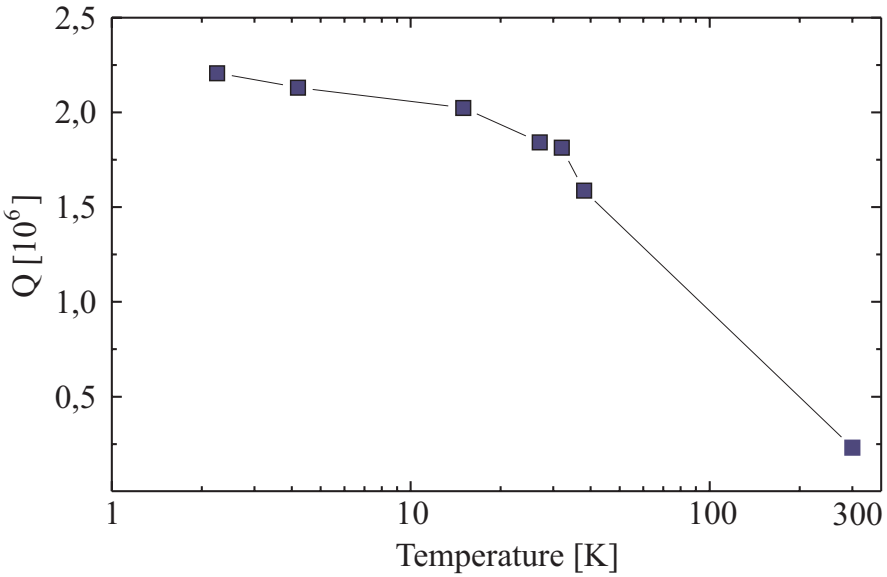

Figure 6.4: *Temperature dependence of the quality factor.*

environment is negligible. It is interesting to note that the pressure dependence for the microoscillators of the same design presented in section 6.1.6 is almost the same, despite the scaling factor of 20.

As for the temperature dependence, the quality factor increased from $\approx$ 200 000 at room temperature to >2 000 000 at 4 K due to a reduction in phonon scattering. Fig. 6.4 shows the Q-factor of a coated oscillator in the temperature range 300 K - 2 K. In the same temperature range the resonance frequency increases by about 100 Hz, due to changes in the elastic constants.

The Q-factor measurements presented here are still one order of magnitude lower than the presently best ones for macroscopic silicon torsional oscillators [118, 270]. This has or may have five reasons: (i) better fastening methods, (ii) Si-material (low n-doping), (iii) different etching techniques, (iv) slightly different design, and (v) measurements at temperatures <1 K. The first three points will be further investigated in the future development of the experiment, design changes are discussed in section 6.1.4, the operation at lower temperatures is presently not possible in our experiment, due to the employed cryostat.

Comparable or higher Q-values for mechanical oscillators besides torsional oscillators have only been observed for bulk-oscillations [155] or pendulum modes [24, 249]. The application of either of them would require a different design of the experiment leading to difficulties outlined in section 6.7.

As a conclusion, the Q-values achieved so far should be high enough to reach the goals outlined in the previous chapter with the present experiment. Yet improvements by an order of magnitude may still be possible.

6.1.4 Possible changes in the oscillator design

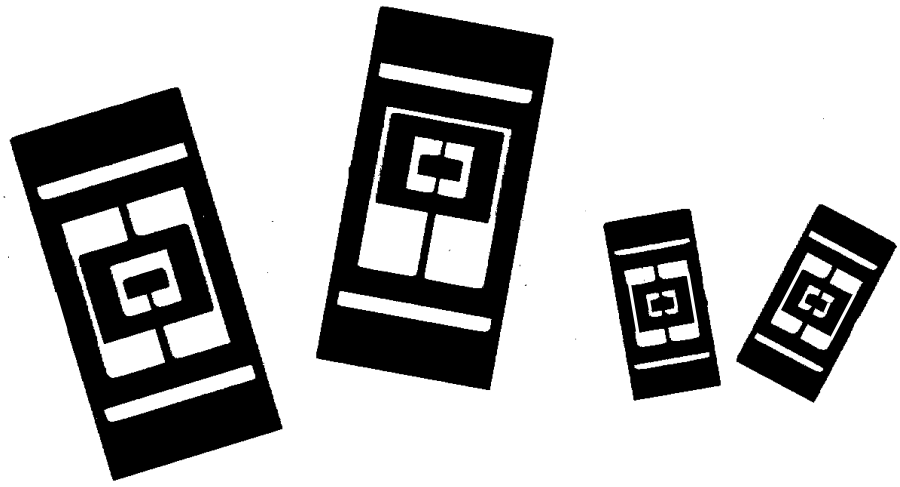

Figure 6.5: *Lasercut oscillators of different designs. Left design: Vane held by only one bar to reduce the internal friction and to lower the resonance frequency, middle: stretched bar of decoupling frame for better isolation from the clamping area, right: test of scaling properties.*

A look at the ratio between thermal noise and quantum back action

$$\frac{x_{\mathrm{BA}}^2}{x_{\mathrm{TH}}^2} = \frac{Q}{\omega_0 m^2}\frac{1}{k_B T}\frac{\hbar k}{c}\left(\frac{F}{\pi}\right)^2 P_0 \tag{6.5}$$

shows which features of the mechanical oscillator are important: Low mass, high Q, low frequency. Since in these formulas the effective mass does not only depend on the oscillator's weight, but also on the distance d of the laser beam from the torsional axis, hardly anything is gained by a simple scaling of the oscillator's size which would also make high-finesse coatings and cavity alignment more difficult. Furthermore, to keep the optical losses due to finite size effects of the mirror below 0.5 ppm, the distance between the center of the laser beam to the edge of the high reflection coating should exceed 5 times the beam waist, which shows that for realistic waists of $100\,\mu$ the scaling of the vane's side c can't be reduced by much. Only the oscillator's thickness should be kept as small as possible. Technical limits for superpolished Si-wafers are 250-300 μ (Crystec, Berlin).

The highest mechanical Q-factor for silicon torsional oscillators has been achieved with a structure similar to the here employed Buser-design [118, 270], with the most important difference that vane and decoupling frame are held only at one side by a single bar. The advantage is a reduction of the internal friction and losses due to surface effects and a lowering of the resonance frequency. Furthermore, lengthening the bar of the decoupling frame leads to a better isolation of the whole oscillator from the environment (reduced clamping losses) [271]. Both changes in the design, however, have the disadvantage, that the bending motion of the oscillator is enhanced. Thus laser frequency stabilization to the cavity length in the setup of the interferometer will be more difficult. As a test, different oscillators designed by AUTOCAD were fabricated via laser cutting by a local company

and by the Fraunhofer Institut für Lasertechnik in Aachen. This also served as a test for alternative production methods that don't involve the lengthy and expensive fabrication of the etching masks.

It turned out that the surface quality of the cut edges is much inferior to that achieved by etching (small bubbles of melted Si, fissures, diffusion of the surface protection coating (hairspray or spin coated photo resist)). No Q-factors >40 000 were obtained, making it difficult to quantitatively evaluate the influence of the geometry on the Q-factor. Fig. 6.5 shows the tested oscillators. The leftmost design was also realized by removing via laser cut one bar of an etched oscillator of Buser-design. With this device, the lowering of the resonance frequency by a factor of $\sqrt{2}$ was demonstrated, while no significant change of the Q-value was observed. As a conclusion, for the near future further experiments with the modified design (Fig. 6.5 left), could be done by the tested combined fabrication method (etching, laser cutting) or by using the existing etching mask with a slight modification. General tests of oscillator designs need fabrication methods more reliable than laser cutting.

6.1.5 Nonlinear mechanical effects

Any real mechanical oscillator driven to high enough amplitudes will exhibit some kind of nonlinear behavior. Since the first half of this thesis deals with nonlinear optical effects, and since nonlinear mechanical effects may change the responsivity of the oscillator and have an influence on decay time measurements, a short investigation is helpful for comparison and for future characterizations of the oscillators. As in the optical domain, the observed effects can be divided into (a) harmonic generation, (b) sub-harmonic generation (parametric effects), and (c) bistable response (third order effects).

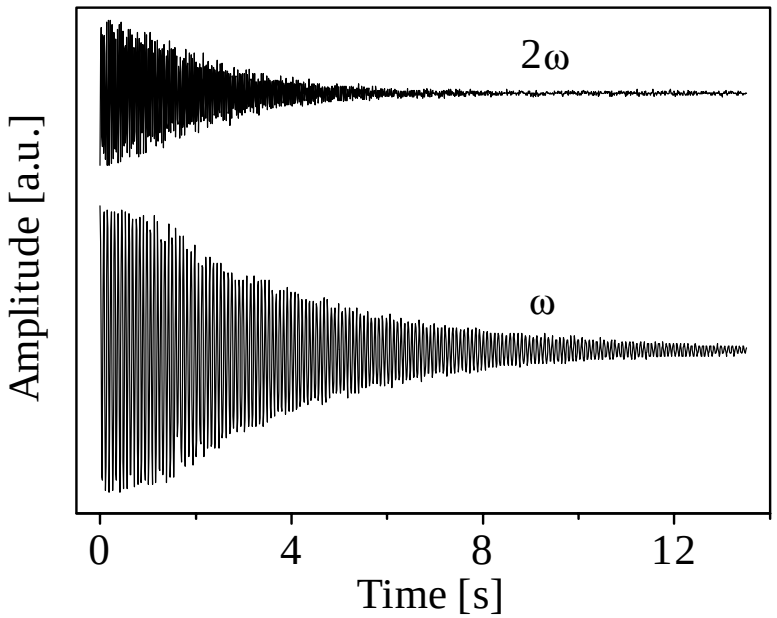

Figure 6.6: *Decay of the oscillator's ω_0 and $2\omega_0$ resonances. The pure exponential decay of the ω_0-oscillation does not start until the $2\omega_0$-oscillation has become small enough.*

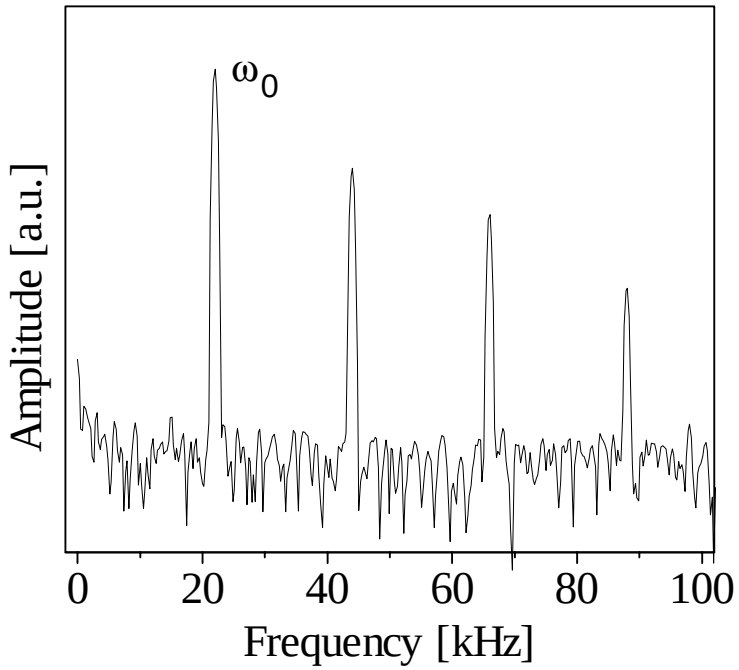

Figure 6.7: *Strong excitation of the oscillator leads to the generation of higher harmonics. Here the first 3 harmonics of the ω_0-oscillation are shown.*

The second harmonic generation is shown in Fig. 6.6 employing the same measuring device as for the Q-measurements in section 6.1.3. For strong enough excitation at the frequency ω_0, the oscillator starts oscillating at $2\omega_0$ as well. When the excitation is switched off, the influence on the decay time can be observed: The energy of the $2\omega_0$-oscillation is transferred to the ω_0-oscillation, leading to a non-exponential decay. Thus much longer decay times for the ω_0-oscillation are measured, leading to an artificial increase of the oscillator's mechanical Q. It is interesting to note, that, although the decay time τ^* of the $2\omega_0$-oscillation is shorter than that of the ω_0-oscillation, the Q-factor, being defined by $\tau^*\pi f$ is higher for the harmonic (330 000) than for the sub-harmonic (230 000).

Not only the second order but still higher harmonics were observed by strong excitation at the frequency ω_0. Fig. 6.7 shows the first four harmonics measured by a spectrum analyzer. With a lock-in detector the 10th harmonic was still detectable. The measurement of the mechanical Q for different overtones has been used as a tool for analyzing the origin of acoustic wave attenuation [62].

Mechanical parametric amplification and deamplification with a corresponding change of the thermal noise characteristics has been beautifully demonstrated in [206]. Effects of this kind are probably not usable to enhance the sensitivity of the interferometer, since damping of the noise floor leads to a damping of the signal as well. Nevertheless they contribute to a better understanding of the oscillator's noise behavior.

In classical mechanics the parametric interaction is described by Mathieu's equation

$$m\ddot{x} + \delta\dot{x} + (k + \lambda\cos(\omega_1))x = F\cos(\omega_0 + \phi). \tag{6.6}$$

If $\omega_1 = 2\omega_0$, a π-periodic phase-dependence of ϕ leads to amplification and deamplifica-

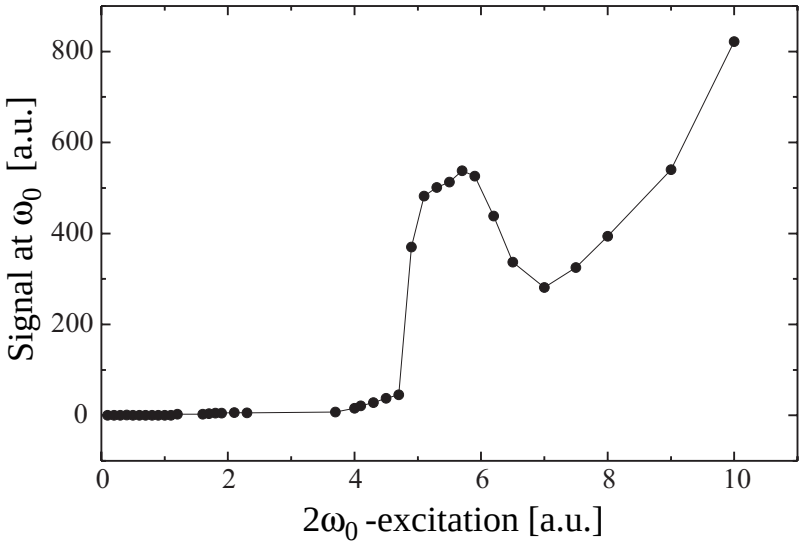

Figure 6.8: *Mechanical parametric oscillation: Starting from a certain power of the $2\omega_0$-pump λ, the subharmonic ω_0 starts oscillating. The dip at higher excitation strengths is due to destructive interference between the ω_0- and $2\omega_0$-oscillation.*

tion of the oscillator's amplitude x. If the input signal F is equal to zero, a parametric oscillation with a certain mechanical threshold λ_0, depending on the oscillator's Q-factor is expected. In our experiment, ω_0-signal input and $2\omega_0$-pump were realized by two piezoelectric transducers, exciting the oscillator mechanically at two different points. Fig. 6.8 shows the parametric oscillation with no signal input, having a well-defined threshold power for a certain pump strength λ. With a weak signal input the phase dependence of the parametric effects was measured as well. The third nonlinear effect, bistable response, was observed only for high-Q cryogenically cooled oscillators. Scanning slowly the excitation frequency, asymmetric line shapes were reproducibly found.

6.1.6 Investigation of microoscillators

We investigated micromechanical Si-structures to test new fabrication technologies, to examine the influence of scaling on the mechanical Q-factor, and also because many experiments on optomechanical coupling have previously been carried out in this area (Refs. see Sec. 6.6.2). Such oscillators are of practical use as pressure sensors, light modulators, accelerometers, tactile, flow, temperature, or radiation sensors (see the reviews [197]). They are also used to approach the investigation of phonon finite-size effects [78], for high precision electrical charge measurements [48], or as magnetometers [2].

The fabrication of the two oscillators presented here was done by Thomas Müller, ETH Zürich/Austria Mikro Systeme, Unterpremstätten. The etching process is described in detail in [162]. By doping and electrochemical etch stop techniques very thin n-well membranes were defined, out of which the structures were etched. The oscillator we investigated first was 4.5 μm thick with an overall size of 1x2 mm. Except for the scaling, the design, shown in Fig. 6.9, is the same as the one from Buser et al. [37]. With the notation of section 6.1 the proportions of the vane are $a = 100\,\mu$m, $c = 100\,\mu$m,

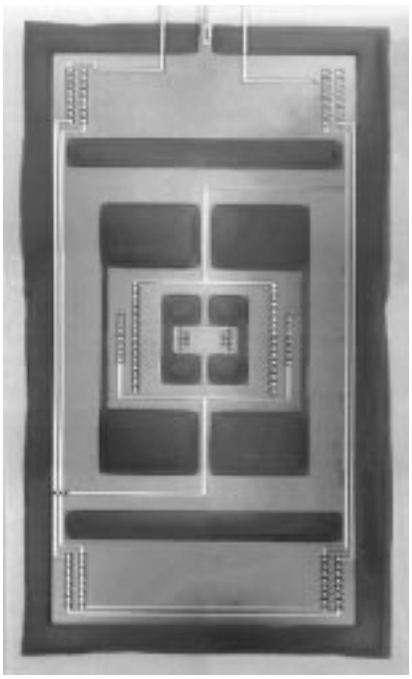

Figure 6.9: *Photograph of the microoscillator. The overall size is 1x2 mm. Traces of the electric contacts necessary for the processing are still visible.*

$b = 20\,\mu$m, $L = 105\,\mu$m. The measurement of the oscillators resonances is done the same way as described in section 6.1.3. Fig. 6.10 shows a typical spectrum. The resonance of the vane can be identified with the peak at 130 kHz. Its frequency is a bit lower than the one theoretically predicted of 144 kHz, due to the "soft" boundary conditions for the torsion bars inside the thin n-well structure, compared to rigid clamping assumed in the analytical model. The Q-value amounted to 27 400. This is of the same order of

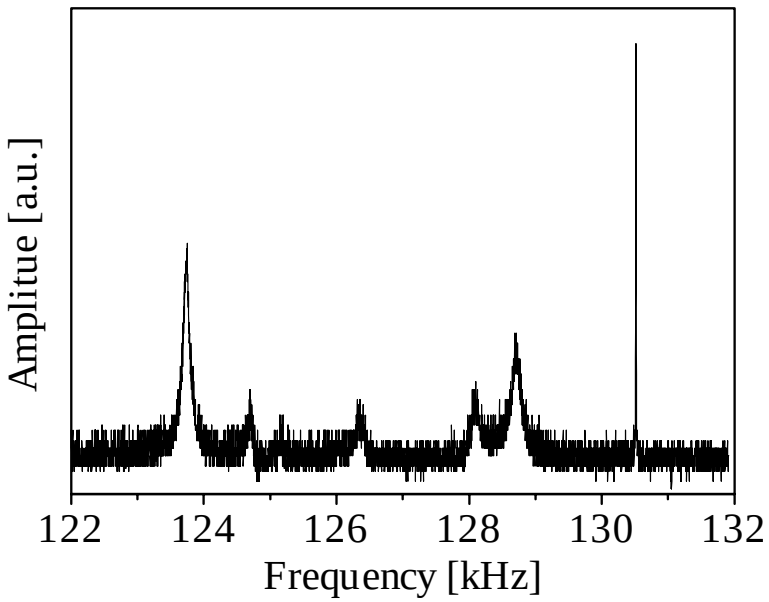

Figure 6.10: *Spectrum of the microoscillator. The sharp narrow resonance at 130.5 kHz is due to the torsional movement of the vane. The Q-value, obtained by measuring the width of the resonance, amounted to 27400.*

magnitude as values achieved with similar structures fabricated at Caltech in Pasadena [194]. Other micromachined torsional Si-oscillators reported earlier [180] showed much lower Q-values.

By reducing the size of the oscillators even more ($a = 45\,\mu$m, $c = 50\,\mu$m, $b = 20\,\mu$m, $L = 32\,\mu$m, $h = 10\,\mu$m), the Q-value degraded. The best resonance at ≈ 2 MHz was fitted with a Q-value of 7300. Though the two microoscillators are not directly comparable since the etching procedure varied, it seems that due to the dominance of surface losses higher Q-values can be more easily achieved with larger structures.

With other designs than the ones reported here, Q-values of $\approx 10^6$ have been measured for Si-oscillators of μm size [78] and Q-values of 20 000 for nanometer scale Si-oscillators with resonance frequencies >70 MHz [47]. This and the prospect of becoming able to fabricate macroscopic mechanical devices with thicknesses of tenths of micron or in the long run even fabricate micromechanical structures that exhibit quantum mechanical behavior should spur further efforts in these investigations.

6.2 Optical coating and cleaning

So far two attempts were made to supply the vanes of the Si-oscillators with high finesse coatings. One was carried out at the Laser Zentrum Hannover (LZH) and one by Research Electro Optics (REO), Boulder. In both cases the oscillators were cleaned directly before the coating. In Hannover we cleaned with lens tissue and ethanol until the oscillators appeared to by dustfree under a microscope. The coating itself consisted of a 4.3 micron layer of SiO_2/Ta_2O_5 (LZH). Apart from employing different masks, so that the coated area was larger in the second run made in Boulder, no significant differences between both coatings were found. The more homogeneous LZH-coatings were used in the measurements presented below.

Since the packaging for the shipping after both coating runs was not optimum, and since the oscillators had to be handled quite much (glueing, aligning) before being placed in the vacuum chamber, we had to investigate cleaning methods. For the fragile oscillator vanes it worked best to rub gently in one direction with lens tissue using as a solvent first acetone and afterwards iso-propanol. For the mirrors a spinning device was employed, using (medical) cotton-wool tips and the same solvents as above. The efficiency of the cleaning was checked by observation of the substrates with a dark field microscope. Although finesse values improved, cleaning methods are still not optimum.

For some of the oscillators it was also necessary to remove scattered coating material from the oscillator's backside. This was successfully done by using a HF-buffer (H_2O, HF 50 %, NH_4F 40 % ratio 40:7:1) after having protected the coated vane with a special photoresist.

The best values we obtained in finesse measurements were 30 000 (employing for the cavity an incoupling mirror with measured reflectivities/losses for a finesse of 60 000). For the cavity used in the actual setup the finesse values were lower since the vane was inhomogeneously coated and the difficult cavity alignment did not always allow finding the spot with the highest finesse. Furthermore the beam position shifted slightly during the cool down period in the cryostat.

Measurements of the single pass transmission of the coated vanes gave transmission losses of $T = \approx 5 \cdot 10^{-5}$. Since finesse measurements indicate total losses of $A+T = 4 \cdot 10^{-4}$, we have to assume that the major loss factor is the scattering on the coated silicon vane. This is confirmed by the low incoupling C of about 10 %, which indicates a scattering loss of $A = \pi(1+\sqrt{1-C})/\mathcal{F} = 4 \cdot 10^{-4}$. The total cavity transmission amounted to $\approx 3 \cdot 10^{-3}$.

6.2.1 Surface quality measurements

To be able to give a more precise estimation of the limiting factor for the obtainable finesse values, we investigated the surface quality of the Si-substrates. A one-parameter description of the surface quality for a specified area is given by the RMS roughness, defined as the height variance of the recorded points of this area: $\Delta h_{rms} = \sqrt{< (h - < h >)^2 >}$. Other important characteristics are the peak-to-valley ratio of the surface structures, and their lateral frequency.

Meaningful surface measurements on superpolished substrates are not done easily, they should cover an area comparable to the employed beam waist (100 μm) and should have sub-Angstrom vertical resolution. We employed four different instruments to obtain surface data:
1) An AFM, here in Konstanz,
2) a ZYGO Maxim 3D at the MPI in Mainz,
3) Total Integrated Scattering (TIS) measurements of the Fraunhofer institute in Jena,
4) a Micromap Phase-shift Mirau Micro-Interferometer in Boulder.

The AFM measurements were done on areas in the μm regime. RMS values < 10 Å were obtained (coated segments slightly higher). This is in agreement with the values specified by commercial Si-polishers for unprocessed wafers. AFM measurements of the company Crystec, Berlin showed typical values of 3 Å. The ZYGO measurements resulted in RMS values of 10-20 Å for areas of 60x80 μm and 20-30 Å for areas of 600x800 μm. No difference was found between processed and unprocessed wafers. The validity of these measurements is limited though, since a superpolished Si-wafer, comparable to the probes, was used for the calibration of the instrument. The TIS-measurements were not yet ready at the time of finishing this thesis.

The Micromap measurements are perhaps the most informative and reliable ones. Fig. 6.11 shows the image of an uncoated vane of a Si-oscillator in comparison with that of a quartz substrate. As can be seen, the most dominant structures have lateral extensions of $\approx 30\,\mu$m and the RMS roughness of 4 Å is one order of magnitude larger than that for the quartz substrate. We estimate that this is the dominant loss mechanism so far.

The relation between RMS roughness and cavity losses due to surface scattering is given by

$$\rho_S = \left(\frac{4\pi \Delta h_{rms}}{\lambda} \right)^2 . \tag{6.7}$$

Thus given the measurements of this section, scattering losses of $\rho_S = 2.5 \cdot 10^{-5}$ result in a limiting value for the finesse of $\mathcal{F} < 240\,000$.

In conclusion it should be said that, although the provided coatings with finesse values of 10 000-30 000 have not met our expectations so far, it is, to my knowledge, the first time

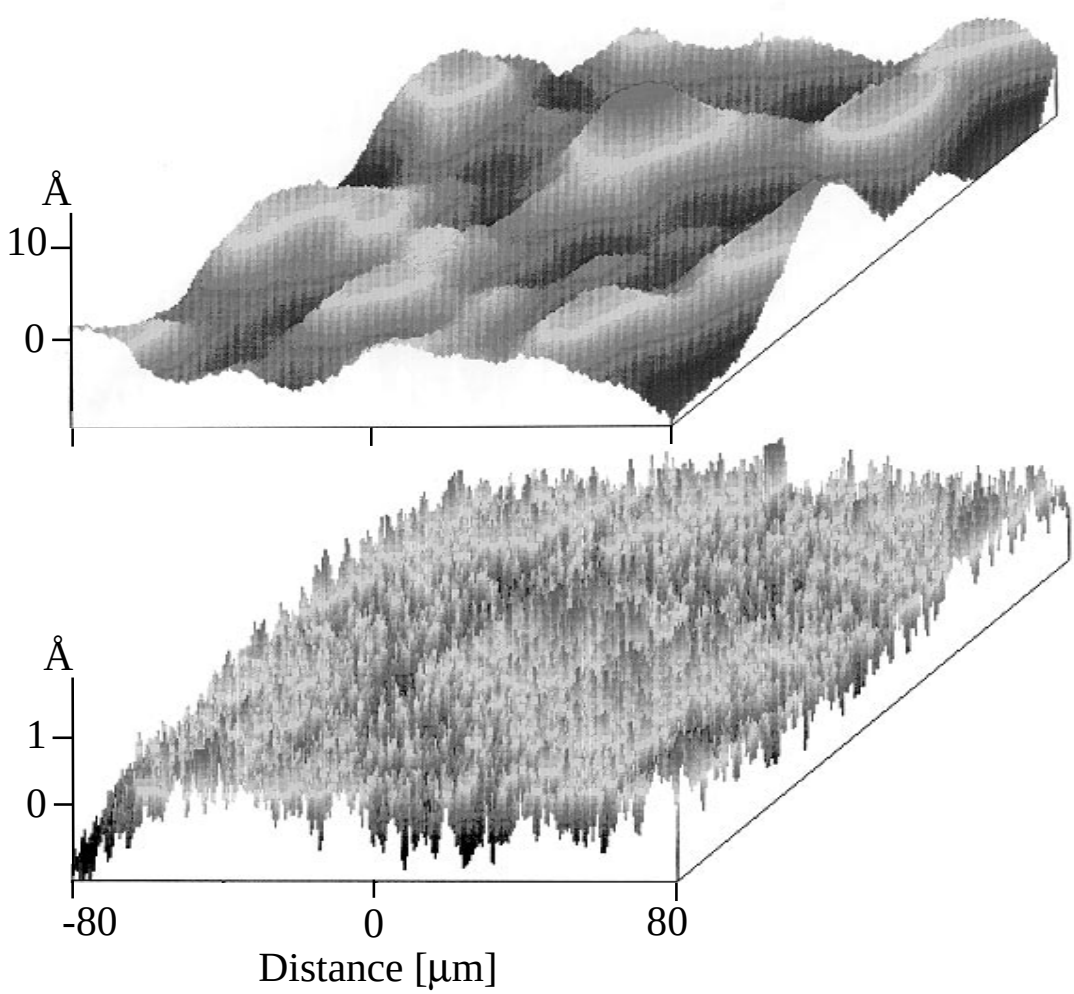

Figure 6.11: *Surface measurements of the vane of the silicon torsional oscillator before coating (upper image) in comparison with a quartz substrate used for high finesse coatings. Both images were taken with a Micromap interferometer. The waviness of the Si-surface can clearly be seen. Note also the difference in the scaling of both plots.*

that high-finesse coatings were applied to silicon substrates. For the first experimental tests of the cavity stabilization and measurements of the oscillator's Brownian motion, the finesse values of the coatings so far were sufficient. For further experiments, improvements by a factor of 10 are necessary. Regarding the surface measurements of this section this should be possible to achieve.

6.3 The cryostat

The cryostat was designed especially for this experiment by the company Cryovac, Troisdorf. It is cooled by ^{4}He without nitrogen pre-cooling. It contains an upper storage vessel with a capacity of 7 l and a lower 2.3 l vessel, which is used for cooling by evaporation of ^{4}He. Besides the main outer steel envelope, the LHe tanks are protected by three copper radiation shields each covered with layers of superinsulation. Of the four suprasil

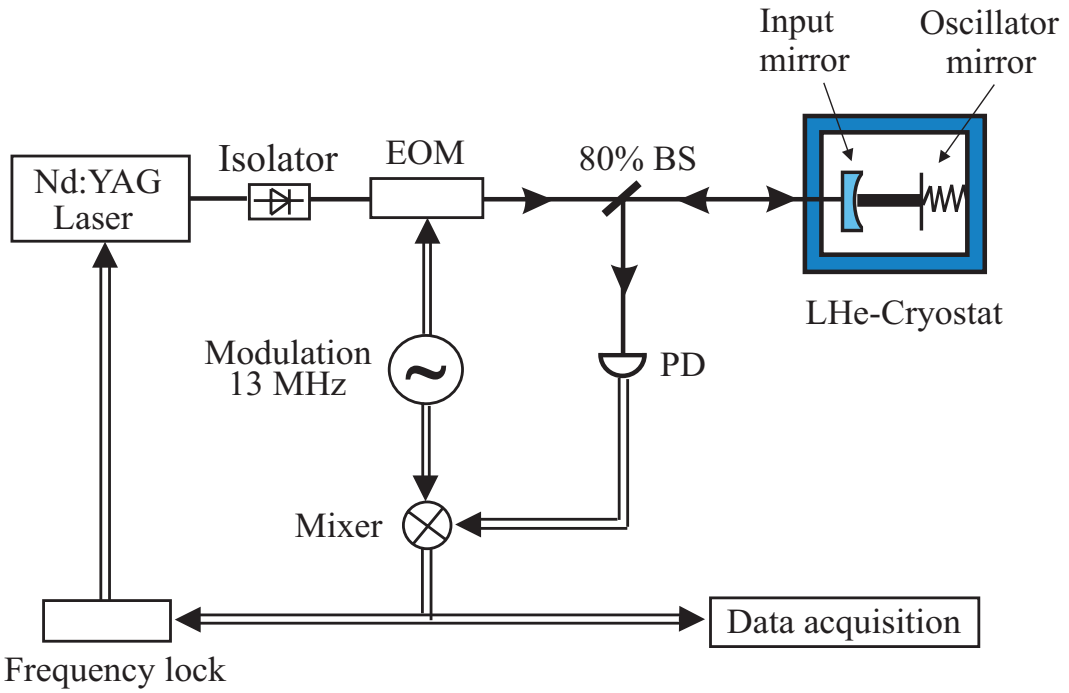

Figure 6.12: *Schematic of the experiment. PD photo detector, BS beam splitter, EOM electro-optic modulator.*

windows tilted by an angle of 5° to avoid back reflections, we replaced two by copper rings, to minimize the loss of the laser beam traversing to and from the main chamber (⌀ 160 mm, height 70 mm). The temperature inside the cryostat is monitored by two calibrated germanium sensors, one fixed at the bottom plate of the lower He-tank, the other in the Invar holder near the oscillator's vane. For temperatures >40 K a Pt-100 resistor is employed. Once cooled down in ≈ 6 hrs the cryostat remains at 4 K without refill for more than 24 hrs. The lowest temperature achieved so far by pumping the lower ^{4}He-vessel was 2.2 K.

6.4 The setup

A schematic of the experiment is shown in Fig. 6.12. The optomechanical sensor is housed in the LHe-cryostat. The Invar holder onto which the oscillator is glued is attached to a larger Invar block fixed tightly to the bottom plate of the lower ^{4}He-vessel. A rigid incoupling mirror is mounted on the block's side opposite to the oscillator mirror, thus forming a cavity of length L_c=1 cm (free spectral range FSR=$c/2L_c$=15 GHz). The concave input coupler with 10 cm radius has a transmissivity $1 - r_1^2 = 50$ ppm. The finesse of the cavity is $\mathcal{F}$ =15 000 (undercoupled), limited by the loss of the oscillator mirror. A 300 mW diode-pumped monolithic Nd:YAG laser (Lightwave model 122) is used as a light source, with typical laser powers incident onto the cavity around 5 mW. The beam traverses an EOM (Gsänger) which is driven by a function generator (HP 33120 A) having an HF-amplifier (minicircuits ZHL-6A) added at its output port. The electronic power transfer to the EOM is enhanced by a resonance circuit. Thus at phase

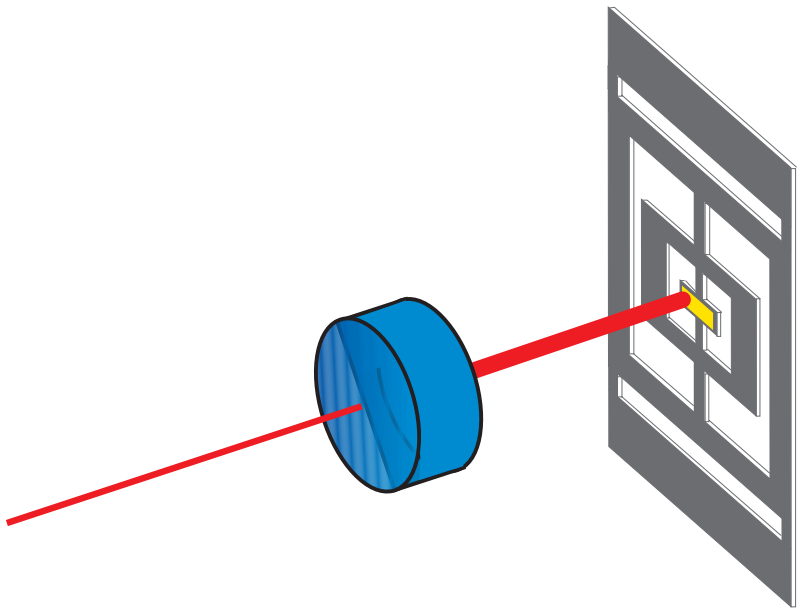

Figure 6.13: *Schematic of the cavity employing the vane of the silicon torsional oscillator as a moving mirror.*

modulation frequencies around 13 MHz a modulation index $\epsilon = 0.8$ was reached. We verified via homodyne detection that in this frequency range the laser intensity noise level is at the shot-noise level for the given 5 mW power level. The read-out sensitivity was therefore not limited by technical laser noise.

Since the rigid incoupling mirror was not adjustable, in order to keep the cavity alignment stable during the cool down period, modematching of the laser mode into the cavity situated inside the cryostat was a tedious task. A modematch efficiency of $\approx 50\,\%$ was typically reached.

The back reflected beam is split off by a 80 % beam splitter and directed to an InGaAs photodetector (Epitaxx ETX500). In the earlier stage of the experiment a configuration with a $\lambda/4$-plate and a polarizing beam splitter was used. It was discarded since the circularly polarized light incident onto the cavity led to a polarization splitting of the cavity modes when the system was cooled down. This indicates a birefringence of the mirror coatings at low temperatures. Since the back reflected beam loses 20 % power at the beam splitter and also has to traverse the two tilted windows of the cryostat (loss $\approx$ 10 %) the overall detection efficiency η was $\approx 65\%$.

A Pound-Drever technique was used to stabilize the laser frequency to the cavity [59, 91]. The demodulation signal for the AC-output of the photodetector was provided by a second HP 33120 function generator, phase-locked to the first one. By adjusting phase and amplitude of both function generators an optimum error signal was generated. Fig. 6.14 shows a typical scan across the cavity resonance with the corresponding error signal.

The error signal was split into a high frequency part (>10 kHz), which serves for the analyzation of the oscillator's motion and a low frequency part, which is directed to the fast-input of the laser control to regulate the laser frequency via a piezoelectric transducer glued onto the laser crystal. The bandwidth of the feedback loop for the locking is 300 Hz.

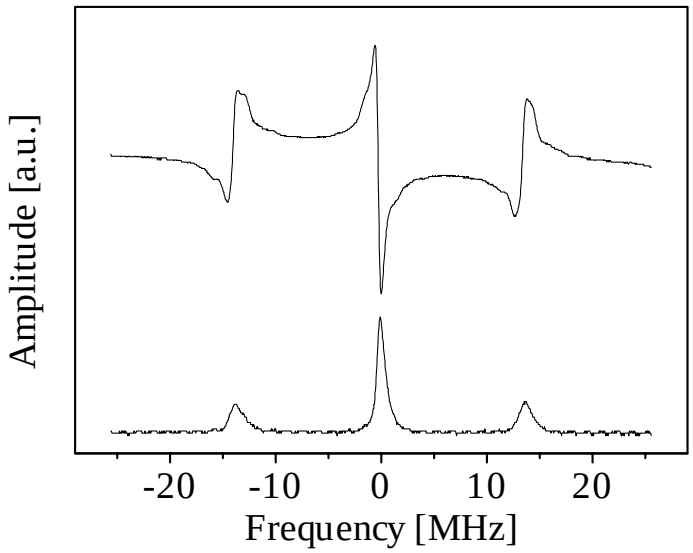

Figure 6.14: *Scan of the laser frequency across the resonance of the cryogenically cooled cavity (lower figure). The two sidebands at ± 13 MHz are clearly visible, the finesse amounted to 11 000 in this measurement. The corresponding error signal is shown above.*

In addition, an extra bandfilter at the oscillator's resonance 26 kHz had to be inserted to avoid electronical feedback to the oscillator's motion. At room temperature, the frequency lock was stable over minutes, on quiet days with low seismic noise even for tens of minutes. At cryogenic temperatures the lock became unstable after seconds. This is either due to temperature effects, or to the ten times enhanced mechanical responsivity of the mirror oscillator due to its increased mechanical Q. The problem of seismic disturbances due to boiling LHe can be circumvented by operating the system after the cool down period for 1-2 hours with empty storage vessels.

While the laser frequency is stabilized to the cavity, the high frequency part of the error signal is either analyzed by a lock-in detector to measure the oscillator's motion in the time domain, or by a spectrum analyzer for quantitative evaluations in the frequency domain.

For adjustment of the cavity and control of the lock stability a second detector and a CCD-camera is placed at the rear side of the cryostat to monitor the transmitted beam. The whole setup, including the cryostat, was mounted on a vibration isolated optical table of Newport, Irvine CA.

6.5 Interferometric measurements of the oscillator's motion

The setup with the optomechanical sensor allows detailed studies of the Brownian motion of the moving mirror. The time domain analysis [206] of the oscillator motion is performed by feeding the cavity detuning error signal into a two-phase lock-in amplifier, with a reference frequency equal to the resonance frequency ω_0. The integration time constant corresponds to τ. Fig. 6.15 shows a phase plot of the two quadratures of the error signal

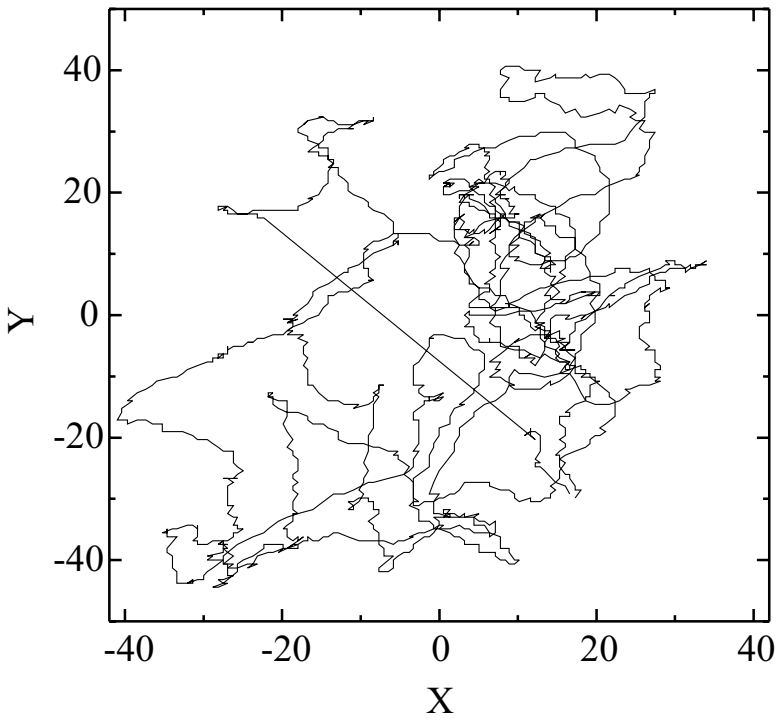

Figure 6.15: *Phase space trajectory of the oscillator at room temperature driven by thermal noise during a time interval of 80 s. One larger jump corresponding to a laboratory disturbance can be seen. For comparison: the trajectory of an excited noiseless oscillator would be just a point in phase space, since the coordinate system rotates with the oscillator's resonance frequency ω_0, due to the detection method, employing a lock-in amplifier at ω_0.*

near ω_0, showing the Brownian random walk of the oscillator at room temperature. Note that this mapping of the oscillator's statistics in phase space comes quite close to the measurements presented in the first part of this thesis, in particular the one of the thermal state of the light field.

For a frequency domain analysis, the error signal is recorded with a SRS 780 FFT spectrum analyzer. Recording with frequency intervals smaller than the oscillator's linewidth, enables us to determine mechanical properties from interferometric measurements. In Fig. 6.16 a Q-factor measurement at room temperature is shown. To map out the line shape a measurement bandwidth of one tenth of the oscillator's linewidth (≈ 0.01 Hz) is used. Furthermore the spectra are averaged 10 times, to reduce the disturbances due to background noise. For high Q-factors, such as the ones of the cryogenically cooled oscillators the resulting time span of 20 minutes for the necessary 10 measurements exceeds until now the time interval where the lock operates stable at low temperatures.

6.5.1 Quantitative evaluation, comparison with theory

The spectrum analyzer provides a power spectrum of the cavity detuning $\Delta^2\nu$, which is equivalent to the square of the oscillator's displacement Δx from 0 at a specific frequency.

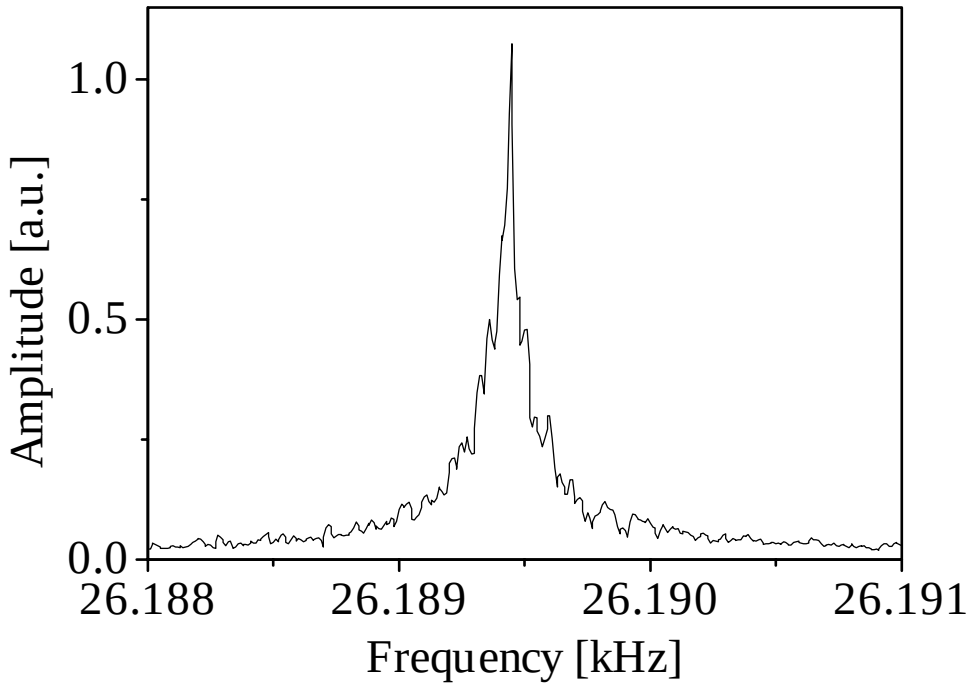

Figure 6.16: *Linewidth of the mechanical resonance of the oscillator at room temperature, measured by reading out the error signal of the Fabry-Perot interferometer at the oscillator's resonance. The Q-factor $\nu/\Delta\nu$ amounted to 140 000 in this measurement. This is in agreement with decay time measurements for this oscillator, which was at room temperature exposed to a slight strain due to the fastening by 4-point glueing.*

To quantitatively evaluate the oscillator's motion, we performed short time measurements, with measurement times τ smaller than the decay times τ^* of the oscillator. In the resulting spectrum one integrates over the whole mechanical resonance, thus making the peak value at the resonance frequency comparable to a calibration signal generated by a function generator whose linewidth is also negligibly small compared to the measurement bandwidth.

The calibration signal is gained the following way: To the last stage of the lock-in amplifier used for the laser frequency stabilization via the fast-input of the laser control, a weak modulation is added. The modulation frequency of 26 kHz was chosen to be sufficiently separated from the mechanical resonance frequency, but sufficiently close so that the error signal gain is the same. Knowing the modulation amplitude U determines the amount of modulation $\Delta\nu$, since the transfer coefficient

$$\frac{\partial\nu}{\partial U} = 4.54 \pm 0.2 \frac{\mathrm{MHz}}{\mathrm{V}}, \tag{6.8}$$

at 26 kHz was measured independently by scanning the laser frequency, using modulated side bands as a reference. The calibration for the spacial displacement follows straight from the cavity geometry: $\Delta x_{cal} = \Delta\nu\lambda/(2 \cdot \mathrm{FSR})$.

Typically, the spectrum was recorded with a 0.25 s integration time. This is an order of magnitude less than τ^*. Therefore the spectrum was averaged 30 times for room temperature and 100 times for cryogenic measurements.

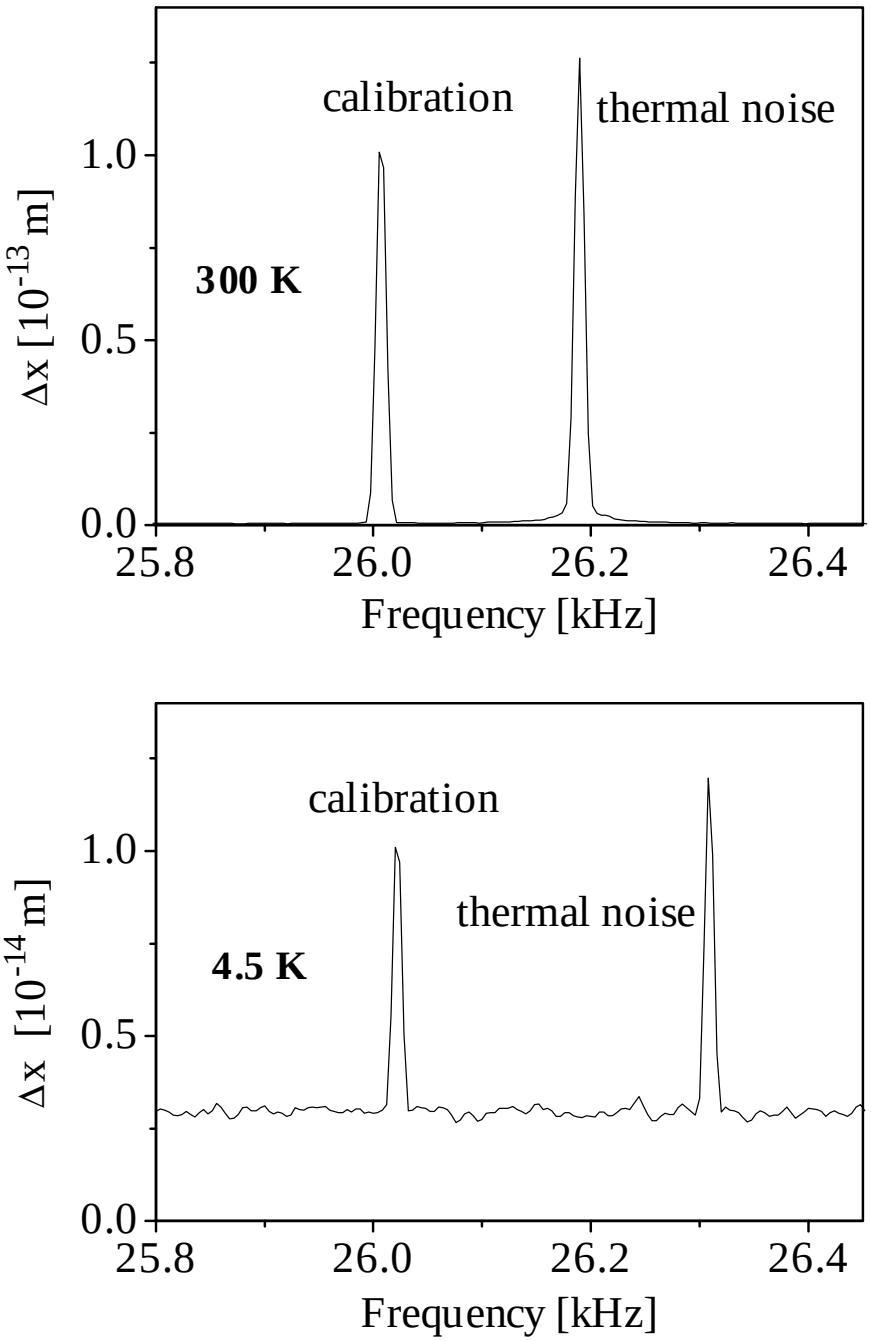

Figure 6.17: *The spectrum of the cavity detuning error signal at room temperature and 4.5 K. The peak at 26.2 kHz for the room temperature measurement and 26.3 kHz for the measurement at 4.5 K has its origin in the Brownian motion of the mechanical oscillator. The observed shift of the oscillator's resonance is due to the increased spring constant at lower temperatures. The calibration peak at 26 kHz is obtained by frequency-modulating the laser. The measurement bandwidth was 4 Hz. Note the different vertical scaling of the two coordinate systems, demonstrating the expected 10-fold decrease of the oscillators amplitude at 4.5 K compared to room temperature.*

Fig. 6.17 shows two typical results. At 26.2 kHz for the room temperature measurement and at 26.3 kHz for the cryogenic setup the motion of the torsional oscillator is clearly observed. The measured noise levels of $\Delta x = 1.28 \pm 0.6 \cdot 10^{-13}$ m at 300 K and $\Delta x = 1.33 \pm 2 \cdot 10^{-14}$ m at 4.5 K agree with the theoretical expectation for thermal motion

$$\Delta x_{TH} = \sqrt{\frac{k_B T}{m\omega_0^2}} = \begin{cases} 1.3 \pm 0.6 \cdot 10^{-13}\,\text{m at } 300\text{ K} \\ 1.5 \pm 0.7 \cdot 10^{-14}\,\text{m at } 4.5\text{ K} \end{cases} \tag{6.9}$$

The large error for the theoretical estimates comes from the fact that the distance d of the laser beam's spot on the vane to the vane's torsion axis, which is used for the determination of the mass m, can only be estimated up to a factor of 1.5.

To give an impression of the status of the experiment, the results of the two measurements of Fig. 6.17 are marked in Fig. 5.2 of the theory section. With the present optical power, improvements in the finesse value by at least a factor of 10 are necessary to reach the back action regime.

Note that for measurement times τ smaller than the oscillator's decay time τ^* usually a correction factor to Δx_{TH}^2 is introduced [267]. The argument for this is as follows. If the oscillator's excitation amplitude as a function of time is recorded, the probability to measure at a time τ the amplitude x, given that at time 0 the oscillator's amplitude was x_0 is given by the conditional probability [80]

$$P(x, \tau | x_0, 0) \simeq \exp\left(-\frac{m\omega_0^2 \langle x - \bar{x} \rangle^2}{2\, k_B T (1 - e^{-\tau/\tau^*})} \right), \tag{6.10}$$

where $\bar{x} = x_0\, e^{-(\tau/\tau^*)}$. In comparison with Eq. 5.23 the finite speed of the oscillator's thermal motion, the autocorrelation of its trajectory is taken into account. The variance of this distribution leads to a corrected displacement uncertainty of

$$\Delta x_{TH,cor}^2 = \frac{2\, k_B T (1 - e^{-\tau/\tau^*})}{m\omega_0^2} \approx \frac{k_B T\, \tau}{m\omega_0^2\, \tau^*}. \tag{6.11}$$

This expression, however, is not in agreement with the observed behavior. In the measurements done so far, no bandwidth (measurement time interval) dependence of the signal height was observable for $\tau < \tau^*$, i.e. BW $> \Delta\nu_0$. The reason for this is the following. What is measured by a spectral analysis of an interferometric setup like the one presented here, is not the change of the oscillator's amplitude at its resonance frequency, but the root mean square value of its amplitude in the measurement interval. For an amplitude distribution with a mean of 0, the latter is equivalent to a direct measurement of the standard deviation Δx. Thus for arbitrary short measurement times the approximately correct thermal displacement uncertainty can be gained. The only restriction is that the thermal probability distribution given in Eq. 5.23 is truly randomized only at time scales comparable to τ^*. Thus in order to obtain a statistically significant mean for Δx_{TH}, a large number N of amplitude measurements has to be performed such that $N \cdot \tau > \tau^*$.

For further clarification let us return to Fig. 6.15. The variance of the phase space distribution obtained from the depicted trajectory is equal to the displacement uncertainty Δx. If we denote by τ the overall time of measurement of the phase space trajectory, it

can be readily understood that only for $\tau \to \infty$ the correct value for Δx_{TH} is gained, and that for short sampling times, where the oscillator's movement covers only a small section of the phase space, Δx_{TH} will be correspondingly smaller, proportional to $\sqrt{\tau}$. In contrast to this, a spectrum analyzer does not measure the variation of the amplitude, but its absolute value, i.e. the distance of the points in Fig. 6.15 to the phase space origin. This explains why Eq. 6.10 does not apply to the measurement shown in Fig. 6.17.

Note also that apart from these considerations for the quantum mechanically correct calculation of the Brownian motion, a small correction term has to be added to Eq. 5.23 [246]. For the present experimental parameters this term, scaling with $\hbar^2$, is negligible.

Sensitivity of the interferometer

The displacement sensitivity for the measurement of the oscillator motion, obtained from the error signal noise floor, is $2 \cdot 10^{-16}$ m/$\sqrt{\text{Hz}}$.[1] The expected level from Eq. 5.17 is $\sqrt{S_{SN}} = 3 \cdot 10^{-19}\text{m}/\sqrt{\text{Hz}}$. Electronic noise is responsible for the difference, thus for measurements of the oscillator's motion at frequencies away from the resonance this value has to be improved considerably. The state of the art in the sensitivity of prototype small scale gravitational wave interferometers is of the order of 10^{-18} m/$\sqrt{\text{Hz}}$ [139, 201, 108, 98].

6.5.2 Remarks about the influence of thermal effects

One of the major problems in future experiments with our setup will probably not be the detection of a light power dependent excitation of the oscillator, but the distinction, as to which effect of the ones mentioned in section 5.4 actually causes this excitation, and, even more important and not discussed so far, as to whether any observed effect may be due to photothermal excitation [129, 152, 46].

Fig. 6.18 shows the absorption profile of the uncoated silicon. The sharp edge indicates the bandgap energy of silicon which is just matched by the energy of the 1064 nm photons. About one third of the laser's power is absorbed. This dissipated power leads to heating effects whose influence on the oscillator's motion are difficult to estimate in magnitude. In contrast to other experiments employing microoscillators, in which cantilever or brigde structures were excited into a bending motion by the optothermal effect (Refs. see Sec. 6.6.2), there is no direct torsional moment caused by thermal effects, which could be transferred to the oscillator employed here. Nevertheless it was found experimentally that it is possible to excite the oscillator by periodically heating via a copper coil fixed to the Invar holder.

A possible experimental distinction between radiation pressure and thermal effects could be realized by checking not only the power and frequency dependence of the relevant equations, but also the wavelength dependence. This way not only an additional parameter could be investigated, but also due to the different absorption for different wavelengths, thermal effects could be checked independently. Practically, this idea could

[1] Note that the noise floor of the cryogenic measurement in Fig. 6.17 is higher than the value given here. This is due to intrinsic electronic noise of the SRS 780 FFT spectrum analyzer. To avoid this, a reset of the spectrum analyzer by pressing the backspace button while booting should be made before any serious measurement.

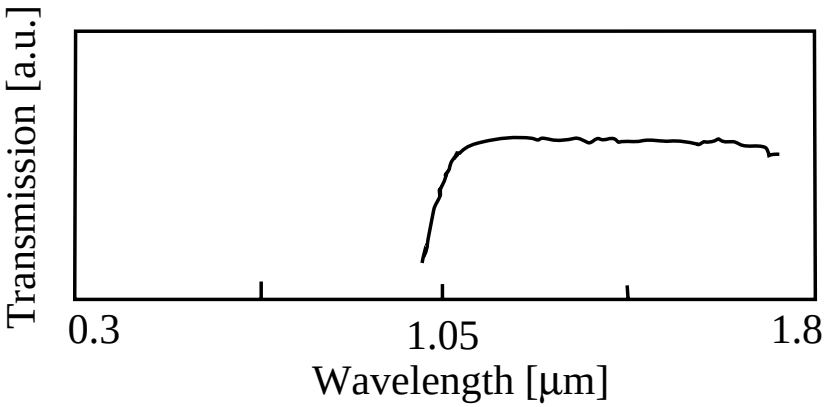

Figure 6.18: *Absorption profile of silicon. Measured is the transmission of a white light source with an Anritsu optical spectrum analyzer.*

be easily (...) implemented, employing the newly available widely tunable, compact and stable cw-OPO light sources developed in our group [220].

Another possibility is, in case future coating runs turn out more successful, to compare the data for oscillators with different finesse. Thermal excitation should decrease, radiation pressure excitation should increase with improved reflectivities of the Si-coating.

A third possibility would be, to estimate the photothermal excitation by shining a 1064 nm wave onto the oscillator's vane from the back side of the cavity, while the incoupling side is used as before for locking and reading out the oscillator's displacement. With this method, the strength of the photothermal excitation could be checked independently from the cavity's circulating light power.

6.6 Related experiments of other groups

This chapter serves the purpose of setting our experimental efforts and results in a more general frame, relating it to achievements elsewhere. Besides that, during the time of this thesis it was seen that the experimental implementation of radiation pressure effects, opto-mechanical coupling, moving mirrors, laser interferometric measurements of Brownian motion are also important subjects in experiments which are, considering the final goals, not directly related to the one presented here, but nevertheless employ similar techniques that might be helpful in the further progress of our experiment as well.

6.6.1 Directly comparable experiments

There are, to my knowledge, four directly comparable experiments. One in Hannover, in the vicinity of the gravitational wave detection project (K. Danzmann), one in Paris, in the quantum optics group at Jussieu (A. Heidmann), one test setup for an optical transducer for resonant gravitational wave detection in College Park, Maryland (Y. Pang and J.P.Richard) [176] and one as a part of the gravitational wave detection project at the University of Western Australia (Blair) [247].

The Hannover group employs a pendulum quartz mirror with a resonance frequency in the Hz regime, $Q = 5 \cdot 10^6$. The goal is to detect the SQL at room temperature by

measurements in the frequency domain off-resonance. Due to seismic disturbances, laser stabilization is extremely difficult in such a setup. Furthermore, the higher temperature leads to higher requirements for the mechanical Q-factor and the finesse.

The Paris group uses the bulk oscillations of a silicate mirror. Advantages here are the lack of disturbance by seismic effects at the resonances in the MHz regime, and that the whole system is very compact. As in our case, it is planned to be mounted in a cryostat. The primary goal in this experiment is the detection of squeezing in the reflected light field, due to the opto-mechanical interaction. Disavantages are the large spring constant and the higher requirements for the mechanical Q-factor due to the higher frequency.

Both projects profit from the fact that well-known standard coating procedures can be employed to reach a high finesse. Nevertheless, since apart from theoretical considerations [63, 86] and initial studies [249] both groups have not published anything so far, it is hardly possible to estimate, which experimental design will be the most successful in the long run.

The optical transducer by Pang and Richard has a finesse of 70 000 but only a moderate mechanical quality factor of 3000. Until now, it has not been cooled down and no back action effects have been observed.

The australian project is probably the most advanced of the experimental setups presented here. Its main difference from the other three setups is that it operates at microwave instead of optical frequencies. The final setup of the experiment has not been decided yet. Test setups involved as mechanical oscillators bulk oscillations of sapphire bars (ν =10 GHz), tuning fork resonances of slotted sapphire (ν = 1 kHz, $Q = 3 \cdot 10^7$ at 4 K) and niobium ($Q = 2 \cdot 10^7$ at 4 K) bars, and membrane oscillations of a niobium membrane ($Q = 10^5$). For the bulk oscillations in sapphire, Q-values of 10^8 were measured [106]. Using whispering gallery modes in a monocrystalline sapphire dielectric resonator classical radiation pressure effects were detected [44].

The investigation of back-action effects and Brownian motion in an *electromechanical* sensor is described in [147].

6.6.2 Experiments employing similar techniques

Many experimental techniques can be learned and a variety of classical opto-mechanical effects can be understood from previous experiments employing micromechanical oscillators in sensor technology. Thermal excitation of micromechanical silicon sensors has been demonstrated in [209, 128]. Optical excitation and/or readout of micromechanical silicon sensors have been described in [258, 3, 105, 244, 273, 285, 182, 129, 286, 254, 190, 43, 251]. All experiments employ interferometric detection methods via optical fibers, and oscillators of bridge or cantilever structure with low or medium mechanical Q. The excitation mechanism does not involve radiation pressure, but rather optothermal coupling [129, 286, 46]. The experiments of this category closest to ours make use of an optical cavity, formed by the tip of the fiber used to excite the oscillator and the coated oscillator itself [234, 190, 36] or by silicon microcavities [288] (see also [131, 82]). With such setups, optical feedback due to the change in the intracavity circulating power induced by the oscillator's motion, similar to the one described in section 5.4 has been observed [131, 234, 36, ?, 82, 195].

A similar category of experiments with weak forces acting on optically monitored microoscillators is the high precision AFM detection [205, 160]. Using fiber optical readout techniques for silicon cantilevers, force sensors with attonewton precision have been fabricated [236].

Micromechanical silicon oscillators that are especially designed to form optical mirrors have been fabricated within the framework of optical switches at Texas Instruments [207] (see also [99]). Since these devices are fabricated to exhibit a fast bistable response via tilting of the micromirror instead of continuous oscillation, no values for the mechanical Q-factor have been given. Switching times are 10 μs for the 1° angle.

As a last quite exotic but closely related experiment in biophysics I want to mention the recently measured Brownian motion of hair bundles in the inner ear by laser interferometry [56, 97]. Reaching the eardrum, the acoustic wave is transmitted through mechanical and hydraulic linkages to a set of receptor cells, the hair cells in the spiraling cochlea contained in the inner ear. Each hair bundle, situated at a specific place of the basilar membrane, is resonant at a specific frequency, allowing thus a spatial separation and distinction of different frequencies of the incoming wave. Just as in our setup, the Brownian motion of these mechanical receptors limits the degree of sensitivity at which small forces (faint acoustic signals) can be detected (heard). Besides the detection of this Brownian motion, in a series of beautiful experiments [202, 103, 97] it was shown, how nonlinear mechanical properties, comparable to the ones shown in section 6.1.5, lead to auditory illusions, such as the two-tone distortion, well-known in Baroque music theory.

6.7 Outlook part II

The further development of the experiment will most likely come in two stages:

The short term goals are achievable with the present setup. With an improvement of the lock stability, which may comprise a vibration isolation for the cryogenic cavity, long time stabilized operation at cryogenic temperatures and therewith a better understanding of the Brownian noise measurements and measurements of the classical back action should be possible. Probably the most difficult task will be to thoroughly understand the DC radiation pressure effects caused by the oscillator's motion and the influence of photothermal excitation. In principle, DC radiation pressure effects may be circumvented by detecting off-resonance, however, for this a substantial increase in the interferometer's sensitivity is necessary.

The medium term goal consists in manufacturing another set of mechanical oscillators with new optical coatings. If the finesse values can be improved by a factor of 10 or more, the detection of radiation pressure damping and of quantum back action is in principle possible. As mentioned before, the main difficulty will be the correct interpretation of any measured light power dependence of the oscillator's motion.

Besides these more technical suggestions, there are certain aspects/features of the experiments in part I and part II of this thesis, that may unify both experiments in the more distant future.

The first is, to investigate the output light field of the movable mirror cavity via tomographical methods. In the regime of quantum back action a $\chi^{(3)}$-squeezing should be

observable, which in the ideal case should have a non-Gaussian phase space distribution [88, 63, 148, 261].

The second proposal is valuable only if the interferometer is operated in the back action regime where it is limited by the quantum noise introduced by the light field. It consists in increasing the interferometer's resolution by the injection of squeezed vacuum proposed 1981 by Caves [40] and recalculated in [101, 143, 175]. Note also that due to the squeezing effect of the interferometer in the back action regime, a resolution enhancement can already be achieved by detecting not the intensity or the phase but a specific quadrature of the output field [261].

The third proposal has its origin in the analogy of the light field's and the mechanical oscillator's harmonic time evolution. This becomes evident in the similarity of the phase space investigations of both experiments: The measurement of the oscillator's Brownian motion in Fig. 6.15 is the exact classical analogue to the measurement of the thermal state of the light field. A similar analogy was pointed out in section 6.1.5 and Ref. [206] regarding the nonlinear effects in both systems.[2] Since it is a present research endeavour of several groups investigating techniques of micromachining to fabricate oscillators that exhibit quantum mechanical behavior at cryogenic temperatures, tomographical characterization of the mechanical noise properties of such oscillators via interferometric detection would offer a powerful tool of analyzation for such devices.

[2] See also [167] for a discussion of the relation between Brownian and quantum noise.

*

7 Conclusion

If science has taught us anything, it is that the environment is full of uncertainties.

Prince Charles

The thesis presents two experiments to investigate the quantum nature of light. In the first part, a complete experimental characterization of the whole family of squeezed states of the light field and of incoherent superpositions of coherent states is presented. Average photon number and orientation of the states in phase space were accurately controlled by macroscopic experimental parameters. The degree of squeezing amounted with 6 dB to the present state of the art in the world. It should be noted that the presented measurements do not give a proof of the correctness of quantum mechanics or evidence for the particle nature of light, since the laws of quantum mechanics had to be used for the interpretation of the measured data. Nevertheless it is the first time that such detailed experimental descriptions of non-classical states of the light field are being made available. The quantum state reconstructions were performed in quasi real time, with a data acquisition time of 200 ms and an analyzing time of $\approx$20 s. The results are in very good agreement with theory. Among the special quantum mechanical features observed were oscillations in the photon number distribution, amplitude-squeezed light with either sub- or super-Poissonian photon statistics, bifurcation of the phase distribution, verification of the number-phase uncertainty for squeezed states, higher order squeezing, loss of coherence by phase diffusion, and the exponential decay of the first-order time correlation function of the squeezed vacuum.

In the second part, a cryogenically cooled Fabry-Perot interferometer with a movable mirror for high precision position measurements was built in order to observe the quantum back action of a probe laser beam that monitors the movable mirror's position. Thermal motion in the order of 10^{-14} m of the high Q mirror oscillator at 4.5 K was detected. First effects of opto-mechanical coupling were observed.

The outlooks for both experiments have been given separately in Sec. 3.11 and Sec. 6.7 respectively. It is hoped that the continuation of both projects will lead to the exploration of yet unknown states of light and to the first evidence of the effect of the momentum transfer of single quanta of light to a macroscopic object, thus elucidating new aspects of the never completely comprehensible quantum world.

Bibliography

[1] G.I. Abbas, V.W.S. Chan, and T.K. Yee, "Local-oscillator excess-noise suppression for homodyne and heterodyne detection", Opt. Lett. **8**, 419 (1983);

[2] V. Aksyuk, F.F. Balakirev, G.S. Boebinger, P.L. Gammel, R.C. Haddon, D.J. Bishop, "Micromechanical "trampoline" magnetometers for use in large pulsed magnetic fields", Science **280**, 720 (1998);

[3] M.V. Andres, K.W.H. Foulds, and M.J. Tudor, "Optical activation of a silicon vibrating sensor", Electr. Lett. **22**, 1097 (1986);

[4] F.T. Arecchi, "Measurement of the statistical distribution of gaussian and laser sources," Phys. Rev. Lett. **15**, 912 (1965); F.T. Arecchi, A. Berné, and P. Bulamacchi "High-order fluctuations on a single mode laser field," Phys. Rev. Lett. **16**, 32 (1966);

[5] A. Assion, M. Geisler, J. Helbing, V. Seyfried, and T. Baumert, "Femtosecond pump-probe photoelectron spectroscopy: Mapping of vibrational state motion", Phys. Rev. A **54**, R4605 (1996);

[6] J. Bajer, "Photon statistics of the Nth subharmonics", J. Mod. Opt. **38**, 1085 (1991);

[7] K. Banaszek and K. Wodkiewicz, "Direct probing of quantum phase space by photon counting", Phys. Rev. Lett. **76**, 4344 (1996);

[8] K. Banaszek and P.L. Knight, "Quantum interference in three photon down conversion," Phys. Rev. A **55**, 2368 (1997);

[9] K. Banaszek, "Maximum-likelihood estimation of photon number distribution from homodyne statistics", to be published;

[10] M.J. Bastiaans, "Application of the Wigner distribution function to partially coherent light", Phys. Rev. A **3**, 1227 (1986);

[11] M. Beck, D.T. Smithey, J. Cooper, and M.G. Raymer, "Experimental determination of number-phase uncertainty relations," Opt. Lett. **18**, 1259 (1993);

[12] C. Becher, E. Gehrig, and K.J. Boller, "Spectrally asymmetric mode correlation and intensity noise in pump-noise-suppressed laser diodes", Phys. Rev. A **57**, (1998);

[13] J. Bertrand and P. Bertrand, "A tomographic approach to Wigner's function" Found. Phys. **17**, 397 (1987);

[14] J.E. Bjorkholm, A. Ashkin and R.G. Smith, "Improvement of optical parametric oscillators by nonresonant pump reflection," IEEE J.Quant.Electr. **QE-6**, 797 (1970);

[15] D.M. Bloom, G.W. Bekkers, J.F. Young, and S.E. Harris, "Third-harmonic generation in phase-matched alkali metal vapors," Appl. Phys. Lett. **26**, 687 (1975);

[16] K. Blum, *Density matrix theory and applications*, Plenum Press, New York (1981);

[17] M.F. Bocko and R. Onofrio, "On the measurement of a weak classical force coupled to a harmonic oscillator: experimental progress", Rev. Mod. Phys. **68**, 755 (1996);

[18] D. Boggavarapu, D. McAlister, M. E. Anderson, M. Munroe, M. G. Raymer, G. Khitrova, and H. Gibbs, "Ultrafast photon statistics of normal mode coupling in a semiconductor microcavity", Proceedings of Quantum Electronics and Laser Science Conference (June 2-7, 1996, Opt. Soc. of Am., Technical Digest Vol.9, 1996), pg.33.; M. E. Anderson, M. Munroe, U. Leonhardt, D. Boggavarapu, D. F. McAlister and M. G. Raymer, "Ultrafast Balanced-Homodyne Chronocyclic Spectrometer", Proceedings of Generation, Amplification, and Measurement of Ultrafast Laser Pulses III, pg 142-151 (OE/LASE, San Jose, Jan. 1996) (SPIE, Vol. 2701, 1996);

[19] F. Bondu, P. Fritschel, C.N. Man, and A. Brillet, "Ultrahigh-spectral-purity laser for the VIRGO experiment", Opt. Lett. **21**, 582 (1996)

[20] S. Bondurant and J. H. Shapiro, "Use of squeezed light in phase-sensitive interferometers", Phys. Rev. D **30**, 2548 (1984);

[21] G. D. Boyd and D. A. Kleinman, "Parametric Interaction of Focussed Gaussian Light Beams," J. Appl. Phys. **39**, 3597 (1968);

[22] V.B. Braginsky and A.B. Manukin, Zh. Eksp. Teor. Fiz. **52**, 998 (1967);

[23] V.B. Braginsky, A.B. Manukin *Measurement of weak forces in physics experiments*, Univ. of Chicago Press, Chicago 1977;

[24] V.B. Braginsky, V.P. Mitrovanov, V.I. Panov *Systems with small dissipation*, Univ. of Chicago Press, Chicago 1985;

[25] V.B. Braginsky, F.Y. Khalili, *Quantum Measurement*, K. P. Thorne (Ed.), Cambridge University Press, 1992;

[26] S. Brandt and H.D. Dahmen *The picture book of quantum mechancics*, Springer, Berlin 1994;

[27] S.L. Braunstein and R.I. McLachlan, "Generalized squeezing", Phys. Rev. A **35**, 1659 (1987); S.L. Braunstein and C.M. Caves, "Phase and honodyne statistics of generalized squeezed states", Phys. Rev. A **42**, 4115 (1990);

[28] G. Breitenbach, T. Müller, S. Pereira, J.-P. Poizat, S. Schiller und J. Mlynek, "Squeezed Vacuum from a Monolithic Optical Parametric Oscillator", J. Opt. Soc. Am. B, **12**, 2304 (1995);

[29] G. Breitenbach, S. Schiller and J. Mlynek, "81% Conversion Efficiency in Frequency-stable Continuous-Wave Parametric Oscillation", J. Opt. Soc. Am. B, **12**, 2095 (1995);

[30] G. Breitenbach, S. Schiller, and J. Mlynek, "Measurement of the quantum states of squeezed light", Nature, **387**, 471 (1997);

[31] G. Breitenbach and S. Schiller, "Homodyne tomography of classical and non-classical light", J. Mod. Opt. **44**, 2207 (1997);

[32] G. Breitenbach, S. Schiller, and J. Mlynek, "Broadband quantum state reconstruction of squeezed vacuum: A spectrum of quantum states", to appear in Europhys. Lett.;

[33] M. Brune, E. Hagley, J. Dreyer, X. Maître, A. Maali, C. Wunderlich, J.M. Raimond, and S. Haroche, "Observing the progressive decoherence of the meter in a quantum measurement", Phys. Rev. Lett. **77**, 4887 (1996);

[34] R. Bruckmeier, K. Schneider, S. Schiller, and J. Mlynek, "Quantum nondemolition measurements improved by a squeezed meter input", Phys. Rev. Lett. **78**, 1243 (1997); R. Bruckmeier, H. Hansen, S. Schiller, and J. Mlynek, "Realization of a paradigm for quantum measurements: The squeezed light beamsplitter", Phys. Rev. Lett. **79**, 43 (1997);

[35] B.C. Buchler, E.H. Huntington, C.C. Harb, and T.C. Ralph, "Feedback control of laser intensity noise", Phys. Rev. A **57**, 1286 (1998);

[36] V.D. Burkov, F.A. Egorov, and V.T. Potapov, "Interaction of an erbium fiber-optic laser with a microresonator through a nonlinear Fabry-Perot interferometer", Tech. Phys. Lett. **22**, 738 (1996);

[37] R.A. Buser and N.F. Rooij, "Very high Q-factor resonators in monocrystalline silicon," Sensors and Actuators **A21-A23**, 323 (1990)

[38] K.E. Cahill and R.J. Glauber, "Density operators and quasiprobability distributions", Phys. Rev. **177**, 1882 (1969);

[39] C. M. Caves, "Quantum-mechanical radiation pressure fluctuations in an interferometer," Phys. Rev. Lett. **45**, 75 (1980);

[40] C. M. Caves, "Quantum-mechanical noise in an interferometer," Phys. Rev. D **23**, 1693 (1981);

[41] C. M. Caves, "Quantum limits on noise in linear amplifiers," Phys. Rev. D **26**, 1817 (1982);

[42] C. M. Caves and B.L. Schumaker, "New formalism for two-photon quantum optics," Phys. Rev. A **31**, 3068 (1985)

[43] M.A. Chan, S.D. Collins, and R.L. Smith, "A micromachined pressure sensor with fiber-optic interferometric readout", Sensors and Actuators A **43**, 196 (1994);

[44] S. Chang, A.G. Mann, A.N. Luiten, and D.G. Blair, "Measurements of radiation pressure effects in cryogenic sapphire dielectric resonators", Phys. Rev. Lett. **79**, 2141 (1997);

[45] C.-C. Chen and M. Z. Win, "Frequency noise measurement of diode-pumped Nd:YAG ring lasers", IEEE Phot. Tech. Lett. **2**, 772 (1990);

[46] A.V. Churenkov, "Photothermal excitation of mechanical microcavities by modulated optical radiation", Opt. Spectrosc. **72**, 825 (1992);

[47] A.N. Cleland and M.L. Roukes, "Fabrication of high frequency nanometer scale mechanical resonators from bulk Si crystals", Appl. Phys. Lett. **69**, 2653 (1996);

[48] A.N. Cleland and M.L. Roukes, "A nanometre-scale mechanical electrometer", Nature **392**, 160 (1998);

[49] M.J. Collett and C.W. Gardiner "Squeezing of intracavity and traveling-wave light fields produced in parametric amplification," Phys. Rev A **30**, 1386 (1984); M. J. Collett and D. F. Walls, "Squeezing spectra for nonlinear optical systems," Phys. Rev A **32**, 2887 (1985);

[50] M. Dakna, G. Breitenbach, J. Mlynek, T. Opatrný, S. Schiller, and D.-G. Welsch, "Homodyne measurements of quantum optical phase moments", to be published;

[51] G. M. D'Ariano, C. Macchiavello, and M. G. A. Paris, "Detection of the density matrix through optical homodyne tomography without filtered back projection," Phys. Rev. A **50**, 4298 (1994).

[52] G.M. D'Ariano, U. Leonhardt, and H. Paul, "Homodyne detection of the density matrix of the radiation field", Phys. Rev. A **52**, R1801 (1995)

[53] G.M. D'Ariano, "Homodyning as universal detection", in *Proc. Quant. Comm. and Meas. III*, ed. V.P. Belavkin, O. Hirota, and R.L. Hudson, Plenum Press, New York (1996);

[54] L. Davidovich, "Sub-Poissonian processes in quantum optics", Rev. Mod. Phys. **68**, 127 (1996)

[55] G. Delapierre, "Micro-machining: A survey of the most commonly used processes", Sensors and Actuators **17**, 123 (1989);

[56] W. Denk, W.W. Webb, and A.J. Hudspeth, "Mechanical properties of sensory hair bundles are reflected in their Brownian motion measured with a laser differential interferometer", Proc. Natl. Acad. Sci. USA **86**, 5371 (1989);

[57] V.V. Dodonov, O.V. Man'ko, and V.I. Man'ko, "Photon distribution for one-mode mixed light with a generic Gaussian Wigner function," Phys. Rev. A **49**, 2993 (1994);

[58] A. Dorsel, J.D. McCillen, P. Meystre, E. Vignes, and H. Walther, "Optical bistability and mirror confinement induced by radiation pressure", Phys. Rev. Lett. **51**, 1550 (1983);

[59] R. Drever, J.L. Hall, F. Kowalski, J. Hough, G. Ford, A. Munley and H. Ward "Laser phase and freequency stabilization using an optical resonator," Appl. Phys. B **31**, 97 (1983);

[60] T.J. Dunn, J.N. Sweetser, and I.A. Walmsley, "Experimental determination of the quantum-mechanical state of a molecular vibrational mode using fluorescence tomography," Phys. Rev. Lett. **74**, 884 (1995);

[61] W.A. Edelstein, J. Hough, J.R. Pugh, and W. Martin, "Limits to the measurement of displacement in an interferometric gravitational radiation detector", J. Phys. E **11**, 710 (1978);

[62] A. El Habti, A. Zarka, and F. Bastien, "Physical limitation on the quality factor of quartz resonators", J. Acoust, Soc. Am. **94**, 917 (1993);

[63] C. Fabre, M. Pinard, S. Bourzeix, A. Heidmann, E. Giacobino, S. Reynaud, "Quantum-noise reduction using a cavity with a movable mirror", Phys. Rev. A **49**, 1337 (1994);

[64] U. Fano, "Description of states in quantum mechanics by density matrix and operator techniques," Rev. Mod. Phys. **29** No.1, 74 (1957);

[65] T. Felbinger, S. Schiller, and J. Mlynek, "Oscillation in 3-photon down-conversion and generation of nonclassical states", Phys. Rev. Lett. **80**, 492 (1998);

[66] T. Felbinger, diploma thesis, Konstanz 1996;

[67] J. Ferreirinho, "Internal friction in high Q materials", in *The detection of gravitational waves*, Ed.: D.G. Blair, Cambridge University Press 1991;

[68] R.A. Fisher, M.M. Nieto, and V.D. Sandberg, "Impossibility of naively generalizing squeezed coherent states," Phys. Rev. A **29**, 1107 (1984)

[69] C. Freed and H.A. Haus, "Photoelectron statistics produced by a laser operating below the threshold of oscillation," Phys. Rev. Lett. **15**, 943 (1965)

[70] M. Freyberger, P. Bardroff, C. Leichtle, G. Schrade, and W. Schleich, "The art of measuring quantum states", Phys. World, Nov. 1997;

[71] S.R. Friberg, S. Machida, M.J. Werner, A. Levanon, and T.Mukai, "Observation of optical soliton photon-number squeezing", Phys. Rev. Lett. **77**, 3775 (1996);

[72] G.A. Garrett, A.G. Rojo, A.K. Sood, J.F. Whitaker, R. Merlin, "Vacuum squeezing of solids: Macroscopic quantum states driven by light pulses", Science **275**, 1638 (1997);

[73] D. Giulini, E. Joos, C. Kiefer, J. Kupsch, I.O. Stamatescu, and H.D. Zeh, *Decoherence and the appearance of a classical world in quantum theory*, Springer, Berlin 1996;

[74] R.J. Glauber, "The Quantum Theory of Optical Coherence," Phys. Rev. **130**, 2529 (1963); R.J. Glauber, "Coherent and Incoherent States of the Radiation Field," Phys. Rev. **131**, 2766 (1963);

[75] A. Gozzini, F. Maccarrone, F. Mango, I. Longo, and S. Barbarino, "Light-pressure bistability at microwave frequencies", J. Opt. Soc. B **2**, 1841 (1985);

[76] P. Grangier, R.E. Slusher, B. Yurke, and A. La Porta, "Squeezed-Light-Enhanced Polarization Interferometer," Phys. Rev. Lett. **59**, 2153 (1987);

[77] D.S. Greywall, B. Yurke, P.A. Busch, A.N. Pargellis, and R.L. Willett, "Evading amplifier noise in nonlinear oscillators", Phys. Rev. Lett. **72**, 2992 (1994);

[78] D.S. Greywall, B. Yurke, P.A. Busch, S.C. Arney, "Low-temperature anomalies in the dissipation of small mechanical resonators", Europhys. Lett. **34**, 37 (1996);

[79] W. Hai, X. Changde, P. Qing, X. Chengyang, Z. Yun, and P. Kunchi, "Optical measurements of weak absorption beyond shot-noise limit", to be published;

[80] W.O. Hamilton, "Near zero force, force gradient and temperature: Cryogenic bar detectors of gravitational radiation", in *Near zero*, ed. J.D. Fairbank, B.S. Deaver, C.W.E. Everitt, and P.F. Michelson, W.H. Freeman and Co., New York 1988;

[81] K. Hane and K. Suzuki, "Self-excited vibration of a self-supporting thin film caused by laser irradiation", Sensors and Actuators A **51**, 179 (1996);

[82] K. Hane, "Analytical modelling of micromachined resonator sensor activated by cw laser irradiation", Proc. Int. Conf. Solid-State Sensors and Actuators, Transducers'97, Chicago 1997;

[83] H. Hansen, presently in the lab, working; see also *http://quantum-optics.physik.uni-konstanz.de*;

[84] T. Hashimoto and T. Yoko, "Phase matching of rutile single crystal", Appl. Phys. Lett. **68**, 2478 (1996);

[85] C.C. Havener, N. Rouze, W.B. Westerfeld, and J.S. Risley, "Experimental determination of the density matrix describing collisionally produced H(n=3) atoms", Phys. Rev. A **33**, 276 (1986);

[86] A. Heidmann and S. Reynaud, "Photon noise reduction by reflection from a movable mirror," Phys. Rev. A **50**, 4237 (1994);

[87] C. Hettich, diploma thesis, Konstanz 1997;

[88] L. Hilico, J.M. Courty, C. Fabre, E. Giacobino, I. Abram, and J.L. Oudar, "Squeezing in $\chi^{(3)}$ materials", Appl. Phys. B, **55**, 202 (1992);

[89] M. Hillery, R.F. O'Connell, M.O. Scully and E.P. Wigner, "Distribution functions in physics: fundamentals," Phys. Rep. 106 (1984) 121.

[90] M. Hillery, "Photon number divergence in the quantum theory of n-photon down conversion," Phys. Rev. A **42**, 498 (1990)

[91] D. Hils and J.L. Hall, "Response of a Fabry-Perot cavity to phase modulated light", Rev. Sci. Instrum. **58**, 1406 (1987);

[92] T. Hirano and M. Matsuoka, "Generation of broadband squeezed states pumped by cw mode-locked pulses", Appl. Phys. B **55**, 233 (1992);

[93] A.S. Holevo, Probabilistic and statistical aspects of quantum theory (North-Holland, Amsterdam, 1982); A.S. Holevo, in Quantum Probability and Applications to the Quantum Theory of Irreversible Processes, edited by L. Accardi, A. Frigerio, and V. Gorini, Springer Lect. Notes Math. Vol. 1055 (Springer-Verlag, Berlin, 1984), p. 153;

[94] M. Hollenhorst, "Quantum limits on resonant-mass gravitational-radiation detectors", Phys. Rev. D **19**, 1669 (1979);

[95] C.K. Hong and L. Mandel, "Higher-order squeezing of a quantum field", Phys. Rev. Lett. **54**, 323 (1985)

[96] Z. Hradil, "Quantum state estimation", Phys. Rev. A **55**, R1561 (1997);

[97] A.J. Hudspeth and V.S. Marklin, "The ear's gears: Mechanoelectrical transduction by hair cells", Phys. Today, p.22 Feb.1994;

[98] Interferometric gravitational wave detectors:
ACIGA: www.anu.edu.au/physics/aciga
GEO600: www.geo600.uni-hannover.de
LIGO: www.ligo.caltech.edu
LISA: www.lisa.uni-hannover.de
TAMA300: www.tamago.mtk.nao.ac.jp
VIRGO: www.pi.infn.it/virgo
see also G. Schäfer and B. Schutz, "Gravitational physics", Physics World, December 1996;

[99] V.P. Jaecklin, C. Linder, J. Brugger, N.F. de Rooij, J.M. Moret, and R. Vuilleumier, "Mechanical and optical properties of surface micromachined torsional mirrors in silicon, polysilicon, and aluminum", Sensors and Actuators A **43**, 269 (1994);

[100] Jaehne, *Digitale Bildverarbeitung*, Chap. 11 (1989);

[101] M.T. Jaekel and S. Reynaud, "Quantum limits in interferometric measurements", Europhys. Lett **13**, 301 (1990);

[102] U. Janicke and M. Wilkens, "Tomography of atom beams," J. Mod. Opt. **42**, 2183 (1995)

[103] F. Jaramillo, V.S. Marklin, and A.J. Hudspeth, "Auditory illusions and the single hair cell", Nature **364**, 527 (1993);

[104] S. Jiang, S. Machida, Y. Takiguchi, H. Cao, and Y. Yamamoto, "Wide band AC balanced homodyne detection of weak coherent pulses", Opt. Comm. **145**, 91 (1998);

[105] M. Johnson, 'Optical-actuator frequency-coded pressure sensor", Opt. Lett. **11**, 587 (1986);

[106] L. Ju, M. Notcutt, D. Blair, F. Bondu, and C.N. Zhao, "Sapphire beamsplitters and test masses for advanced laser interferometer gravitational wave detectors", Phys. Lett. A **218**, 197 (1996);

[107] K. Kasai, G. Jiangrui, and C. Fabre, "Observation of squeezing using cascading nonlinearity", Europhys. Lett. **40**, 25 (1997);

[108] K. Kawabe, S. Nagataki, M. Ando, K. Tochikubo, N. Mio, and K. Tsubono, "Demonstration of a recombined Fabry-Perot-Michelson interferometer with suspended mirrors", Appl. Phys. B **62**, 135 (1996);

[109] E.H. Kennard, Zeit. Phys. **44**, 326 (1996), Sec. 4C;

[110] S.H. Kienle, D. Fischer, W.P. Schleich, V.P. Yakovlev, and M. Freyberger, "Reconstructing quantum states via quantum tomography and atom interferometry", Appl. Phys. B **65**, 735 (1997);

[111] K. Kim and T. Kim, "Relationship between squeezing and sub-poissonian statistics", Phys. Lett. A **125**, 83 (1987)

[112] C. Kim and P. Kumar, "Quadrature-squeezed light detection using a self-generated matched local oscillator", Phys. Rev. Lett. **73**, 1605, 1994;

[113] H.J. Kimble, M. Dagenais, and L. Mandel, "Photon antibunching in resonance fluorescence," Phys. Rev. Lett. **39**, 691 (1977);

[114] M.S. Kim, F.A.M. Oliveira, and P.L. Knight, "Properties of squeezed number states and squeezed thermal states", Phys. Rev. A **40**, 2494 (1989);

[115] H.J. Kimble, "Quantum Fluctuations in Quantum Optics - Squeezing and Related Phenomena," Les Houches summer school 1990

[116] P. Kinsler and P.D. Drummond, "Quantum dynamics of the parametric oscillator", Phys. Rev. A **43**, 6194 (1991);

[117] T. Kiss, U. Herzog, and U. Leonhardt, "Compensation of losses in photodetection and in quantum-state measurements", Phys. Rev. A **52**, 2433 (1995)

[118] R.N. Kleiman, G.K. Kaminsky, J.D. Reppy, R. Pindak, and D.J. Bishop, "Single-crystal silicon high-Q torsional oscillators", Rev. Sci. Instr. **56**, 2088 (1985);

[119] R.N. Kleiman, G. Agnolet, and D.J. Bishop, "Two-level systems observed in the mechanical properties of single-crystal silicon at low temperatures", Phys. Rev. Lett. **59**, 2079 (1987);

[120] M. Koashi, K. Kono, T. Hirano, and M. Matsuoka, "Photon antibunching in pulsed squeezed light generated via parametric amplification," Phys. Rev. Lett. **71**, 1164 (1993);

[121] H. Kobayashi, H. Kanbara, and M. Koga, "Third-order nonlinear optical properties of As_2S_3 chalcogenide glass," J. Appl. Phys. **74**, 3683 (1993);

[122] H. Kogelnik and T. Li, "Laser Beams and Resonators," Appl. Opt. **5**, 1550 (1966);

[123] D.S. Krähmer and U. Leonhardt, "State reconstruction of one-dimensional wave packets", Appl. Phys. B **65**, 725 (1997);

[124] L. Krippner, W. J. Munro, and M. D. Reid, "Transient Macroscopic Quantum Superposition States in Degenerate Parametric Oscillation", Phys. Rev. A **50**, 4330 (1994);

[125] K. Kubodera and H. Kobayashi, "Determination of third-order nonlinear optical susceptibilities for organic materials by third harmonic generation," Mol. Cryst. Liq. Cryst. **182A**, 103 (1990); T. Kurihara, H. Kanbara, H. Kobayashi, K. Kubodera, S. Matsumoto, and T. Kaino, "Third-order nonlinear optical properties of DEANST: a new material for nonlinear optics," Opt. Comm. **84**, 149 (1991);

[126] C. Kurtsiefer, T. Pfau, and J. Mlynek, "Measurement of the Wigner function of an ensemble of helium atoms", Nature, **386**, 150 (1997);

[127] W.E. Lamb, "Anti-photon", Appl. Phys. B **60**, 77 (1995);

[128] T.S.J. Lammerink, M. Elwenspoek, R.H. van Ouwerkerk, S. Bouwstra, and J.H.J. Fluitman, "Performance of thermally excitated resonators", Sensors and Actuators **A21-A23**, 352 (1990);

[129] T.S.J. Lammerink, M. Elwenspoek, and J.H.J. Fluitman, "Optical excitation of micro-mechanical resonators", Proc. IEEE Micro Electro Mechanical Systems Cat.No.91CH2957-9, p.160 (1991);

[130] Landolt-Börnstein, New Series III/22a, *Semiconductors: Intrinsic properties of group IV elements*;

[131] R.M. Langdon and D.L. Dowe, "Photoacoustic oscillator sensors", Proc. SPIE **798** Fiber Optic Sensors, 86 (1987);

[132] D. Leibfried, D.M. Meekhof, B.E. King, C. Monroe, W.M. Itano, and D.J. Wineland, "Experimental determination of the motional quantum state of a trapped atom", Phys. Rev. Lett. **77**, 4281 (1996);

[133] F. Le Kien, A.V. Chizhov, W.P. Schleich, G. Breitenbach, S. Schiller, and J. Mlynek, "Asymptotology of squeezed thermal states", to be published

[134] U. Leonhardt and H. Paul, "Realistic optical homodyne measurements and quasiprobability distributions," Phys. Rev. A 48, 4598 (1993);

[135] U. Leonhardt, M. Munroe, T. Kiss, Th. Richter, and M.G. Raymer, "Sampling of photon statistics and density matrix using homodyne detection," Opt. Comm. **127**, 144 (1996);

[136] U. Leonhardt and M.G. Raymer, "Observation of moving wave packets reveals their quantum state", Phys. Rev. Lett. **76**, 1985 (1996);

[137] U. Leonhardt, *Measuring the quantum state of light*, Cambridge University Press, Cambridge 1997;

[138] M. Ley and R. Loudon, "Quantum theory of high-resolution length measurement with a Fabry-Perot interferometer", J. Mod. Opt. **34**, 227 (1987);

[139] LIGO interferometer: A. Abramovici et al., "LIGO: the Laser Interferometer Gravitational-Wave Observatory", Science, **256**, 325 (1992); A. Abramovici et al., "Improved sensitivity in a gravitational wave interferometer and implications for LIGO", Phys. Lett. A **218**, 157 (1996);

[140] R. Loudon, *The quantum theory of light*, Oxford 1973;

[141] R. Loudon, "Quantum limit on the Michelson interferometer used for gravitational wave detection", Phys. Rev. A **47**, 815 (1981);

[142] L.A. Lugiato and A. Gatti, "Spatial structure of squeezed vacuum", Phys. Rev. Lett. **70**, 3868 (1992);

[143] A. Luis and L.L. Sanches-Soto, "Multimode quantum analysis of an interferometer with moving mirrors", Phys. Rev. A **45**, 8228 (1992);

[144] A.N. Luiten, A.G. Mann, and D.G. Blair, "Ultrahigh Q-factor cryogenic sapphire resonator", Electr. Lett. **29**, 879 (1993);

[145] R. Lynch, "The quantum phase problem: a critical review", Phys. Rep. **256**, 367 (1995);

[146] S. Machida, Y. Yamamoto, and Y. Itaya, "Observation of amplitude squeezing in a constant-current-driven semiconductor laser," Phys. Rev. Lett. **58**, 1000 (1987);

[147] E. Majorana, P. Puppo, P. Rapagnani and F. Ricci, "Observation of the Brownian motion of a mechanical oscillator by means of a back action evading system", Appl. Phys. B **64**, 145 (1997);

[148] S. Mancini and P. Tombesi, "Quantum noise reduction by radiation pressure", Phys. Rev. A **49**, 4055 (1994);

[149] L. Mandel, "Squeezed states and sub-poissonian photon statistics", Phys. Rev. Lett. **49**, 136 (1982);

[150] L. Mandel and E. Wolf, *Optical coherence and quantum optics*, Cambridge University Press, Cambridge 1995;

[151] P. Marian and T.A. Marian, "Squeezed states with thermal noise", Phys. Rev A **47**, 4474 (1993);

[152] O. Marti, A. Ruf, M. Hipp, H. Bielefeldt, J. Colchero, and J. Mlynek, "Mechanical and thermal effects of laser irradiation in force microscope cantilevers", Ultramicroscopy **42-44**, 345 (1992);

[153] A.B. Matsko, E.A. Zubova, and S.P. Vyatchanin, "The value of the force of radiative friction", Opt. Comm. **131**, 107 (1996);

[154] D.F. McAlister and M.G. Raymer, "Ultrafast photon-number correlations from dual-pulse, phase-averaged homodyne detection", Phys. Rev. A **55**, R1609 (1997);

[155] D.F. McGuigan, C.C. Lam, R.Q. Gram, A.W. Hoffman, and D.H. Douglass, "Measurements of the mechnical Q of single-crystal silicon at low temperatures", J. of Low Temp. Phys. **30**, 621 (1978)

[156] D.M. Meekhof, C. Monroe, B.E. King, W.M. Itano, and D.J. Wineland, "Generation of nonclassical motional states of a trapped atom," Phys. Rev. Lett. **76**, 1796 (1996);

[157] P. Meystre, E.M. Wright, J.D. McCullen, and E. Vignes, "Theory of radiation-pressure-driven interferometers", J. Opt. Soc. Am. B **2**, 1830 (1985);

[158] R.E. Mihailovich and J.M. Papria, "Anomalous low temperature mechanical properties of single-crystal silicon", Physica B **165/166**, 125 (1990);

[159] G.J. Milburn and D.F. Walls, "Effect of dissipation on interference in phase space," Phys. Rev. A **38**, 1087 (1988);

[160] G. J. Milburn, K. Jacobs and D. F. Walls, "Quantum-limited measurements with the atomic force microscope", Phys. Rev. **A 50**, 5256 (1994);

[161] B.R. Mollow and R.J. Glauber, "Quantum theory of parametric amplification," Phys. Rev. bf 160, 1076 (1967);

[162] T. Müller, T. Feichtinger, G. Breitenbach, M. Brandl, O. Brand, and H. Baltes, "Industrial fabrication method for arbitrarily shaped silicon n-well micromechanical structures", Proceedings IEEE 11th Annual International Workshop on Micro Electro Mechanical Systems, Heidelberg, (1998);

[163] M. Munroe, D. Boggavarapu, M.E. Anderson, and M.G. Raymer, "Photon statistics from the phase-averaged quadrature field distribution: theory and ultrafast measurement," Phys. Rev. A **52**, R924 (1995);

[164] K. Nakagawa, A.S. Shelkovnikov, T. Katsuda, and M. Ohtsu, "Fast frequency stabilisation of a diode-laser-pumped monolithic Nd:YAG laser with an extra-cavity electro-optic modulator", Opt. Comm. **109**, 446 (1994);

[165] R. Nath and P. Kumar, "Phase properties of squeezed thermal states", J. mod. Opt. **43**, 7 (1996);

[166] F. Natterer, *The Mathematics of Computerized Tomography*, Wiley, New York, (1986);

[167] E. Nelson, "Derivation of the Schrödinger equation from Newtonian mechanics", Phys. Rev. **150**, 1079 (1966);

[168] M.M. Nieto, "Displaced and squeezed number states", Phys. Lett. A **229**, 135 (1997);

[169] J.W. Noh, A. Foug'eres, and L. Mandel, "Measurement of the quantum phase by photon counting," Phys. Rev. Lett. **67**, 1426 (1991);

[170] M. Okada, "Third-order nonlinear optical coefficients of $LiIO_3$", Appl. Phys. Lett. **18**, 451 (1971);

[171] T. Opatrný, "Number-phase uncertainty relations", J. Phys. A **28**, 6961 (1995);

[172] T. Opatrný, D.-G. Welsch, and W. Vogel, "Least-squares inversion for density-matrix reconstruction", Phys. Rev. A **56**, 1788 (1997);

[173] T. Opatrný, M. Dakna, and D.-G. Welsch, "Number-phase uncertainty relations: Verification by balanced homodyne measurement", Phys. Rev. A **57**, 2129 (1998);

[174] Z.Y. Ou and H.J. Kimble, "Probability distribution of photoelectric currents in photodetection processes and its connection to the measurement of a quantum state," Phys. Rev. A **52**, 3126 (1995);

[175] A. F. Pace, M. J. Collett and D. F. Walls, "Quantum limits in interferometric detection of gravitational radiation", Phys. Rev. A **47**, 3173 (1993);

[176] Y. Pang and J.-P. Richard, "Room-temperature tests of an optical transducer for resonant gravitational wave detection", Appl. Opt. **34**, 4982 (1995);

[177] R. Paschotta, K. Fiedler, P. Kürz, R. Henking, S. Schiller, and J. Mlynek, "82 % efficient cw frequency-doubling of 1.06 μm using a monolithic $MgO:LiNbO_3$ resonator", Opt. Lett. **19**, 1325 (1994);

[178] H. Paul, P. Törmä, T. Kiss, and I. Jex, "Photon chopping: A new way to measure the quantum state of light", Phys. Rev. Lett. **76**, 2464 (1996);

[179] D.T. Pegg and S.M. Barnett, "Phase properties of the quantized single-mode electromagnetic field", Phys. Rev. A **39**, 1665 (1989); D.T. Pegg and S.M. Barnett, "Tutorial review Quantum optical phase", J. Mod. Opt. **44**, 225 (1997);

[180] K.E. Petersen, "Silicon as a mechanical material", Proc. IEEE **70**, 420 (1982);

[181] M. Pierre, J.B. Ehooman, G.R. Neergaard, J.L. Coutaz, and I. Ledoux, "Phase matched third harmonic generation from organic crystal of 4-aminobenzonitrile," Opt. Comm. **98**, 209 (1993);

[182] R.J. Pitcher, K.W.H. Foulds, J.A. Clements, and J.M. Naden "Optothermal drive of silicon resonators: The influence of surface coatings", Sensors and Actuators **A21-A23**, 387 (1990);

[183] F. Pobell, *Matter and methods at low temperatures*, Springer, Berlin 1992;

[184] E. S. Polzik, J. Carri, and H. J. Kimble, "Spectroscopy with squeezed light," Phys. Rev. Lett. **68**, 3020 (1992); E. S. Polzik, J. Carri, and H. J. Kimble, "Atomic spectroscopy with squeezed light for sensitivity beyond the vacuum-state limit," Appl. Phys. B **55**, 279 (1992)

[185] W.H. Press, B.P. Flannery, S.A. Teukolsky, and W.T. Vetterling, *Numerical recipes*, Cambridge University Press, Cambridge 1989;

[186] P. Qiu and A. Penzkofer, "Picosecond third-harmonic light generation in β-BaB_2O_4," Appl. Phys. B **45**, 225 (1988);

[187] H. Puell, K. Spanner, W. Falkenstein, W. Kaiser, and C.R. Vidal, "Third-harmonic generation of mode-locked Nd:glass pulses in phase-matched Rb-Xe mixtures", Phys. Rev. A **14**, 2240 (1976);

[188] J. Radon, Berichte der sächsischen Akademie der Wissenschaften, Leipzig, Math.-Phys. Kl. **69**, 262-267 (1917);

[189] J.G. Rarity, P.R. Tapster, and E. Jakeman, "Observation of sup-Poissonian light in parametric downconversion," Opt. Comm. **62**, 201 (1987);

[190] Y.J. Rao and B. Culshaw, "Comparison between optically excited vibrations of silicon cantilever and bridge microresonators", Sensors and Actuators A **30**, 203 (1992);

[191] M. G. Raymer, J. Cooper, H. J. Carmichael, M. Beck and D. T. Smithey, "Ultrafast measurement of optical-field statistics by dc-balanced homodyne detection," J. Opt. Soc. Am. B **12**, 1801 (1995);

[192] M.G. Raymer, D.F. Mc Alister, and U. Leonhardt, "Two-mode quantum optical state measurement: Sampling the joint density matrix", Phys. Rev. A **54**, 2397 (1996);

[193] M.G. Raymer, D.T. Smithey, M. Beck, M. Anderson, and D.F. McAlister, Proc. III. intern. Wigner Symp., Oxford 1993, to appear in J. of Mod. Physics B;

[194] M. Roukes, private communication, Pasadena 1997;

[195] D. Rugar, private communication, San José 1997;

[196] Review articles on squeezed states: D.F. Walls, "Squeezed states of light," Nature **306**, 141 (1983); R. Loudon and P.L. Knight, "Squeezed light", J. Mod. Opt. **34**, 709 (1987); G. Leuchs, "Squeezing the quantum fluctuations of light", Contemp. Phys. **29**, 299 (1988); M.C. Teich and B.E.A. Saleh, "Squeezed states of light", Quantum Opt. **1**, 153 (1989);

[197] Review articles on miniature silicon sensors: R.M. Langdon, "Resonator sensors - a review", J. Phys. E: Sci. Instr. **18**, 103 (1985); J.C. Greenwood, "Silicon in mechanical sensors", J. Phys. E: Sci. Instr. **21**, 1114 (1988); G. Stemme, "Resonant silicon sensors", J. Micromech. Microeng. **1**, 113 (1991); M. Elwenspoek, "Micromechanical resonant sensors", Journal A, **32**, 15 (1991); D.S. Greywall, "Micromechanical light modulators, pressure gauges, and thermometers attached to optical fibers", J. Micromech. Microeng. **7**, 343 (1997);

[198] W. Richardson, S. Machida, Y. Yamamoto, "Squeezed Photon-Number Noise and Sub-Poissonian Electrical Partition Noise in a Semiconductor Laser," Phys. Rev. Lett. **68** (1992);

[199] Th. Richter, "Pattern functions used in tomographic reconstruction of photon statistics revisited", Phys. Lett. A **211**, 327 (1996);

[200] Th. Richter and A. Wünsche, "Determination of occupation probabilities from time-averaged position distributions", Phys. Rev. A **53**, R1974 (1996);

[201] D.I. Robertson, E. Morrison,. J. Hough, S. Kilbourn, B.J. Meers, G.P. Newton, N.A. Robertson, K.A. Strain, and H. Ward, "The Glasgow 10 m prototype laser interferometric gravitational wave detector", Rev. Sci. Instr. **66**, 4447 (1995);

[202] L. Robles, M.A. Ruggero, and N.C. Rich, "Two-tone distortion in the basilar membrane of the cochlea", Nature **349**, 413 (1991);

[203] T.V. Roszhart, "The effect of thermoelastic friction on the Q of micromachined silicon resonators", IEEE Solid-State Sensors and Actuators Workshop 1990, p. 13;

[204] A. Royer, "Measurement of quantum states and the Wigner function", Found. Phys. **19**, 3 (1989);

[205] D. Rugar, H.J. Mamin, and P. Grüttner, "Improved fiber-optic interferometer for atomic force microscopy", Appl. Phys. Lett. **55**, 2588 (1989); D. Rugar, C.S. Yannoni, and J.A. Sidles, "Mechanical detection of magnetic resonance", Nature **360**, 563 (1992); D. Rugar, O. Züger, S. Hoen, C.S. Yannoni, H.M. Vieth, and R.D. Kendrick, "Force detection of nuclear magnetic resonance", Science **264**, 1560 (1994);

[206] D. Rugar and P. Grüttner, "Mechanical parametric amplification and thermomechanical noise squeezing," Phys. Rev. Lett. **67**, 699 (1991);

[207] J.B. Sampsell, "Digital micromirror device and its application to projection displays", J. Vac. Sci. Technol. B **12**, 3242 (1994);

[208] M. Sargent, M.O. Scully, and W.E. Lamb, *Laser Physics*, Addison-Wesley, Reading 1974 (chapt. 18);

[209] D.W. Satchell and J.C. Greenwood, "A thermally excited silicon accelerometer", Sensors and Actuators **17**, 241 (1989);

[210] M.V. Satyanarayana, "Generalized coherent states and generalized squeezed coherent states", Phys. Rev. D **32**, 400 (1985);

[211] P.R. Saulson, "Thermal noise in mechanical experiments", Phys. Rev. D **42**, 2437 (1990);

[212] S. Schiller, S. Kohler, R. Paschotta, and J. Mlynek, "Squeezing and Quantum Non-Demolition Measurements with an Optical Parametric Amplifier," Appl. Phys. B **60**, S77 (1995);

[213] S. Schiller, G.Breitenbach, R. Paschotta und J. Mlynek, "Subharmonic-pumped continuous-wave parametric oscillator," Appl. Phys. Lett. **68**, 3374 (1996);

[214] W. Schleich and J.A. Wheeler, "Oscillations in photon distribution of squeezed states and interference in phase space," Nature **326**, 574 (1987);

[215] W. Schleich and J.A. Wheeler, "Oscillations in photon distribution of squeezed states," J. Opt. Soc. Am. B **4** No 10, 1715 (1987);

[216] W. Schleich, D.F. Walls, and J.A. Wheeler, "Area of Overlap and interference in phase space versus Wigner pseudoprobabilities," Phys. Rev. A **38** No 3, 1177 (1988);

[217] W. Schleich, R.J. Horowicz, and S. Varro, "Bifurcation in the phase probability distribution of a highly squeezed state", Phys. Rev. A **40**, R7405 (1989);

[218] W.P. Schleich, E. Mayr, D. Krähmer, *Quantum Optics in Phase Space*, Wiley, Weinheim 1998;

[219] K. Schneider, diploma thesis, Konstanz 1995;

[220] K. Schneider, P. Kramper, S. Schiller, and J. Mlynek, "Toward an optical synthesizer: a single-frequency parametric oscillator using periodically poled $LiNbO_3$", Opt. Lett. **22**, 1293 (1997);

[221] K. Schneider, M. Lang, J. Mlynek, and S. Schiller, "Generation of strongly squeezed light at 1064 nm," Opt. Express **2**, 59 (1998);

[222] E. Schrödinger, "Der stetige Übergang von der Mikro- zur Makromechanik", Die Naturwiss. **28**, 665 (1926);

[223] B. Schumaker, "Noise in Homodyne Detection," Opt. Lett. **19**, 189 (1984);

[224] R.M. Shelby, M.D. Levenson, S.H. Perlmutter, R.G. DeVoe, and D.F. Walls, "Broad-band parametric deamplification of quantum noise in an optical fiber", Phys. Rev. Lett. **57**, 691 (1986);

[225] R. Short and L. Mandel, "Observation of sub-Poissonian photon statistics," Phys. Rev. Lett. **51**, 384 (1983);

[226] A. E. Siegman, *Lasers*, Science Books, Mill Valley, 1986;

[227] R.E. Slusher, L.W. Hollberg, B. Yurke, J.C. Mertz, and J.F. Valley, "Observation of squeezing by four wave mixing in a cavity," Phys. Rev. Lett. **55**, 2409 (1985);

[228] D.T. Smithey, M. Beck, M. Belsey, and M.G. Raymer, "Sub-shot-noise correlation of total photon number using macroscopic twin pulses of light," Phys. Rev. Lett. **69**, 2650 (1992);

[229] D.T. Smithey, M. Beck, M.G. Raymer, A. Faridani, "Measurement of the Wigner Distribution and the Density Matrix of a Light Mode using Optical Homodyne Tomography: Application to Squeezed States and the Vacuum" Phys. Rev. Lett. **70**, 1244 (1993); D. T. Smithey, M. Beck, J. Cooper, M. G. Raymer and A. Faridani, "Complete experimental characterization of the quantum state of a light mode ...", Phys. Scr. T **48**, 35 (1993);

[230] D.T. Smithey, M. Beck J. Cooper, and M.G. Raymer, "Measurement of number-phase uncertainty relations of optical fields," Phys. Rev. A **48**, 3159 (1993);

[231] S. Spälter, M. Burk, U. Strössner, M. Böhm, A. Sizmann, and G. Leuchs, "Photon number squeezing of spectrally filtered sub-picosecond optical pulses", Europhys. Lett. **38**, 335 (1997);

[232] Special issues on squeezed states of light: J. Opt. Soc. Am. B **4** (1987), J. Mod. Opt. **34** (1987); special issue on quantum noise reduction in optical systems: Appl. Phys. B **55**, n.3 (1992);

[233] Special issue on quantum state preparation and measurement, J. Mod. Opt. **44** number 11/12 (1997);

[234] N.A.D. Stokes, R.M.A. Fatah, and S. Venkatesh, "Self-excited vibrations of optical microresonators", Electr. Lett. **24**, 777 (1988);

[235] D. Stoler, "Equivalence classes of minimum uncertainty packets I,II," Phys. Rev. D **1**, 3217 (1970); Phys. Rev. D **4**, 1925 (1971);

[236] T.D. Stowe, K. Yasumura, T.W. Kenny, D. Botkin, K.Wago, and D. Rugar, "Attonewton force detection using ultrathin silicon cantilevers", Appl. Phys. Lett. **71**, 288 (1997);

[237] L. Susskind and J. Glogower, Physics **1**, 49 (1964);

[238] I. Szabo, *Höhere technische Mechanik*, Springer, Berlin (1977);

[239] I. Szabo, *Einführung in die technische Mechanik*, Springer, Berlin (1984);

[240] H. Takahasi, "Information theory of quantum mechanical channels", Adv. Comm. Systems **1**, 227 (1965);

[241] S.M. Tan, "An inverse problem approach to optical homodyne tomography", J. Mod. Opt. **44**, 2233 (1997);

[242] M.C. Teich and B.E.A. Saleh, "Observation of sub-Poisson Franck-Hertz light at 253.7 nm," J. Opt. Soc. B **2**, 275 (1985);

[243] K. Terashima, S.H. Kim, and T. Yoko, "Nonlinear Optical Properties of B_2O_3-based glasses," J. Am. Ceram. Soc. **78**, 1601 (1995);

[244] K.E.B. Thornton, D. Uttamchandani, and B. Culshaw, "Temperature dependence of resonant frequency in optically excited diaphragms", Electr. Lett. **22**, 1232 (1986); K.E.B. Thornton, D. Uttamchandani, and B. Culshaw, "Novel optically excited resonant pressure sensor", Electr. Lett. **24**, 573 (1988);

[245] I. Tittonen, G. Breitenbach, T. Kalkbrenner, T. Müller, R. Conradt, S. Schiller, E. Steinsland, N. Blanc, and N.F. Rooij, "Interferometric measurements of the position of a macroscopic body: towards observation of quantum limits," to appear in Phys. Rev. A;

[246] I. Tittonen, K. Jacobs, and H.M. Wiseman, "Quantum noise in the position measurement of a cavity mirror undergoing Brownian motion", in preparation;

[247] M.E. Tobar, E.N. Ivanov, D.K.L. Oi, B.D. Cuthbertson, and D.G. Blair, "Sapphire test-masses for measuring the standard quantum limit and achieving quantum non-demolition", Appl. Phys. B **64**, 153 (1997);

[248] I.V. Tomov, B. van Wonterghem, and P.M. Rentzepis, "Third harmonic generation in barium borate", Appl. Opt. **31**, 4172 (1992);

[249] S. Traeger, B. Willke, and K. Danzmann, "Monolithically suspended fused silica substrates with very high mechanical Q", Phys. Lett. A**225**, 39 (1997);

[250] K. Tsubono and S. Moriwaki, "Shot-noise limited low-frequency intensity noise of a Nd:YAG laser", Jpn. J. Appl. Phys. **31**, 241 (1992);

[251] Y. Uenishi, M. Tsugai, and M. Mehregany, "Micro-opto-mechanical devices fabricated by anisotropic etching of (110) silicon", J. Micromech. Microeng. **5**, 305 (1995);

[252] G.E. Uhlenbeck and L.S. Ornstein "On the theory of Brownian motion", Phys. Rev. **36**, 823 (1930);

[253] W.G. Unruh, "Quantum noise in the interferometer detector", in *Quantum Optics, Experimental Gravitation and Measurement Theory*, ed. by P. Meystre and M. O. Scully, Plenum, New York, 1983, p. 647;

[254] D. Uttamchandani, Z.N. Li, L.M. Zhang, and B. Culshaw, "All-fibre optical system for exciting and detecting the vibration of silicon microresonator systems", Opt. and Lasers in Engineering **16**, 119 (1992);

[255] J.A. Vaccaro and D.T. Pegg, "Phase properties of squeezed states of light," Opt. Comm. **70**, 529 (1998);

[256] J.A. Vaccaro, "New Wigner function for number and phase," Opt. Comm. **113**, 421 (1995);

[257] O. Veits and M. Fleischauer, "Quantum fluctuations in the optical parametric oscillator in the limit of a fast decaying subharmonic mode", Phys. Rev. A **52**, R4344 (1995);

[258] S. Venkatesh and S. Culshaw, "Optically activated vibrations in a micromachined silica structure", Electr. Lett. **21**, 315 (1985); S. Venkatesh and S. Novak, "Micromechanical resonators in fiber-optic systems", Opt. Lett. **12**, 129 (1987);

[259] K. Vogel and H. Risken, "Determination of quasiprobability distributions in terms of probability distributions for the rotated quadrature phase," Phys. Rev. A **40**, 2847 (1989);

[260] R. Vyas and S. Singh, "Exact quantum distribution for parametric oscillators", Phys. Rev. Lett. **74**, 2208 (1995);

[261] S.P. Vyatchanin and E.A. Zubova, "On the quantum limit for resolution in force measurement in interferometric optical transducers of displacement", Opt. Comm. **111**, 303 (1994); S.P. Vyatchanin and E.A. Zubova, "Quantum variation measurement of a force", Phys. Lett. A **201**, 269 (1995);

[262] K.Wago, O. Züger, R.D. Kendrick, C.S. Yannoni, and D. Rugar, "Low-temperature magnetic resonance force detection", J. Vac. Sci. Technol. B **14**, 1197 (1996);

[263] N.G. Walker and J.E. Carroll, "Simultaneous phase and amplitude measurements on optical signals using a multiport junction," Electr. Lett. **20**, 981 (1984); N.G. Walker, "Quantum theory of multiport optical homodyning", J. Mod. Optics **34**, 15 (1987);

[264] S. Wallentowitz and W. Vogel, "Unbalanced homodyning for quantum state measurements", Phys. Rev. A **53**, 4528 (1996);

[265] D.F. Walls and G.J. Milburn, "Effect of dissipation on quantum coherence," Phys. Rev. A **31**, 2403 (1985);

[266] D.F. Walls, G.J. Milburn, *Quantum Optics*, Springer Berlin (1994);

[267] *Selected papers on noise and stochastic processes*, ed. N. Wax, Dover Publications, New York 1954;

[268] A.G. White, private communication, Konstanz 1995;

[269] A.G. White, J. Mlynek, and S. Schiller, "Cascaded second-order nonlinearity in an optical cavity," Europhys. Lett. **35**, 425 (1996);

[270] B.E. White, Jr. and R. O. Pohl, "Internal friction of subnanometer α-SiO_2 films", Phys. Rev. Lett. **75**, 4437 (1995);

[271] B.E. White, "Elastic properties of amorphous thin films", Ph.D. Thesis, Cornell University, Ithaca (1996);

[272] E. P. Wigner, "On the Quantum Correction for Thermodynamic Equilibrium," Phys. Rev. **40**, 749 (1932);

[273] H. Wölfelschneider, R. Kist, G. Knoll, S. Ramakrishnan, H. Höflin, W. Benecke, L. Csepregi, A. Heuberger, and H. Seidel, "Optically excited and interrogated micromechanical silicon cantilever structure", SPIE Vol. 798 Fiber Optic Sensors II, 61 (1987); M. Hildebrand and H. Wölfelschneider, "Micromechanical structures excited by noise-modulated light via optical fibers", SPIE Vol. 1011 Fiber Optic Sensors III, 95 (1988);

[274] M. Wolinsky and H.J. Carmichael, "Quantum noise in the parametric oscillator: From squeezed states to coherent-state superposition," Phys. Rev. Lett. **60**, 1836 (1988);

[275] N.C. Wong, K.W. Leong, and J.H. Shapiro, "Quantum correlation and absorbtion spectroscopy in an optical parametric oscillator in the presence of pump noise", Opt. Lett. **15**, 891 (1990);

[276] L.-A. Wu, H.J. Kimble, J.L. Hall and H. Wu, "Generation of squeezed states by parametric down conversion," Phys. Rev. Lett. **57**, 691 (1986); L.-A. Wu, M. Xiao, and H.J. Kimble, "Squeezed states of light from an optical parametric oscillator," J. Opt. Soc. Am. **4**, 1465 (1987);

[277] S.-W. Xie, X.-L. Yang, W.-Y. Jia, and Y.-L. Chen, "Phase matched third harmonic generation in biaxial crystals," Opt. Comm. **118**, 648 (1995);

[278] M. Xiao, L. A. Wu, H. J. Kimble, "Precision Measurement beyond the Shot-Noise Limit," Phys. Rev. Lett. **59**, 298 (1987);

[279] A. Yariv, P. Yeh, *Optical waves in Crystals*, John Wiley & Sons (1984); A. Yariv, *Quantum Electronics*, John Wiley & Sons (1988);

[280] H.P. Yuen, "Two-photon coherent states of the radiation field," Phys. Rev. A **13**, 2226 (1976);

[281] H. P. Yuen and V. W. S. Chan, "Noise in Homodyne and Heterodyne Detection," Opt. Lett.**18**, 177 (1983);

[282] J.F. Young, G.C. Bjorklund, A.H. Kung, R.B. Miles, and S.E. Harris, "Third-harmonic generation in phase-matched Rb vapor," Phys. Rev. Lett. **27**, 1551 (1971);

[283] B. Yurke, "Squeezed-coherent-state generation via four-wave mixing and detection via homodyne detectors," Phys. Rev. A **32**, 300 (1985);

[284] B. Yurke and D. Stoler "Measurement of amplitude probability distributions for photon-number-operator eigenstates," Phys. Rev. A **36**, 1955 (1987);

[285] L.M. Zhang, D. Uttamchandani, and B. Culshaw, "Transient excitation of silicon microresonator", Electr. Lett. **25**, 149 (1989);

[286] L.M. Zhang, D. Walsh, D. Uttamchandani, and B. Culshaw, "Effect of optical power on the resonance of optically powered silicon microresonators", Sensors and Actuators A **29**, 73 (1991);

[287] C. Zhu and C.M. Caves, "Photocount distributions for continuous-wave squeezed light," Phys. Rev. A **42**, 6794 (1990);

[288] J.D. Zook, D.W. Burns, and J.N. Schoess, "Optically resonant microbeams", Proc. SPIE **2383**, 6 (1995);

[289] X.T. Zou and L. Mandel "Photon-Antibunching and sub-Poissonian photon statistics", Phys. Rev. A **41**, 475 (1990);

[290] A. Zucchetti, W. Vogel, M. Tasche, and D.-G. Welsch, "Direct sampling of density matrices in field-strength bases", Phys. Rev. A **54**, 1 (1996);

[291] W.H. Zurek, "Decoherence and the transition from quantum to classical," Phys. Today **44** (10), 36 (1991);

Acknowledgements

The work presented in this thesis has not been done by one person alone.
I am deeply thankful to

Prof. Mlynek, for patiently leaving an ecological niche on P8 in which research endeavors could grow, stimulated by international guest researchers and monetary fertilizer,
Stephan Schiller, for more than 4 years of creative disputes, ardous lessons in English style, and last not least the inauguration of the challenging SQL project,
Thomas Müller, for his brave work as my so-called first diploma student, the squeezing detectors, the first time-resolved measurement of the squeezed vacuum state and the micro-oscillator project are due to him (among many other things),
Thomas Kalkbrenner, for working his way with me through the first SQL-limits, bequeathing a highly usable diploma thesis,
Illka Tittonen, for many SQL calculations and "it would be nice, if we had ..." suggestions, not to mention the Lapponia Liqueur,
Ulf Leonhardt, for continuous input and many comments during his visits, making theory partially understandable for an experimentalist
Andrew G. White, for lively discussions when the first Wigner functions dropped out of the PC and for assistance in surviving formal conference dinners
Raffael Storz, Stefan Seel, Dr. Raphael Leonhardt, Hartmut Görig, and Ralph Sieber, for help in keeping cool
Jean-Philipe Poizat, for a three months crash course in basics of experimental optics,
Timo Felbinger, Hauke Hansen, and Christian Hettich for starting together with me the big step from $\chi^{(2)}$ to $\chi^{(3)}$,
Rüdiger Paschotta, for his help at the beginning of the squeezing experiment, especially for the design and ordering of the monolithic OPA, crystal # 25,
Robert Bruckmeier, for many discussions, especially the ones concerning frequency dependence of noise,
Tomas Opatrnỳ and Mohammed Dakna, for the joint work about phase reconstruction and discussions about two-mode fields,
Sze M. Tan, for the joint work about quantum state estimation and a gentle introduction to MATLAB,
Prof. Schleich and Fam LeKien, for the joint work about phase space interference,
Prof. Raymer and A. Faridani, for providing us with the original source code for the inverse Radon transform,
Ulf Janicke, for improvements regarding the numerical inversion,
Sigmund Kohler, for giving the SQL experiment a start,
Raid Al-Tahtamouni, for introducing some Arabian culture (and dishes) to our group,
Fabrizio Illuminati, for elucidating the time dependence of squeezed vacuum states,
Peter Münstermann, for high finesse help,
Markus Spiegel, for help in clean-etching some overcoated oscillators,
Christian Kurtsiefer, for ... I'm sure for something,
Prof. Robert O. Pohl, for his hospitality at Cornell,
Stefan Hahn, for much (non-quantum) mechanical help,

Stefan Eggert, for as same as much electronical help,
our secretaries Waltraud Heinzen, Ute Hentzen, and Renate Beck,
the superusers Mike Hartl, Björn Brezger, UJ, HH, RS for keeping the NeXT-cluster running, without which no pretty 3D-plots would exist,
Peter Bauer, on behalf of the university orchestra and Felix Köhler and Tessa Theodorakopoulos of the university theatre, for many glamorous performances,
Hauke Hansen, Heinz Meschede, Stephan Schiller, and Thomas Kalkbrenner for proof reading, and all our other group members Alex Beirer, Kamel Bencheikh, Tobis Boley, Claus Braxmeier, Anne-Catherine Etilé, Klaus Jäck, Patrick Kramper, Michael Lang, S.F. Pereira, Oliver Pradl, Jürgen Schoser, Uli Strössner, Dennis Weise, for the enjoyable atmosphere, not to mention all the other important people that I did not mention here.

...But release me from my bands
With the help of your good hands:
Gentle breath of yours my sails
Must fill, or else my project fails...

W. Shakespeare, The Tempest